

Quantum confinement in Si and Ge nanostructures: Theory and experiment

Eric G. Barbagiovanni,^{1,a)} David J. Lockwood,² Peter J. Simpson,³
and Lyudmila V. Goncharova³

¹Laboratory for Simulation of Physical Systems, Beijing Computational Science Research Centre,
Beijing 100084, People's Republic of China

²National Research Council, Ottawa, Ontario K1A 0R6, Canada

³Department of Physics and Astronomy, University of Western Ontario, London, Ontario N6A 3K7, Canada

(Received 7 July 2013; accepted 27 September 2013; published online 6 January 2014)

The role of quantum confinement (QC) in Si and Ge nanostructures (NSs) including quantum dots, quantum wires, and quantum wells is assessed under a wide variety of fabrication methods in terms of both their structural and optical properties. Structural properties include interface states, defect states in a matrix material, and stress, all of which alter the electronic states and hence the measured optical properties. We demonstrate how variations in the fabrication method lead to differences in the NS properties, where the most relevant parameters for each type of fabrication method are highlighted. Si embedded in, or layered between, SiO_2 , and the role of the sub-oxide interface states embodies much of the discussion. Other matrix materials include Si_3N_4 and Al_2O_3 . Si NSs exhibit a complicated optical spectrum, because the coupling between the interface states and the confined carriers manifests with varying magnitude depending on the dimension of confinement. Ge NSs do not produce well-defined luminescence due to confined carriers, because of the strong influence from oxygen vacancy defect states. Variations in Si and Ge NS properties are considered in terms of different theoretical models of QC (effective mass approximation, tight binding method, and pseudopotential method). For each theoretical model, we discuss the treatment of the relevant experimental parameters. © 2014 AIP Publishing LLC.

[<http://dx.doi.org/10.1063/1.4835095>]

TABLE OF CONTENTS

I. INTRODUCTION	2
A. Overview of nanostructure properties	2
1. Band gap engineering	3
2. Oscillator strength	5
3. Exciton/bi-exciton	6
4. Fine structure	8
5. Spin	9
6. Carrier tunnelling hopping	10
B. Applications of nanostructures	10
C. Comparison with compound materials.....	10
II. EXPERIMENTAL METHODS FOR THE PRODUCTION OF Si AND Ge NANOSTRUCTURES.....	10
A. Quantum dots.....	10
1. Co-sputtering.....	11
2. Plasma enhanced chemical vapour deposition (PECVD)	13
3. Molecular beam epitaxy	15
4. Ion implantation	17
5. Porous silicon (por-Si)	20

^{a)}Present address: Departamento de Física, Centro de Física das Interacções Fundamentais, Lisboa 1049-001, Portugal. Electronic mail:
santino.gasparo@gmail.com

B. Q-Wires.....	21
1. VLS technique	22
2. Oxide assisted growth	23
3. por-Si	24
C. Quantum wells.....	25
1. Magnetron sputtering.....	25
2. Plasma enhanced chemical vapour deposition	26
3. MBE.....	28
4. Thermal/chemical processing (SOI)	29
III. NANOSTRUCTURE PARAMETERS.....	30
A. QD parameters	31
1. Co-sputtering.....	31
2. PECVD.....	31
3. MBE	31
4. Ion implantation	32
5. Por-Si	32
B. Q-Wire parameters.....	32
1. VLS.....	32
2. OAG	32
3. Por-Si	33
C. QW parameters.....	33
1. Magnetron sputtering	33
2. PECVD.....	33
3. MBE	33
4. SOI	33

IV. THEORETICAL MODELLING.....	33
A. Overview of theoretical methods	34
B. Effective mass approximation, $\mathbf{k} \cdot \mathbf{p}$ method.....	35
1. $\mathbf{k} \cdot \mathbf{p}$ method applied for bulk phase	35
2. $\mathbf{k} \cdot \mathbf{p}$ theory for nanostructures	36
C. ETB method	37
1. General features of the ETB method for bulk phase	37
2. ETB theory for nanostructures	37
D. Empirical pseudopotential method	39
1. Bulk theory	39
2. EPM for nanostructures.....	39
E. Comparison of theories	40
V. CONCLUSIONS.....	42

I. INTRODUCTION

Nanotechnology has a long and fascinating history (see Chap. 1 of Ref. 1 for a historical overview dating back to 1884). The field gained considerable momentum following Feynman's famous lecture in 1959 on "There is plenty of room at the bottom."²

Nano-scaled materials allow one to exploit the fundamental "strangeness" of quantum mechanics, and this drives their interest for technology. Nanostructures (NSs) have found a home in all disciplines of science and engineering. From a fundamental perspective, NSs have opened the door to new physics; for instance, precisely engineered NSs allow for new schemes to be developed to measure Majorana fermions.^{3,4}

The field of NSs has seen an extraordinary boom in research, particularly due to their many applications (See references in Sec. IB). This boom has arisen in part because the properties of NSs can be influenced by a staggeringly large variation of structural and compositional parameters. These parameters can be adjusted intrinsically by varying the growth duration, changing the growth method, varying the matrix material, and doping the material (see Sec. II). Furthermore, temperature, the excitation conditions, and the spatial distribution of NSs will extrinsically change their properties. Therefore, researchers have found a wide variation in the behaviour of NSs leading to many diverse applications.

At the same time, this situation makes it difficult for the available theoretical tools to handle the diverse range of structural parameters (including interface and defect states) resulting from various experimental approaches. It is essential to understand how different parameters affect the observed properties of NSs to be able to accurately model these systems. Currently, theoretical work has progressed in this area through fitting with bulk material parameters and still using the physical approximations of the bulk, e.g., periodic boundary conditions. Therefore, experiment has pushed the boundary of applicability for current theoretical models in describing the required atomistic symmetries of a NS. For example, the effective mass approximation (EMA) is valid

when the diameter of the confinement axis is approximately at least twice the lattice constant. This situation is easy to maintain in III-V materials where the typical quantum dot (QD) size is on the order of 10–100 nm, but group IV QDs are much smaller, typically 1.5 → 5 nm for Si, which is in the breakdown regime of the EMA, although there are other ways to justify this approximation (see Sec. IV).

The general trend in the literature is to assume that NSs of the same material prepared by different means will have the same properties.⁵ The purpose of this review article is to classify the known experimental parameters according to preparation method and to make a detailed comparison with the most widely used theories. This field is far too vast for us to cover everything without writing a book on the subject. We will concentrate on the most widely used preparation methods for Si and Ge NSs, while compound materials will be discussed in Sec. IC.

In the remainder of this section, we provide an overview of relevant NS properties and interactions. In Sec. II, we discuss the most widely used preparation techniques and highlight the known structural, electronic, and optical properties relevant to the preparation method. In Sec. III, we review the important physical parameters for Si/Ge NSs. Finally, we deal with the current theoretical models and how each is able to describe the experimental parameters in Sec. IV.

A. Overview of nanostructure properties

The main interest in NSs is that one can exploit and control quantum mechanical properties not observed in an analogue bulk system. The effect of a few of these properties is discussed in this section.

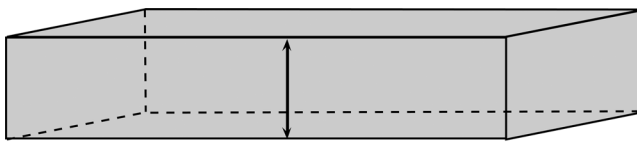
An important feature of NSs is that as the system dimension is changed, parameters affecting the electronic states/energies (e.g., defect states, stress, Coulombic interactions) do not change linearly with respect to each other (see below). Therefore, one must note the energy regime to understand the relevant parameters. In this article, we discuss which approximations are valid and which interactions contribute to the observed optical properties. Parameters as a function of system dimensions are highlighted, but it is important to note that external fields are also a critical factor. For instance, see Ref. 6 for a discussion of the effects of magnetic fields on NSs and excitons.

The information provided here gives a general overview. More details can be found in many good books and review articles. A few books pertinent to the subject of this review are Ref. 7 for a theoretical overview; Ref. 8 for great mathematical rigour; and Ref. 9 contains a nice blend of theory and experiment. Some review articles are: Refs. 10 and 11, concerning Si nanowires; Ref. 12 gives a general overview of low dimensional systems; Ref. 13 reviews group IV NSs with a focus on biological applications; Ref. 14 reviews Si NSs with a focus on theoretical aspects for stimulated emission; Ref. 15 focuses on exciton dynamics; Ref. 16 focuses on preparation of Si; Ref. 17 concerns light emission in NSs; Ref. 18 discusses experimental and theoretical results for light emission in Si with a focus on recently developed

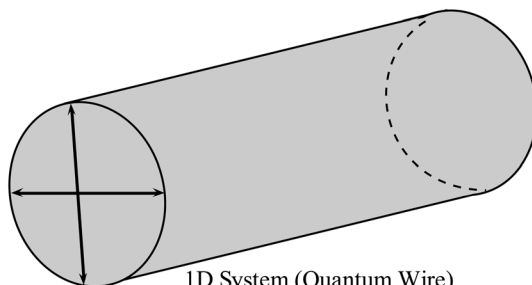
phenomenological theories; and Ref. 19 focuses on synthesis and applications.

1. Band gap engineering

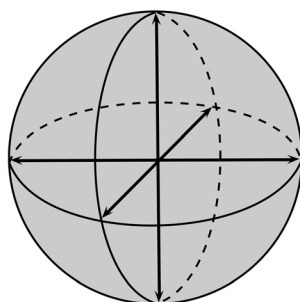
A NS is simply any material with one or more spatial dimensions reduced to the nanometre scale. The Bohr radius of charge carriers in a semiconductor is on the order of a few to tens of nanometres (≈ 4.5 nm in Si and 24 nm in Ge²⁰).²⁰ When one or more dimensions of a system are on par with this length scale, the carriers are said to be confined. A QD is defined as a system confined in three dimensions. Therefore, a QD has zero degrees of freedom, i.e., a QD is an OD system. Similarly, a quantum wire (Q-wire) is confined in two dimensions (1D system), and a quantum well (QW) is confined in one dimension (2D system). Schematically, these definitions are illustrated in Fig. 1. *Quantum confinement (QC) is defined as: a reduction in the degrees of freedom of the carrier particles, implying a reduction in the allowed phase space.* This effect happens through the use of a confining potential due to band gap differences with a surrounding matrix material or with electric field gradients. The alignment of the valence band (VB) and conduction band (CB) at the interface defines the strength of confinement and is important for carrier dynamics in the case of tunnelling phenomena. There are, in general, four types of band alignments: type-I (common to the materials described here), type-II staggered, type-II misaligned, and type-III.²¹ The



2D System (Quantum Well)



1D System (Quantum Wire)



0D System (Quantum Dot)

FIG. 1. Schematic representation of quantum wells, wires, and dots. The arrows indicate the confinement axis.

confinement potential is typically modelled as either Gaussian, or Pöschl-Teller, or in the simplest case a parabolic well.⁶

The interest in quantum confined structures is best summarized in the expressions for the density of states (DOS), $\rho(E)$ (number of states per unit volume per unit energy), defined as

$$\rho(E) = \frac{\partial N}{\partial E}, \quad (1)$$

where N is the total number of states per unit volume. For the bulk system (3D system), with momentum wave-vector \mathbf{k} : $N = \frac{k^3}{3\pi^2}$. For a 2D system (i.e., two degrees of freedom): $N = \frac{k^2}{2\pi}$. For a 1D system: $N = \frac{2k}{\pi}$. For a 0D system, there is no \mathbf{k} -space to be filled and the number density is discrete. These definitions lead to the following expressions for the DOS:

$$\begin{aligned} \rho_{3D}(E) &= \frac{1}{\pi^2} \left(\frac{m^*}{\hbar^2} \right)^{3/2} \sqrt{2E}, \\ \rho_{2D}(E) &= \frac{m^*}{\pi\hbar^2} \sum_{n_x} \Theta(E - E_{n_x}), \\ \rho_{1D}(E) &= \frac{1}{\pi\hbar} \sqrt{2m^*} \sum_{n_x, n_y} (E - E_{n_x, n_y})^{-1/2}, \\ \rho_{0D}(E) &= 2 \sum_{n_x, n_y, n_z} \delta(E - E_{n_x, n_y, n_z}), \end{aligned} \quad (2)$$

where m^* is the effective mass, $\Theta(E)$ is the step function, E is the energy of the particular state, E_{n_i} with $i = x, y, z$ is the quantized energy of the particular confinement direction, and $E_{n_x, n_y} = E_{n_x} + E_{n_y}$, etc. To first order, in the infinite cubic potential configuration,

$$E_{n_i} = \frac{\hbar^2 \pi^2 n_i^2}{2m^* D_i^2}, \quad (3)$$

where n_i is the principal quantum number and D_i is the confinement diameter. Note that the energy in Eq. (3) is offset by the band gap energy, E_G , in a semiconductor. A plot of the DOS for systems of different dimensionality is given in Fig. 2. The DOS is plotted considering a confinement diameter of 2 nm and using the Si effective mass of $m^* = 1.08m_o$, where m_o = electron mass. Each level is plotted for only higher quantum numbers $n_x = 1, 2, 3$, for simplicity.

The DOS illustrates that a change in the confinement dimension directly changes the energy occupation level. Thus, a modification in the DOS with respect to the dimension of the system is referred to as band gap engineering; a device can be engineered to absorb/emit light at a tunable wavelength. For example, Si can be tuned by proton implantation to operate as an optical detector at the telecommunications wavelength of 1550 nm, whereas the bulk band gap corresponds to 1100 nm.²²

Besides modifying the DOS, band gap engineering can occur in another fundamental way. Silicon and germanium are indirect gap materials in their bulk state. Such indirect-gap electronic structures in pure form require phonon

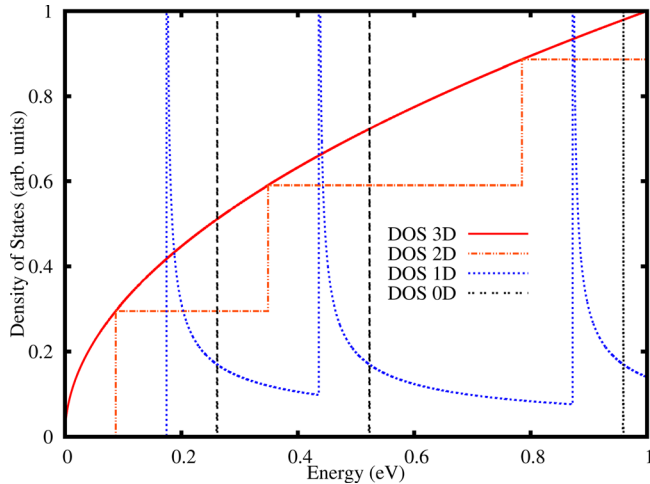


FIG. 2. Plot of the DOS for a bulk (3D), Q-wire (2D), QW (1D), and a QD (0D) system. The figure is not drawn to scale. The DOS is plotted considering a confinement diameter of 2 nm and using the Si effective mass of $m^* = 1.08 m_e$, where m_e = electron mass. Each level is plotted for only higher quantum numbers n_s , for simplicity. Note that in a semiconductor system the DOS is offset from the Fermi level by either the CB or VB energy, which is set to 0 in the figure.

scattering for optical absorption/emission, in order to maintain momentum conservation. However, in the NS, optical transitions can happen without the aid of a phonon event by breaking the momentum conservation rules and/or by making the material quasi-direct through the process of Brillouin zone-folding.²³ The origins of these two processes are physically different, but they produce nearly identical effects.

Breaking of the momentum conservation rules (\mathbf{k} -conservation) is a direct prediction from the Heisenberg uncertainty relation. A reduction of the system dimension implies an increase in the spread of the electron/hole wavefunction in momentum space. Fig. 3 shows confinement in the x -direction in \mathbf{k} -space for the electron and hole wave-functions in the Gaussian confinement approximation, given by

$$\Psi_{\mathbf{k}} = \frac{(2\pi)^{3/2}}{V} \prod_{i=x,y,z} \left(\frac{\sigma_i}{\pi^3} \right)^{1/4} e^{-\frac{k_i^2 \sigma_i^2}{2}}, \quad (4)$$

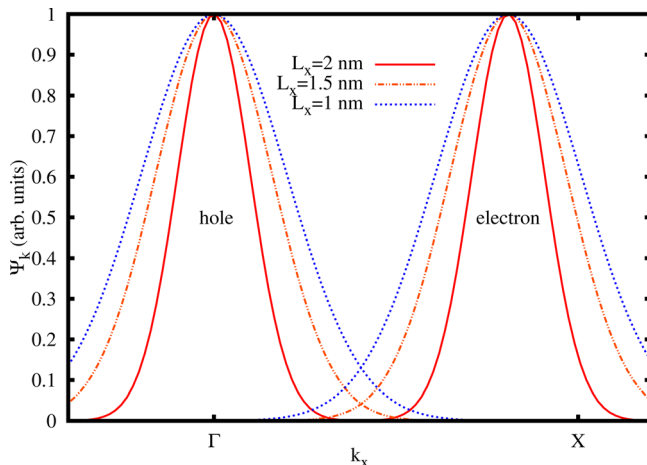


FIG. 3. Plot of a Gaussian envelope function for a single confinement direction in \mathbf{k} -space with an electron centred at $0.8 \times \text{X}$ -point and a hole at the Γ -point in the Brillouin zone, as appropriate for Si. The plot is not normalized and is shown for three different values of confinement dimension, L_x .

where V is the volume of the crystal and σ_i is the Gaussian width parameter. It is clear in Fig. 3 that as the confinement dimension L_x is reduced, the width in momentum space is increased. For Si with the hole located at the Γ -point ($\mathbf{k} = 0$) in the VB (the same applies in Ge) and the electron at $0.8 \times \text{X}$ -point ($\mathbf{k} = \frac{2\pi}{a_c}$, where a_c is the lattice spacing) in the CB (the CB minimum is at the L-point in Ge), lowered dimension implies increased coupling in the transition matrix elements between the electron and hole states (see Sec. IA2) and hence an increased transition probability. Therefore, Fig. 3 is a demonstration of a breaking in the \mathbf{k} -selection rules. In other words, transitions across the band gap between different locations in the Brillouin zone can occur without the aid of phonons. Moreover, disorder can cause breaking of \mathbf{k} -conservation rules, as in the case of $\text{Si}_{1-x}\text{Ge}_x$ or $\text{Si}_{1-x}\text{C}_x$.²⁴

In the work of Ref. 25, it was shown that the breaking of \mathbf{k} -conservation rules is strongly NS size and shape dependent. In Si NSs, \mathbf{k} -conservation is strongly broken below a size of ≈ 2.5 nm, implying that phonon-free transitions dominate.²⁵ (Breaking of the \mathbf{k} -selection rules can occur in larger Ge NSs compared to Si, because of the larger Bohr radius in Ge.) Furthermore, resonant photoluminescence (PL) measurements²⁶ have shown that for higher confinement energies, 0.65 to 0.7 eV, the no-phonon process dominates, which is in agreement with Ref. 25. These observations are equivalent to the existence of a sizeable Fourier component in the envelope function, Eq. (4), corresponding to the magnitude of the indirect gap, which plays the role of the phonon.^{27,28} This type of transition is called *pseudo-direct*. Theoretically, one can calculate the band gap energy for indirect transitions without considering the phonon momentum.²⁹

While the \mathbf{k} -conservation rules are sufficiently broken to allow for indirect transitions, it is clear that this type of transition has a significantly lower coupling strength than the direct gap transition. The lifetime in Si NSs is on the order of microseconds, which is typical for the indirect gap.³⁰ There is a direct gap in Si and transitions at the Γ -point do occur with a lifetime on the order of picoseconds.³¹ This observation is a consequence of the fact that while the band structure retains its indirect character, direct transitions occur with high coupling strength and fast recombination times, in addition to indirect transitions with a lower coupling strength and longer recombination time (see Sec. IA2). Typically, these direct transitions are due to “hot” carriers.³¹

Zone-folding is the other mechanism by which zero phonon transitions can be observed. Zone-folding, in principle, is very difficult to achieve as it requires many factors to work together rather nicely. The conduction band minimum in Si lies at $0.8 \times \text{X}$ -point. If the dimension of the system is reduced in such a manner that the remaining empty \mathbf{k} -space corresponds exactly to a reduced-zone scheme with the $0.8 \times \text{X}$ -point corresponding with the Γ -point at $\mathbf{k} = 0$, then one has created a direct gap NS. In Si, this situation happens in heterostructures when there is a decrease in the periodicity by a factor of five, resulting in the Brillouin zone being divided into fifths, with the proviso that no other modifications happen to the band structure.²³ Brillouin zone-folding mixes \mathbf{k} -space due to the fact that a large fraction of the \mathbf{k} -space is

now empty, which implies large perturbations in the system. In the dilute limit, the folded zone shrinks to zero and only direct transitions remain, if they are permitted by symmetry.³²

Zone-folding is best observed in structures where the band gap offset is minimized at the interface; otherwise, there will be significant band bending. SiGe/Si superlattices are typical candidates for zone-folding,²³ whereas isolated QDs are not ideal candidates for zone-folding²⁷ because of the significant band offset. Calculations have predicted a direct gap behaviour in SiC nanowires.³³ Direct evidence of zone-folding has been observed experimentally³⁴ by reconstructing the Brillouin zone via Raman scattering measurements. Moreover, as in the case above, when a direct transition occurs, one expects short radiative times. Indeed, Si-Ge Q-wells show a lifetime of the order of picoseconds.³⁵

2. Oscillator strength

The most commonly cited issue regarding the optical properties of Si or Ge is the low oscillator strength, which yields a low absorption efficiency. It is also well known that QC acts to increase the oscillator strength. The concept of the oscillator strength is understood by studying the dipole matrix elements, which also provides insight into electronic transition selection rules. The selection rules as determined by the oscillator strength can be complicated by band degeneracy and by the fine structure, discussed further here and Sec. IA 4. First, a review of some of the basic properties of light-matter interactions in NSs is presented (some references are given in Sec. IA and in Refs. 36 and 37.)

The formalism for optical absorption in NSs is centred around the validity of the dipole approximation. This approximation is based on the fact that the wavelength of the excitation light, typically in the visible range, is much larger than the typical size of a NS. The confinement axis of a NS is typically a few to a hundred nanometres, making it is easy to justify the dipole approximation. The Hamiltonian for light interaction with a NS is

$$\left[\frac{(\mathbf{p} + e\mathbf{A})^2}{2m_o} + V_c(\mathbf{r}) \right] \Psi(\mathbf{r}) = i\hbar \frac{\partial \Psi(\mathbf{r})}{\partial t}, \quad (5)$$

where e is the electric charge, m_o is the free electron mass, \mathbf{p} is the momentum operator, \mathbf{A} is the vector potential defined in the Coulomb gauge with the electric field given by $\mathbf{E} = -\frac{\partial \mathbf{A}}{\partial t}$, $V_c(\mathbf{r})$ is the crystal potential, and $\Psi(\mathbf{r})$ is the total wavefunction for the Bloch electrons. The vector potential is used to ensure transverse optical effects with a constant dipole, while a scalar potential yields longitudinal effects that generally have zero transition probability.

The perturbing potential is extracted from Eq. (5)

$$V = \frac{e}{m_o} \mathbf{A} \cdot \mathbf{p}. \quad (6)$$

From Eq. (6), one can apply Fermi's golden rule under the assumption that \mathbf{A} is slowly varying with time, which is justified again by the dipole approximation. Ignoring the photon

momentum ($\therefore \mathbf{k}_{\text{photon}} \approx 0$), the transition probability from an initial state, i , to a final state, f , is given by

$$w_{fi} = \frac{2\pi}{\hbar} \left(\frac{eE_o}{m_o\omega} \right)^2 |\langle f | \epsilon \cdot \mathbf{p} | i \rangle|^2 \times \delta(E_f - E_i - \hbar\omega), \quad (7)$$

where E_o is the magnitude of the electric field, ω is the angular frequency of the light field, and ϵ is the polarization of the light field. E_f and E_i are the final and initial state energies, which in the case of semiconductor transitions across the gap means that the delta function in Eq. (7) relates to energy conservation. In principle, the energy of the initial and final states depends on the wave-vector, \mathbf{k} . Assuming that the effective mass is the same in each of the sub-bands, then for a particular \mathbf{k} , the transition energy is written as $E_f - E_i = \hbar\omega_{fi}$, and thus from Eq. (7), the following expression is extracted:

$$f_{fi} = \frac{2}{m_o\hbar\omega_{fi}} |\langle f | \epsilon \cdot \mathbf{p} | i \rangle|^2 = \frac{2m_o\omega_{fi}}{\hbar} |\langle f | \epsilon \cdot \mathbf{r} | i \rangle|^2, \quad (8)$$

where \mathbf{r} is the position vector. The second expression follows from the commutation rules between the Hamiltonian and \mathbf{p} . f_{fi} is what is typically quoted as the oscillator strength, and $|\langle f | \epsilon \cdot \mathbf{r} | i \rangle|$ is the dipole matrix element.

From the definition of the transition probability, Eq. (7), it is a simple matter to define the optical absorption of a material

$$\alpha_{fi} = \frac{w_{fi}\hbar\omega}{t\mathbf{S}}, \quad (9)$$

where the time dependence, t , comes from \mathbf{A} , and \mathbf{S} is the Poynting vector. The absorption edge is shifted to a higher energy due to QC, and being proportional to the DOS we should expect to see discrete transitions in the absorption spectrum.³⁸ Therefore, to understand the absorption in a NS, one needs to understand the DOS (Eq. (2)), the gap energy, and the initial/final states. How these factors are determined is strongly dependent on the theory used. This point will be discussed further in Sec. IV. The importance of Eq. (7) or (8) is that it is related to the optical functions: dielectric function, index of refraction, conductivity, and susceptibility.³⁶ Note that a more sophisticated derivation for the absorption is given through the Elliot formula using the semiconductor Bloch equations, which considers the details of the band structure.³⁹ In addition, it is important to note that this formalism is not valid in the case of an optical cavity where the light field will become quantized, which is an important situation for opto-electronic applications.

To understand the meaning of the oscillator strength in a NS, recall Sec. IA 1 and Fig. 3. From Eq. (8), the oscillator strength is a function of the momentum transfer matrix between the initial and final states, which increases as the dimension of the system decreases. The reason for the increase in oscillator strength is because of the increase in

wavefunction overlap, depicted in Fig. 3. This observation directly states that an increase in the oscillator strength results in an increase in the coupling efficiency from the ground state to the excited state. For the indirect gap material, one must still consider whether this increase is considerable enough to allow transitions at different points in the Brillouin zone without the aid of a phonon.⁷ Furthermore, an increase in the oscillator strength means a decrease in the lifetime of a sample, which is observed in experiment.³⁰

The oscillator strength contains detailed information concerning the allowed transitions. The symmetry of the wavefunctions determines whether the transition is allowed, while fine structure details will mix states making otherwise forbidden transitions weakly permissible. Filling of the subbands determines whether carriers are present for optical transitions, which can be modified by doping, pumping, or changing the temperature. In an anisotropic NS, the degeneracy of states can be removed and forbidden transitions become allowed (see Ref. 9 for a more detailed discussion of these points).

Formally, the oscillator strength partly determines the selection rules.⁷ Consider the matrix element $\langle f | \epsilon \cdot \mathbf{p} | i \rangle$. In the effective mass representation for the QC system, the initial and final states of a semiconductor material are a product of the Bloch function and an envelope function. The envelope function will be represented by the wavefunction along the confinement axis. Therefore, for interband transitions, the matrix element breaks into a product

$$\epsilon \cdot \langle u_{V\mathbf{k}}(\mathbf{r}) | \mathbf{p} | u_{C\mathbf{k}}(\mathbf{r}) \rangle \langle F_{n\mathbf{k}}^h(\mathbf{r}) | F_{m\mathbf{k}}^e(\mathbf{r}) \rangle, \quad (10)$$

where $u_{C(V)\mathbf{k}}(\mathbf{r})$ are the Bloch functions for either the conduction, C, or valence, V, states, and $F_{n\mathbf{k}}^{h(e)}(\mathbf{r})$ are the envelope functions of the n th band for either the electron, e, or the hole, h. In a symmetric well, the transition across the gap implies that $n = m$ for even parity in the ideal case. The conduction and valence Bloch functions are first subject to the polarization selection rule. Evaluating $\langle u_{V\mathbf{k}}(\mathbf{r}) | \mathbf{p} | u_{C\mathbf{k}}(\mathbf{r}) \rangle$ within the $\mathbf{k} \cdot \mathbf{p}$ formalism, symmetry-allowed transitions become clear. The momentum operator has Γ_4 symmetry in zinc-blend and diamond structures.⁴⁰ In general, a p-like hole with Γ_{8V} symmetry can couple with an s-like electron with Γ_{6C} symmetry via circularly polarized light. Intraband transitions happen between n and m odd states.⁷ Selection rules for QDs are generally not as strict in terms of polarization because the confinement is in all three directions; however, they become more relevant in Q-wires and QWs. In a QD, the main selection rules for intraband transitions are according to those given by spherical harmonics for the orbital angular momentum, l : $\Delta l = \pm 1$.

The considerations so far depend strongly on the assumption of non-degenerate parabolic bands. Under this assumption, absorption happens between δ -like energy states. Experimentally, one observes broadening in the absorption lines through the oscillator strength. The first source of broadening is in the differences of the effective masses between the conduction and the valence states. Further, a dispersion in NS sizes causes inhomogeneous broadening, yielding Gaussian-like absorption peaks. Homogeneous broadening comes from

random interactions described by the decoherence time. The decoherence time is finite, and thus, the optical DOS is replaced by a Lorentzian. Complications arise due to the multiple sources of scattering that exist in a NS.

As mentioned, the degeneracy of states is a critical factor. In the degenerate system, the valence band ground state is eight-fold degenerate. However, as the system dimension is reduced, the exchange interaction increases (see Sec. IA 4), thus removing the degeneracy and creating “bright” and “dark” exciton states. Due to symmetry, the “bright” state is at a higher energy than the “dark” state. Therefore, in a low temperature system, there exists a higher probability that the “dark” state is occupied. This situation has the effect of reducing the oscillator strength because the transitions are not dipole allowed.^{41,42}

For any semiconductor, an important consequence of an increased oscillator strength is the possibility of lasing.⁴³ Optical gain is a function of radiative versus non-radiative processes. Non-radiative processes are typically dominated by surface trapping and multi-particle Auger relaxations. Surface trapping states can be controlled by well passivated NSs; therefore, typical limitations come from Auger processes. Radiative processes have characteristic times on the order of microseconds while Auger process are on the order of nanoseconds; therefore, to achieve population inversion for optical gain, the pump time must be faster than the Auger time. Owing to the increase in optical absorption for the NS, this situation is achievable. For a review of optical gain in Si NSs, see Refs. 43 and 44. Following a theoretical prediction of a large optical gain in ultra thin silicon QWs,⁴⁵ Saito *et al.*⁴⁶ have recently observed optical gain and stimulated emission by current injection into an ultra thin QW of crystalline Si embedded in a resonant optical cavity. At present, lasing has only been observed in Ge for the case of strained⁴⁷ and doped⁴⁸ Ge layers.

3. Exciton/bi-exciton

Optical properties of semiconductors cannot be fully understood without discussing excitonic states. For a discussion of bulk excitons, see the classic work of Knox.⁴⁹ For nice reviews of the properties of excitons in NSs, see Refs. 39 and 50. Furthermore, solar cells (Sec. IB) require the production of multiple exciton pairs. This phenomenon was studied initially in the case of CdSe and PbSe NSs⁵¹ but has also been demonstrated in Si NSs.⁵² For a discussion of multiple exciton generation in photovoltaic applications, see Ref. 53.

Excitons are typically created in semiconductors through optical excitation of carriers, leading to a bound state of an electron and hole. They can also be formed by carrier injection. The exciton bound state is understood from the inclusion of the Coulomb interaction between the electron-hole pair. It is valid to treat excitons in a hydrogenic type model for the correlation energy and thus the binding energy of the exciton. The exciton is truly hydrogenic in the case that the hole mass is much larger than the electron mass, whereas when they are approximately the same, the exciton is more positronium like. In the case of organics, one

observes tightly bound excitons, or Frenkel excitons. In the case of semiconductors, one observes loosely bound excitons, or Wannier-Mott excitons, which have been shown to be hydrogen-like.⁵⁰ In this framework, the exciton energy, E_X , is written as

$$E_X(n, \mathbf{k}) = E_G - R'_y \frac{1}{n^2} + \frac{\hbar^2 \mathbf{k}^2}{2\mu},$$

$$R'_y = \frac{1}{\epsilon^2 m_o} 13.6 \text{ eV}, \quad (11)$$

where n is the principal quantum number, \mathbf{k} is the electron plus hole wavevector ($\mathbf{k} = \mathbf{k}_e + \mathbf{k}_h$), μ is the reduced mass in terms of the electron and hole effective mass ($\frac{1}{\mu} = \frac{1}{m_e^*} + \frac{1}{m_h^*}$), R'_y is the exciton Rydberg energy, E_G is the gap energy, and ϵ is the dielectric constant. The exciton Rydberg energy in Eq. (11) is simply corrected by the reduced mass of the exciton and the dielectric constant. The exciton Bohr radius is given by

$$a_B^X = a_B^H \epsilon \frac{m_o}{\mu}, \quad \text{for } n = 1, \quad (12)$$

where a_B^H is the Bohr radius in the hydrogen atom. The Coulomb energy of the exciton state lowers the energy of the exciton ground state with respect to the free electron-hole pair. Therefore, one can observe exciton absorption through the fact that the absorption will occur below the band gap edge. Fano resonances are also an important consideration for exciton absorption.³⁹ In addition, the Coulomb energy increases the probability of finding the electron and hole in the same place.⁵⁴

The magnitude of the Coulomb energy is typically on the order of $10 \rightarrow 40$ meV, which is much less than the gap energy.¹⁴ In the case of strong confinement, the confinement potential is much stronger than the Coulomb interaction. Therefore, one can treat the Coulomb energy as a perturbation.⁵⁴ Typically, excitons do not play a significant role in Si NSs because the excitation energy is much larger than the Coulomb energy for very small sizes of the NSs. Ge has a larger Bohr radius than Si, meaning that these structures encompass a larger regime of QC where the Coulomb effects can be more important. The thermal energy must also be considered when thinking of excitonic effects.⁵⁵ The Coulomb energy is significant at only around a few Kelvin, where exciton effects have been observed.^{56,57}

In the above discussion, the effect of system dimension is handled through the evaluation of the exciton energy as a function of size. The system dimension can have another important effect on the energy. In an infinitely thin QW (such as graphene), the principal quantum number becomes $n \rightarrow n - \frac{1}{2}$, and the general form of this expression is

$$n \rightarrow n + \frac{d_{eff} - 3}{2},$$

$$d_{eff} = 3 - \exp\left(\frac{-L}{2a_B^X}\right), \quad (13)$$

where d_{eff} is the effective dimension ranging between 3 and 2, and L is the QW thickness.⁵⁵ The Bohr radius is thus reduced by a half, the exciton energy increases by four, and the oscillator strength increases by a factor of eight for the infinitely thin well. The renormalization of the principal number is numerically treated in Ref. 8 (see Figs. 6.4 and 6.5). The effect is usually ignored because the system is not truly a 2D system.

Of the features discussed so far, by far the most important feature is the correct treatment of the dielectric constant. This point does not have a clear solution, and yet, it is critical in correctly determining the exchange interaction (Sec. IA 4). Typically, the Coulomb interaction is screened by the bulk dielectric constant. However, there is some disagreement over the correct value that should be used. In the work of Ref. 58, the Penn model was used to calculate the variation of the dielectric constant with dimension starting from several different values for the matrix dielectric constant, which all yielded essentially the same result. A comparison of the Penn model and a pseudopotential calculation yields very different results.⁵⁹ In the work of Ref. 60, the bulk dielectric constant was used. Dielectric constant corrections lead to corrections in the Sommerfeld factor, which lead to an increase in the absorption.⁹

Two limiting cases for the dielectric function can be easily understood. If the exciton binding energy is less than the optical phonon energy (i.e., the exciton Bohr radius is greater than the polaron radius), then the static dielectric constant can be used. In the case that the exciton energy is comparable with the optical phonon energy, then a dielectric constant between the bulk value (high frequency) and the static dielectric constant can be used.⁵⁵ In this second case, one can use the Haken potential.⁶¹ Neither of these cases can be rigorously justified.

A more accurate treatment of the screening of the electron-hole interaction should contain a contribution from the induced surface polarization charge. To this end, the nature of the interface plays a large role in the details of the dielectric function, whereby an inner dielectric function can be defined by separating the surface contribution. Defining an image charge in this way allows one to consider surface self-energy corrections based on the difference between the inner and outer dielectric functions.⁷ In the case where the inner and outer dielectric functions are of the same order, image charge corrections are not as significant. Generally, one finds that the dielectric function is replaced by the dielectric function in the Thomson-Fermi approximation, which ignores surface polarization effects. This approximation is valid for energies lower than the plasmon energy.

Finally, there are a few fine points to consider in the study of the exciton. Mass re-normalization will also affect the binding energy of an exciton. In a non-rigid lattice, polaron effects couple to the effective mass through Fröhlich couplings. The binding energy of the exciton partly renormalizes this effect. Generally, these couplings are not as important in the case of lower gap materials where they tend to lower the gap energy.^{55,62,63}

Biexciton complexes are also a fascinating subject in the study of NSs. A biexciton is simply the bound state between two excitons. This condition is usually observed in a highly excited NS system, i.e., where the exciton density is high enough that bound states can form (see Refs. 12 and 64 for a general discussion). Biexcitons create a situation of interesting decay dynamics due to the fact that they change the decay scheme to a biexciton decaying to an exciton and then to the ground state.⁶⁵ This situation creates an opportunity to observe exciton condensation experimentally.⁶⁶ As exciton observation is generally complicated in the case of Si and Ge structures, it is even more difficult to observe biexcitons, and very little research has been conducted in this area. The problem in Si and Ge is that biexciton lines can be very broad and hard to distinguish.⁶⁷

4. Fine structure

While the “fine structure” is governed by the exchange and spin-orbit (SO) interaction, it is also mediated by the Coulomb interaction and confinement potential, in principle. The magnitude of these interactions follows Hund’s principle.⁶⁸ For small NSs, this principle is very similar to the rules for an atom. Experimentally, one uses resonant PL and PL excitation (i.e., size selective spectroscopy)⁹ to measure the fine structure.

For some time, these interactions were not extensively studied in Si and Ge. The order of magnitude is small ($\mathcal{O}(10 \text{ meV})$), and inhomogeneous broadening can mask the fine structure in the absorption or emission spectrum. More recently, there is significant research on this topic, because it has been reported that Si may have ideal spin coupling properties for quantum computing.^{69–72}

The exchange interaction is understood in the Hartree-Fock approximation for semiconductors.⁷ In this approximation, the proper symmetry states of the many-electron problem are treated using a Slater determinant of atomic orbitals. Using a variational approach, one obtains single particle states, where the two particle interaction terms go like,

$$\frac{1}{2} \sum_{nm} (\langle nm|V|mn\rangle \pm \langle nm|V|nm\rangle), \quad (14)$$

where V is the Coulomb potential and $\{n\}$ is the set of one particle states, and $|mn\rangle^* = \langle nm|$. The first term in Eq. (14) is the direct Coulomb interaction, and the second term is the exchange interaction. The exchange interaction represents an intrasubband interaction between anti-parallel Pauli states. The spin representation is not made explicit in Eq. (14). This dependency comes from the fact that in a two particle system there are singlet (spin $S=0$) and triplet ($S=1$) spin states. The total wavefunction is the product of a spatial and a spin part. The triplet spin wavefunction is symmetric, and the singlet is antisymmetric. Therefore, in the case of fermions, the spatial part of the singlet wavefunction is symmetric and the spatial part of the triplet is antisymmetric. In Eq. (14), the “±” comes from the symmetry of the spatial part. The “+” sign is from the singlet and the “−” sign from the triplet wavefunction. This means that the triplet is at a

lower energy, which is the so-called “dark” exciton (see Sec. IA 2).

The SO interaction is a relativistic effect that has the form

$$\frac{\hbar}{4m_e^2c^2}(\nabla V_c(\mathbf{r}) \times \mathbf{p}) \cdot \boldsymbol{\sigma}, \quad (15)$$

where $\boldsymbol{\sigma}$ represents the Pauli matrices. In the $L \cdot S (= 1/2(J^2 - L^2 - S^2))$ coupling scheme, the four valence electrons exist in an sp^3 hybridized state. The total angular momentum is given by $J=L \pm S$. Thus, there are two states $J=3/2, 1/2$. The SO interaction, Δ_{SO} , splits these states into a 4-fold degenerate $J=3/2$ band and a $J=1/2$ split off band, depicted in Fig. 4. When there is no SO interaction, the degeneracy at the Brillouin zone centre remains. When the SO interaction is considered, the split off band ($J=1/2$) is shifted downwards, while the $J=3/2$ state is shifted up. The two bands are split by Δ_{SO} , which is on the order of 0.044 eV in Si and 0.3 eV in Ge.⁷³ Furthermore, the $J=3/2$ band becomes nondegenerate for increasing wave-vector as the band splits into two parts, the heavy hole (hh) and the light hole (lh). While Δ_{SO} is very small in Si and will not likely be detectable as a change in the confinement energy, it still has a very important effect through mixing the dark and bright exciton, mentioned in Sec. IA 2.

The energy levels of the exciton states are schematically depicted in Fig. 5. The exciton is comprised of the lh or the hh plus an electron, in either case. These states are represented to the left of Fig. 5. The $J=3/2$ hh combines with the $J=1/2$ electron to form an 8-fold degenerate state split into $J=2$ (5-fold) and $J=1$ (3-fold) states. The $J=1/2$ lh state combines with an electron to form a 4-fold state made up of $J=1$ (3-fold) and $J=0$ (non-degenerate). These states are split according to the total angular momentum states m_J . A description of these states can be found in many textbooks (see Ref. 74). In the exciton model, a two-body system, the two spin states formed by spin 1/2 particles are $S=0, 1$, shown in Fig. 5. The splitting between these two states, discussed above, occurs via the exchange interaction, Δ_{EX} . The $S=1$ state is made up of $J=2, 1, 0$, while the $S=0$ states contains $J=1$.

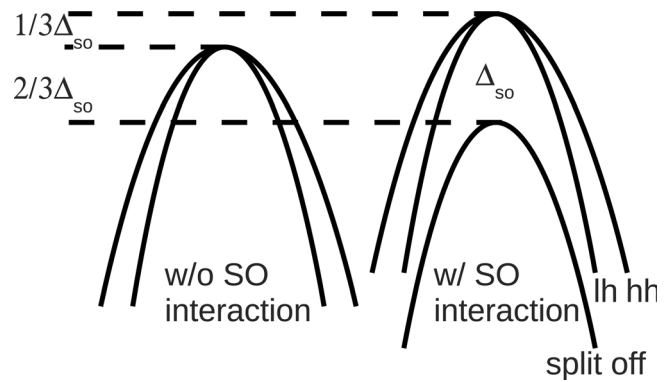
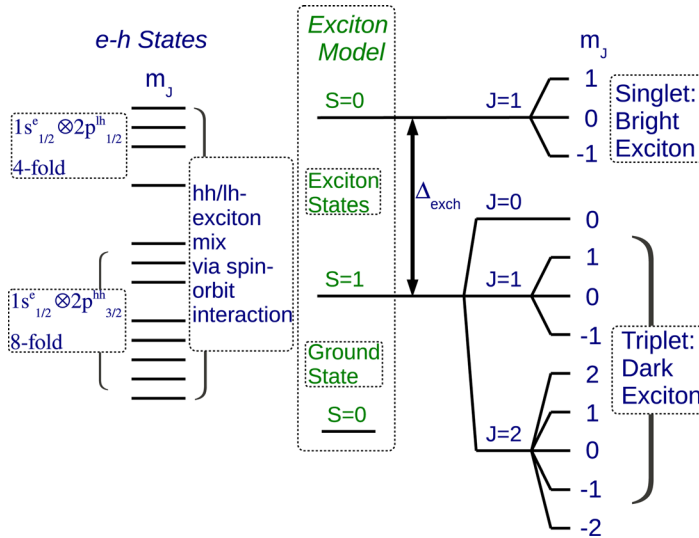


FIG. 4. Schematic representation of valence band states. When there is no SO-interaction (left) the degeneracy in the valence states remains. When the SO-interaction is considered, the split-off ($J=1/2$) band separates from the hh and lh states, by Δ_{SO} . Δ_{SO} shifts the $J=3/2$ state up and lowers the $J=1/2$ state.



When the exchange interaction is not too large, the degeneracy in m_J is not completely removed, and this allows for radiative transitions from the $S = 1$ state. At low temperature, only the $S = 1$ state is occupied. As shown in Fig. 5, the ground state in the exciton model is $S = 0$. Therefore, transitions to the ground state are strictly not allowed from the $S = 1$ state. However, the SO interaction splits the J states and if the exchange is not too large the $S = 0$ and $S = 1$ state will overlap. Therefore, there exists a finite probability that even at low temperature the $S = 0$ state is occupied and transitions will be allowed. These transitions can also become allowed through anisotropy by breaking the selection rules.^{41,42,75} In general, it is the anisotropic nature of a NS that removes the degeneracy between the J states and allows for the simple two level exciton model. In the case of small dots, the selection rules must be broken because the exchange interaction goes with the inverse of the QD size, whereas the SO interaction is constant with size. Therefore, there would be no overlap and transitions could not occur. However, radiative transitions are observed.^{41,42}

By studying the radiative rate of the singlet and triplet states, the role of the exchange and SO interaction is determined. Experimentally, at a few Kelvin, there is a discrepancy between absorption and emission energies of a few meV.⁷ This is explained by the observation that absorption happens in the $S = 0$ state and emission from the $S = 1$ state. In addition, in Si QDs, it has been observed that the decay time of the PL decreases as the temperature increases and the PL intensity increases.⁴¹ With increasing temperature, the $S = 0$ state becomes populated, and therefore, the oscillator strength increases. Around $T = 100$ K, the singlet state becomes fully populated and the PL intensity decreases above this temperature, because non-radiative channels become populated.^{41,42,75}

Critically, the magnitude of the exchange and SO interaction is not significant compared to the confinement energy. Thus, it is justified to not include these interactions in a calculation of the variation in the gap energy. However, their existence in a NS is significant, because they determine the radiative states and hence the oscillator strength. In the literature, there is a large variation in the values reported

FIG. 5. Schematic representation of exciton states, not drawn to scale. From the left, the e-h states schematic represents the combination of the hh-exciton (8-fold degenerate) and the lh-exciton (4-fold degenerate). The m_J , total momentum magnetic number, states are depicted. The states are mixed through the SO interaction. In the exciton model, the s-like 1/2-spin electron combines with the p-like 1/2-spin hole, forming spin $S = 0$ and $S = 1$ states. Ground state $S = 0$ is shown. $S = 0, 1$ states are split by the exchange interaction, Δ_{EX} . The $S = 1$ spin state forms $J = 2, 1, 0$ (triplet dark exciton), and $S = 0$ yields $J = 1$ (singlet bright exciton).

experimentally and theoretically, particularly for the SO interaction, because of the difficulty in directly measuring these quantities.

In Secs. IA 1–IA 4, factors that contribute to QC in NSs were discussed, resulting in a modification of the gap energy and the selection rules. For the remainder of Sec. IA, two features that are general consequences of QC are discussed. Spin states (Sec. IA 5) and tunnelling (Sec. IA 6) are important phenomena to study for quantum mechanical structures. We discuss these two features briefly.

5. Spin

Traditionally, spin states were only of interest in magnetic materials, because in the bulk state only these materials will have a net spin state. In various magnetic devices, research interest is concerned with the study of spin state diffusion at an interface. In addition, scattering with the interface can lead to spin flip. In the context of QWs, one could then study spin tunnelling phenomena when the width of the well is made comparable to the spin diffusion length.⁷⁶ In the NS, one has atomic-like energy levels to consider. This means that energy level filling will happen according to the Pauli principle. Therefore, precise spin-filling is possible.⁷⁷ The number of spin-states can be controlled with an electric field.

Most research concerning spin studies for spin-based devices is on III–V materials. Recently, it has been realized that group IV materials are also a good candidate, because of their weak SO interaction, implying long spin lifetimes.⁷⁸ Ge has a stronger SO interaction than Si, which might make it easier to control the spin state due to stronger coupling. However, this reduces the coherence time.⁷⁹

The most promising candidate for studying spin states is ²⁸Si, which has no net nuclear spin. This means that decoherence is not a problem.⁷⁰ There is a great deal of research now into the use of spin states in Si for various applications, but most notable is the research in quantum computing. Recently, a high level of control has been demonstrated over the spin in Si including the ability to read spin states.^{72,80}

6. Carrier tunnelling hopping

The study of tunnelling states is useful for understanding the energy level structure in NSs. By varying the bias voltage applied to a NS, one can control which states are allowed to tunnel. In the study of SiO₂-Si superlattices, both phonon-assisted states and lh/hh-states have been observed.^{81,82} Tunnelling can also be considered between QD structures. If the carrier injection rate is large, then Coulomb blockage can occur.⁶⁹ Tunnelling spectroscopy can be used to measure both electron and hole tunnelling, thus giving information about the band gap.⁸³ For more detail, see Ref. 7.

B. Applications of nanostructures

We briefly mentioned some applications of semiconductor NSs in Secs. IA and IA5. This article is not intended to provide a review of the wide variety of applications of NSs, but it does give some representative references for the interested reader. Principally, the advantage of NSs versus bulk materials is the control one has over quantum mechanical states. This control leads to a diverse range of photonic and spintronic applications. In addition, NSs can be used for improved performance in current semiconductor technologies. For a review of the diverse range of applications of NSs, see Refs. 84–86. In the field of photonics, single semiconductor QD fabrication is possible within an optical cavity, which leads to a radical enhancement of the quality factor,^{87,88} including polariton condensates.⁸⁹ Control over the spin states within a NS has lead to a new type of device based on spintronics, including the Kondo effect, and quantum computing applications.^{3,70,90,91} Biological applications include DNA sensing, drug delivery, bio-markers, and pH sensing.^{92,93} A review of Si and Ge-based light-emitting and memory devices is given in Ref. 94. Finally, NSs promise a dramatic improvement in solar cell technology.^{95,96}

C. Comparison with compound materials

Another important class of semiconductor NSs comes from the III-V and II-VI compounds.^{12,97–100} The essential difference between the properties observed in these systems versus Si and Ge is due to their direct gap structure. A direct band gap means these mixed compounds have a higher transition probability (see Sec. IA2) and can be used to manufacture lasers. A disadvantage comes from the toxicity of the materials involved, their cost, and a general not compatibility with current semiconductor fabrication methods.

II. EXPERIMENTAL METHODS FOR THE PRODUCTION OF Si AND Ge NANOSTRUCTURES

Several experimental methods have been used in the last few decades to fabricate Si and Ge nanostructures. We primarily review methods that produce structures with spatial dimensions comparable to the Bohr radius, to discuss quantum confinement in Si and Ge NSs (see Sec. IA1). Here, we highlight the salient features of each method and how they pertain to the final structural, electronic, and optical properties of Si and Ge NSs. In each section for quantum dots

(Sec. II A), quantum wires (Sec. II B), and quantum wells (Sec. II C), a basic account of the particular fabrication method is given in the subsections for each type of NS. Readers familiar with the various fabrication methods may like to skip over these subsections and proceed to the “characterization” sections (Secs. II A1a and II A2a, etc.) where we review the properties of each fabrication method and provide representative experimental results. Section III provides a concise summary of the results discussed in detail here. Reference 101 reviews the advantages and disadvantages of a variety of fabrication methods for potential use in electronic and photonic applications.

A. Quantum dots

QDs have received a great deal of attention in the literature owing to the range of available fabrication methods, together with the diversity for potential applications (see Sec. IB). Here we will discuss a few of the more widely used methods that do not include bottom-up solution-based chemical processing (e.g., colloidal QDs). Solution-based chemical methods are novel from an experimental point of view; however, due to the nature of the process, they contain many impurity states, thus making them difficult to characterize with regard to the intentions of this review article.^{102–104}

The methods we review here can be classified into a few distinct categories. In the case of co-sputtering and plasma-enhanced chemical vapour deposition (PECVD), a sub-stoichiometric oxide is initially produced, whereby QDs phase-separate out of the initial oxide during annealing, Secs. II A1 and II A2. Although the two methods produce a similar oxide state initially, the final properties of the QDs are different. Bottom-up fabrication is achieved using molecular beam epitaxy (MBE) by depositing QDs on the surface of a substrate, which can be subsequently capped, Sec. II A3. In the case of ion implantation, a supersaturation of Si or Ge is implanted in a matrix material; upon annealing the implanted material nucleates thus forming QDs, Sec. II A4. This method is characterized by a high concentration of defects produced during the implantation process. Finally, porous-Si (por-Si) is a top-down method carried out by removing material during a chemical etch, Sec. II A5. In all the above cases, the role of surface or interface states is critical for proper characterization of QDs owing to their inherently large surface to volume ratio.

An important class of Si and Ge QDs is the SiGe alloy of Ge composition x denoted as Si_{1-x}Ge_x. The study of SiGe QDs is a topic for a separate review paper, because of the wide range of properties they exhibit depending on the concentration x .^{24,66,105–111}

SiGe structures have a type II band alignment.¹¹² This alignment leads to strong diffusion between the wetting layer and the QDs, which changes the effective mass from the bulk value.¹⁰⁸ The exact picture of band alignment in SiGe depends on the concentration of Si:Ge.

Si and Ge have multiple valleys in the conduction band, with the minimum located at the X and L-point in Si and Ge, respectively. The CB switches from being Si to Ge-like at $x \approx 0.85$. Si and Ge have a 4% lattice mismatch implying the

existence of strain between layers of different composition. This strain implies a reduced symmetry by breaking degeneracies. For more information about the band structure and general properties of SiGe alloys, see Refs. 113 and 114. The method of MBE fabrication is commonly used to produce SiGe alloys, and we discuss a few of their properties in Sec. II A 3 a. References for SiGe quantum wells are given in Sec. II C.

1. Co-sputtering

First, we review QD fabrication via co-sputtering, covering some basic results. More detailed information can be found in Refs. 115–117. Sputtering based fabrication starts with the deposition of a Si or Ge-rich oxide. This section is focused on co-sputtering, although a similar method denoted reactive sputtering is also discussed. Evaporation^{118–124} and pulsed laser deposition^{125–127} based fabrication methods also produce sub-stoichiometric oxides and therefore have similar properties to sputtering based methods.¹²⁸ Differences arise from the exact stoichiometry of the oxide produced and in the chemistry involved.

Sputtering is the process of removing ions from the surface of a target material via bombardment with chemically inert energetic ions such as Ar⁺. Target atoms are removed by either direct collisions with incident ions or through recoil events with surface atoms. As a result of sputtering, a vapour phase consisting of sputtered atoms is created. To improve the low efficiency of ion-based sputtering, many experimental set-ups use a plasma glow discharge as a sputter source.

A schematic representation of a typical sputtering apparatus is given in Fig. 6. In this set-up, the target material is attached to a negative voltage supply (≈ 2000 V), in the case of a DC bias, while the substrate is positively biased. In the case of an insulating substrate, an RF supply is used in place of the DC supply in Fig. 6. The system is initially pumped down, followed by the introduction of the buffer gas (typically Ar), which leaves the system at a pressure of $\approx 1 \rightarrow 10$ Pa. In the intense electric field, high energy electrons positively ionize the Ar gas creating a glow plasma discharge (for more details, see Ref. 115). The ions are attracted to the negatively charged target material to generate sputtering. In many cases, a magnetron field is generated to

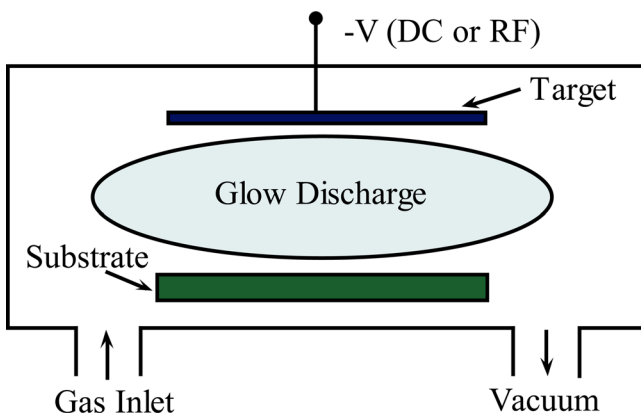


FIG. 6. Schematic representation of sputtering apparatus. A DC source is used for conducting materials or RF for insulating materials.

help increase the ionization efficiency of the buffer gas and help trap ions near the target yielding higher quality films.

Sputtering yield is defined as the average number of surface atoms removed with respect to the number of incident sputtering ions.¹¹⁵ In an SiO₂ target, O is preferentially sputtered.¹²⁹ Therefore, a Si target is used in conjunction with a SiO₂ target to achieve the correct stoichiometric ratio of O and Si during the growth process. This process is known as co-sputtering, whereby chemical reactions occur in the vapour phase. Similar reactions occur in the case of reactive sputtering. In the reactive environment, Si is sputtered in a pre-existing O environment. Still, these two methods yield very different physical parameters (see Sec. II A 1 a). The sputtering process is inherently based on physical deposition. The quality of the deposited film can be described using the structure zone model.¹¹⁷

Several parameters effect the final structure and stoichiometry of the deposited SiO_x or GeO_x film. These parameters include the kinetic energy of the sputtered atoms hitting the substrate, type of particles, flux of particles, growth temperature, sputtering rate, RF power, and pressure.¹¹⁵ As a result, one will observe a wide range of properties (Sec. II A 1 a) between different experimental set-ups. The deposited sub-stoichiometric Si or Ge oxide is thermodynamically unstable, and therefore, annealing will promote the formation of QDs.^{130–132} Thus, annealing causes a sub-oxide state to phase segregate into an amorphous Si or Ge oxide (4⁺) and the bulk Si or Ge (0⁺) state yielding embedded QDs.¹³³ Both Si and Ge QDs produced by this method tend to form crystalline structures.^{134,135} The work of Zhang *et al.*¹³⁶ reported the formation of as deposited crystalline Ge QD in sputtered material. The work of Zhang *et al.*¹³⁶ reported the formation of as deposited crystalline Ge QDs in sputtered material. The stoichiometry of the deposited film also determines the QD diameter. Namely, the QD diameter can be controlled through the sputtering time,¹³⁷ percent composition of sputtered material,^{38,138} and annealing temperature and time.¹³²

a. Characterization of co-sputtered QDs. Si QDs were fabricated using magnetron co-sputtering in the work of Ref. 38. X-ray photoemission spectroscopy (XPS) reveals the Si¹⁺ ion as the dominant interface state, Fig. 7. In comparison, Si QDs produced using reactive magnetron sputtering yield a very different interface structure.¹³³ Reference 133 measured a relatively equal contribution from all three sub-oxide states, Fig. 8. This difference arises due to the nature of the gas environment during the sputtering phase, thus producing slight differences in the stoichiometry and structure of the deposited film. One must also consider variations in the experimental set-up between these two studies. For example, a higher temperature is used during the deposition phase in the work of Ref. 38 compared to Ref. 133, which provides thermal energy for ions at the surface to diffuse more readily.

Co-sputtered Si QDs were produced in Ref. 134, similar to the work of Ref. 38 discussed above. The authors determined that Si¹⁺ (Si-O-Si) states on the surface of the QD acted to quench the non-radiative decay channels and hence

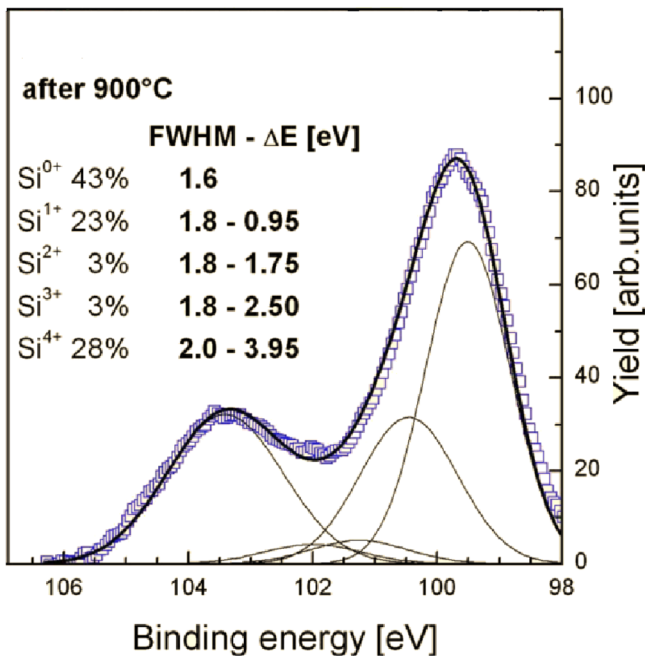


FIG. 7. Si 2p X-ray photoelectron spectra for 43% excess Si fabricated by magnetron co-sputtering, annealed at 900 °C. Best fits are shown depicting the oxidation states with the full width half maximum (FWHM), energy position and percent contribution shown. Reprinted with permission from Mirabella *et al.*, J. Appl. Phys. **106**, 103505 (2009). Copyright 2009 American Institute of Physics.

increase the effect of quantum confinement, Fig. 9. This quenching effect comes about through a coupling of surface vibrational Si-O-Si modes with the lower non-radiative triplet state.¹³⁹ We emphasize that this result is not ubiquitous across experimental set-ups. As noted above, Ref. 133 observed a roughly equal contribution of sub-oxide states. Likewise, Ref. 140 fabricated QDs similar to the work of Ref. 134, and yet the observed photoluminescence is different, presumably due to the existence of different interface states, Fig. 9. Generally speaking, interface states couple with the electronic states in the QD, which leads to the observation of ‘low energy emission’ (1.4 → 1.5 eV).¹⁴¹ ‘High energy emission’ (>1.8 eV) results from defect related states.¹⁴¹ In addition, the interface between the QD and

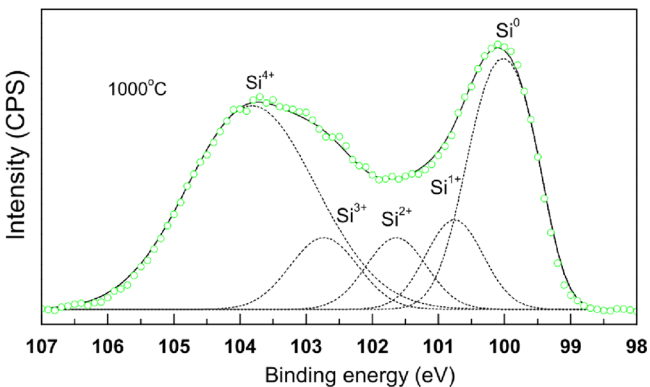


FIG. 8. Si 2p X-ray photoelectron spectra of $SiO_{1.4}$, produced by reactive RF magnetron sputtering, annealed at 1000 °C. The best fit shown depicts sub-oxide states. Reproduced by permission from Zhang *et al.*, J. Cryst. Growth **311**, 1296 (2009). Copyright 2009 by Elsevier Limited.

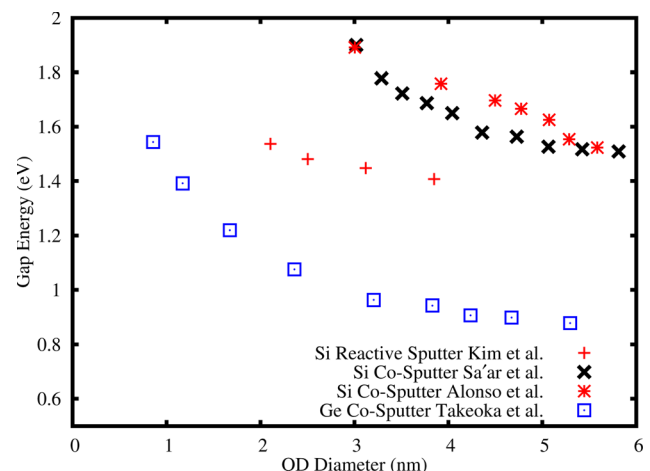


FIG. 9. Variation in the gap energy as a function of QD diameter. Data points are taken from Kim *et al.*,¹⁴³ Sa'ar *et al.*,¹³⁴ Alonso *et al.*,¹⁴⁰ and Takeoka *et al.*¹³⁵

matrix material produces a graded electronic band structure, resulting in a finite confinement potential.¹⁴²

Another effect on the radiative properties of a NS is the stress produced by interfaces. The thicker the NS/matrix interface becomes the more stress one will observe. In the work of Ref. 143, reactive sputtered samples were prepared similar to the work of Ref. 133. In this work,¹⁴³ XPS studies revealed that when the diameter of the QDs was reduced the Si 2p peak shifted to a higher binding energy. Ultimately, the authors determined that the shift in binding energy was due to stress in the system resulting in the observed change of the gap energy (E_g), Fig. 9. The role of stress was confirmed by measuring a Raman shift in the Si^{0+} state at 514 cm^{-1} .¹⁴⁴ However, broadening of the Raman peak also indicates phonon confinement effects.¹³² Similar results are discussed for porous Si in Sec. II A 5.

Though the interface states make it difficult for the observation of clear QC effects, there is direct experimental evidence of such effects. Lifetime measurements by the group of Ref. 130 demonstrate state-filling effects with lifetimes in the microsecond range. Reference 145 observes both fast (nanosecond to picosecond) defect related and slow (microsecond) QC related recombinations. A clear demonstration of singlet-triplet splitting indicative of a two level system is given in Refs. 146 and 147. In addition, direct transitions at the Γ point with a reduction in energy directly related to QD diameter have also been observed.^{31,141}

Ge QDs produced via co-sputtering require one to sputter a Ge sample alongside SiO_2 as a source of oxygen. For this reason, Ge QD formation is generally more complicated than Si due to the thermodynamic instability of GeO_2 (compared to SiO_2), which leads to a higher concentration of defect states. (The role of O on Ge NS formation will be discussed throughout this manuscript.) Oxygen defect states in Ge are similar to their SiO_2 counterparts (see Sec. II A 4), apart from the distinction between O incorporation in the Ge NS versus removal of O states from the SiO_2 matrix.¹⁴⁸ Reference 131 produced Ge QDs via magnetron RF co-sputtering, where XPS measurements indicate a reduction

of GeO_2 as the annealing temperature is raised and an increase in the sub-oxide states,¹⁴⁹ Fig. 10.

The interplane spacing was measured using high resolution transmission electron microscopy (TEM) for Ge QDs with a diameter <4 nm at 0.298 nm, reduced from the bulk value of 0.326 nm suggesting a change in the crystal structure.¹⁵⁰ In this work, the authors suggest that the radiative transitions in their structures are direct with a PL peak energy around 2.3 eV. Similar Ge QDs exhibit a fast ($\ll 1\mu\text{s}$) radiative time.¹⁵¹ The samples of Ref. 150 show broadening and a shift in the Ge crystalline phonon peak via Raman measurements, which is attributed to stress and possibly phonon confinement.¹³⁸ Likewise, Ref. 131 reports a Raman peak at 297.5 cm^{-1} . Ultimately, the PL from Ge QDs has been attributed to E' defect centres and not direct gap transitions.¹³¹

The defect states were controlled in a recently developed procedure by the group of Zhang *et al.*, which is a promising step for Ge QD fabrication.¹⁵² They used a low temperature annealing process where only the substrate was heated. In this work, a superlattice of Ge QDs was fabricated in Ge rich oxide layers buffered by SiO_2 .¹⁵² A thick sub-stoichiometric oxide interface was formed, thus producing highly stressed QDs. Raman measurements indicated

increased stress as the QD diameter was reduced (2.55 GPa for a 7.1 nm QD). Furthermore, the authors measured a blue-shift in the absorption spectrum with decreasing QD diameter. This blue-shift is likely due to the stress in the QDs, in agreement with the results of Ref. 143, noted above.

The PL of Ge QDs produced by co-sputtering can show a large variation in results. In the work of Ref. 153, the authors demonstrate PL due solely to defect states (multiple twin stacks defects are observed). Whereas in the work of Ref. 135, PL due to QC is observed, Fig. 9. In both cases, the samples are produced by magnetron co-sputtering. The essential difference between these sets of samples may be due to the power of the sputtering source, leading to differences in the sputtering yield and hence the Ge concentration. RF powers of 100 and 200 W are used in the work of Refs. 135 and 153, respectively. Zacharias and Fauchet obtained a similar blue (3.1 eV) defect-related PL spectrum from GeO_2 and Ge QDs embedded in an oxide matrix with a subnanosecond lifetime.¹⁵⁴ The ease with which oxygen defect states can form in a GeO_2 matrix implies predominately defect related PL, and increased stress in the QDs will be observed.^{132,135,137,149} Thus, like the case of Si QDs, there exists a large variation in the resulting QD properties, making this preparation method inherently not reproducible from one laboratory setting to another.

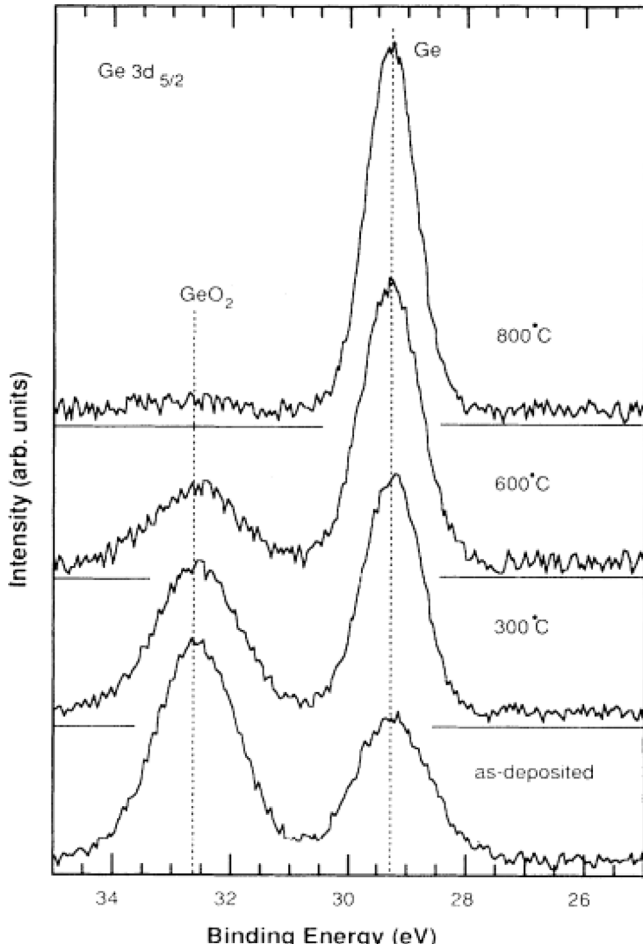


FIG. 10. Ge 3d_{5/2} X-ray photoelectron spectra as a function of annealing temperature. Reproduced by permission from Maeda, Phys. Rev. B **51**, 1658 (1995). Copyright 1995 by American Physical Society.

2. Plasma enhanced chemical vapour deposition (PECVD)

A general overview of QD fabrication via PECVD is given here. More detailed information can be found in Refs. 155–157. Some results pertaining to chemical vapour deposition (CVD) are given below although the focus is on PECVD, which is more widely used due to a higher deposition rate. PECVD is based on the chemical breakdown of silane gas prior to deposition. Microwave plasma decomposition (MPD)^{42,158–160} and laser pyrolysis^{63,161–163} similarly are based on the breakdown of silane and therefore have features in common with PECVD.¹⁵⁶ Essential differences will arise between various experimental set-ups in conjunction with the deposition rate, pressure, and temperature.

Juxtaposed with sputtering (Sec. II A 1), PECVD is an inherently chemical based process, and for this reason, contamination can be an issue of concern. In either case, post high temperature annealing of the deposited sub-stoichiometric film causes phase separation, nucleation sites, and growth of QDs.¹⁶⁴ QD formation in PECVD grown sub-stoichiometric oxide films is a diffusion driven process tending to produce amorphous QDs.¹⁶⁵ A comparison between PECVD and co-sputtering is given in Refs. 38 and 166. Furthermore, CVD can be used to grow surface QD structures,¹⁶⁷ similar to molecular beam epitaxy, Sec. II A 3.

Specifically, CVD is based on the principle of flowing silane, SiH_4 , gas over a heated substrate. The thermal energy induces the chemical reaction: $\text{SiH}_4(\text{g}) \rightarrow \text{Si}(\text{s}) + 2\text{H}_2(\text{g})$ at the surface of the substrate, thus absorbing Si for film growth. In the case of PECVD, a plasma is created in much the same way as described in Sec. II A 1. The plasma or glow

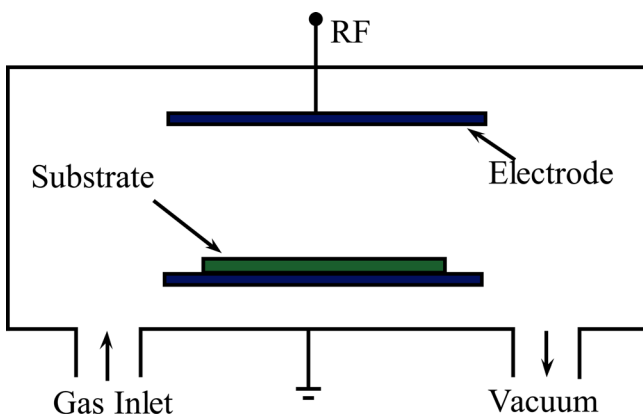


FIG. 11. Schematic representation of plasma-enhanced chemical vapour deposition apparatus.

discharge acts to increase the rate of chemical reactions by providing kinetic energy to the SiH_4 gas to break bonds.

A typical set-up of a PECVD chamber is shown in Fig. 11. The set-up is quite similar to a co-sputtering system apart from there being no target material. In a PECVD chamber, the substrate is placed between two electrodes powered by an RF source. Growth of SiO_x is carried out with the use of SiH_4 , He, and N_2O (or O_2). SiN_x films use SiH_4 , He, and NH_3 (and/or N_2). After the introduction of the gases, a plasma is generated and the typical reaction is: $e^- + \text{SiH}_4 \rightarrow e^- + (\text{SiH}_3)^- + \text{H}^+$. In this ionized state, the gases are more readily attracted to and react with the substrate. It should be noted that the actual chemical process during PECVD is quite complicated and not fully understood.¹⁵⁶

PECVD is characterized by high deposition rates from 3 to 10 nm/min. Parameters that control the quality and structure of the final film include pressure, gas flow, glow (plasma) discharge energy, excitation frequency, RF power, plasma electron density, substrate temperature, and flux of particle species.¹⁵⁶ Surface growth is inherently sensitive to the deposition rate with respect to the relaxation rate of atoms at the surface. These differences of rates can lead to surface irregularities that can propagate through the thickness of the film.

It has been shown that Si-O-Si bonds tend to form during the growth process with a low bond angle.^{156,164} These bonds are stressed and easily break, thus forming defect centres. Inert gases and high temperatures during annealing can help control the formation of defect centres such as Si-H, Si-N, Si-OH, and N-H bonds.^{155,164} Better film quality is achieved in the SiO_x layer when x is not far from 2, which increases the Si-O-Si bond angle.¹⁵⁶ While SiO_x is essential for QD formation, defect free samples are also desired. For higher oxygen content N_2O gas is used, because it has a lower activation energy than O_2 . However, this leads to N contamination in the film, which blue-shifts the optical gap and lowers the absorption efficiency.³⁸

a. Characterization of PECVD QDs. A clear structural difference can be seen between PECVD QDs (Fig. 12) grown at the same atomic concentration as magnetron co-sputtered QDs (Fig. 7), Sec. II A 1 a. XPS measurements confirm the existence of a low concentration of Si-Si bonds

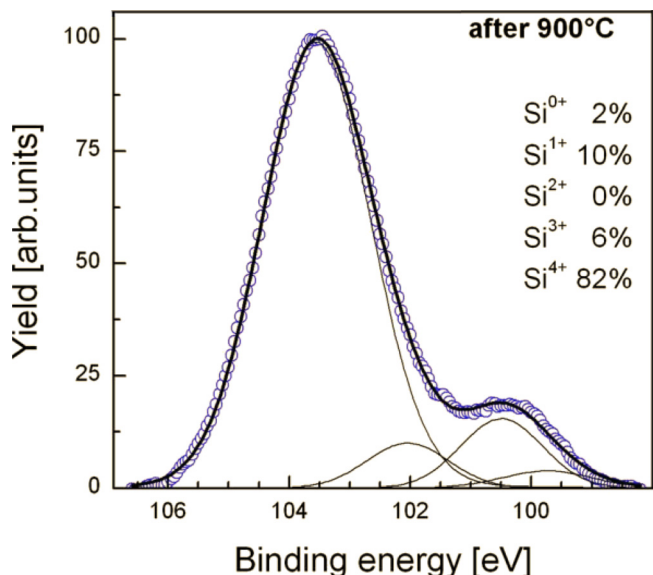


FIG. 12. Si 2p X-ray photoelectron spectra for 43% excess Si fabricated by PECVD, annealed at 900°C. Best fits are shown depicting the oxidation state's percent contribution. Reprinted with permission from Mirabella *et al.*, J. Appl. Phys. **106**, 103505 (2009). Copyright 2009 American Institute of Physics.

for PECVD QDs,³⁸ Fig. 12. The concentration of interface states (Si^{3+} and Si^{1+}) is higher than the Si^{0+} state in the PECVD sample, indicating a thick interface. Due to the thick interface, Raman measurements demonstrate stress in the QDs¹⁶⁸ similar to co-sputtered QDs. In addition, PECVD QDs exhibit a lower concentration of interface states as compared with co-sputtered QDs. This observation is unexpected at first considering the fact that both types of samples are formed via precipitation out of a sub-stoichiometric oxide.

Contamination and defect formation were observed in IR spectroscopy and RBS measurements. Reference 164 produced SiO_x films using source gases of N_2O and SiH_4 . IR spectroscopy measured the Si-O-Si stretching mode at 1028 cm^{-1} for the as-deposited film, which is lower than the bulk value of 1080 cm^{-1} . Subsequent annealing verifies that this mode moves closer to the bulk value indicating that Si is nucleating out of the SiO_x film, thus forming SiO_2 , Fig. 13. Nitrogen contamination was verified through RBS analysis at roughly 10 at. %. Initially, IR measurements detect the Si-N stretching mode (870 cm^{-1}). After annealing the sample, this mode becomes Si-O-N, Fig. 13.

It is clear that impurity defect states do exist in PECVD QDs. While the origin of the defects is different from a co-sputtered sample, they have the same essential effect on the QD structures. The interface-defect states are most likely Si-O-N, based on IR measurements. PECVD QDs demonstrate a notable Stoke's shift between the optical absorption and emission lines due to the interface states.¹⁶⁸ This effect is similar to what was discussed in the case of co-sputtering (Sec. II A 1 a); however, the magnitude of the effect differs due to differences in the interface structure. The observed change in E_G for PECVD QDs is similar to the case of ion implanted QDs (Sec. II A 4 a). Although pinning from interface states has a larger role in the PECVD QD, as noted the change in E_G is minor for QD diameters smaller than

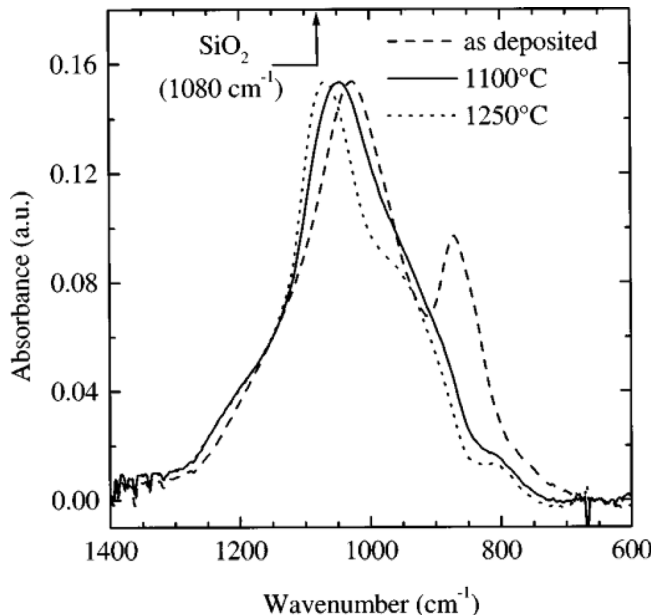


FIG. 13. IR spectrum of an SiO_x film containing 37% excess Si. As deposited, and after annealing at 1100°C and 1250°C shown. The position of the Si-O-Si stretching mode for a stoichiometric SiO_2 film is shown. The Si-N stretching mode is at 870 cm^{-1} . Reprinted with permission from Iacona *et al.*, J. Appl. Phys. **87**, 1295 (2000). Copyright 2000 American Institute of Physics.

2 nm,¹⁶⁴ Fig. 14. Nonetheless, QC effects are still observed albeit minor ones, because of the complicated interplay between stress and interface states in these samples, Fig. 14.

A striking difference is noted when comparing Si QDs embedded in SiO_2 Ref. 164 with ones embedded in Si_3N_4 .¹⁶⁹ Si_3N_4 has a band gap of 5.6 eV, while SiO_2 has a band gap of 8.9 eV. Therefore, one might expect that confinement effects would be stronger in SiO_2 . However, the opposite effect is seen, Fig. 14. The exact reason for this phenomenon is not clear, but it is most likely due to the nature of the interface states. SiO_2 embedded QDs demonstrated a lower change in E_G than most theoretical predictions due possibly to pinning of the VB via interface states,¹⁶⁴ as noted above. Furthermore, a lower bond enthalpy in SiN compared with

SiO implies greater mixing at the interface during annealing,²⁰ thus lowering the confinement strength.^{170,171}

In addition to the interface states, another interesting difference between the SiO_2 and Si_3N_4 embedded PECVD QD is the crystallinity of the structure. TEM images clearly show SiO_2 embedded QD structures as being crystalline.¹⁶⁸ On the other hand, Si_3N_4 embedded QD structures are amorphous.¹⁶⁹ Amorphous structures are known to exhibit stronger confinement, possibly due to a reduction of the effective mass in the amorphous system compared with the crystalline system, and/or due to pinning of valence states in the crystalline system.²⁰ In addition, one cannot discount the large stresses observed in Si_3N_4 embedded QDs.¹⁷⁰

Compared to embedded PECVD QDs, QDs grown on the surface of a substrate show a much stronger blue-shift in the PL energy,¹⁶⁷ Fig. 14. These QDs appear to be characteristic of an amorphous system. Surface grown QDs are based on self-assembly due to strain between the substrate and the deposited material,¹⁶⁷ see also Sec. II A 3. Therefore, the large blue-shift in E_G contains an additional stress component due to the lattice mismatch. In the work of Ref. 167, they cite the theoretical model of Ref. 172, which does not account for the stress component. In addition, a high energy defect band is clearly observed from the substrate material.¹⁶⁶

Ge QDs have been fabricated on the surface of a variety of insulating substrates via a range of conditions within the CVD method.^{173–175} This variability makes it difficult to obtain a clear picture of the final structural and optical properties. Reference 173 reports observing Ge QDs on a N_2O substrates prepared at 550°C and not on other dielectric substrates. Crystalline Ge QDs are reported in Ref. 174, while polycrystalline Ge QDs are reported in Ref. 175. Generally, substrate effects make it difficult to clearly observe QC effects in Ge QDs.¹⁷⁶ Contact with a substrate places large stress on the QD due to lattice mismatch.^{177,178} A similar strain effect is observed in CVD Ge QDs when grown on porous Si.¹⁷⁹

3. Molecular beam epitaxy

A general overview of QD fabrication via molecular beam epitaxy is given here. More detailed information can be found in Refs. 180–182. In the typical set-up, MBE is used to form surface grown QDs sometimes referred to as islands. In this respect, gas source MBE is similar to surface grown CVD structures (Sec. II A 2) or evaporation based methods (Sec. II A 1). The MBE set-up can be used to form islands that can be subsequently capped with typically an oxide layer. An essential feature of these structures is the strain placed on the QDs due to lattice mismatch from the substrate,^{177,178,183} which is required for their growth. This concept of island formation is essentially different from the sub-stoichiometric oxides discussed above, Secs. II A 1 and II A 2.

The principle of MBE growth is fairly straightforward.¹⁸² A simplified schematic of an MBE chamber is shown in Fig. 15. The MBE chamber is pumped down to UHV. Sources can include GeH_4 or SiH_4 , Si_2H_6 or Ge_2H_6 can also be used, which leads to H desorption, but provides a

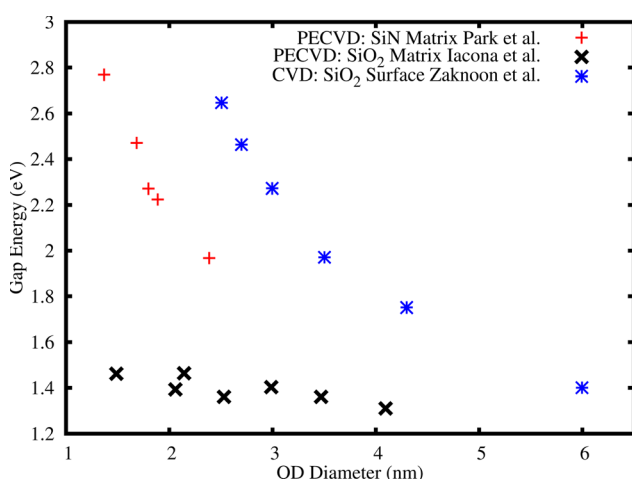


FIG. 14. Variation in the gap energy as a function of QD diameter. Data points are taken from Park *et al.*,¹⁶⁹ Iacona *et al.*,¹⁶⁴ and Zaknoon *et al.*¹⁶⁷

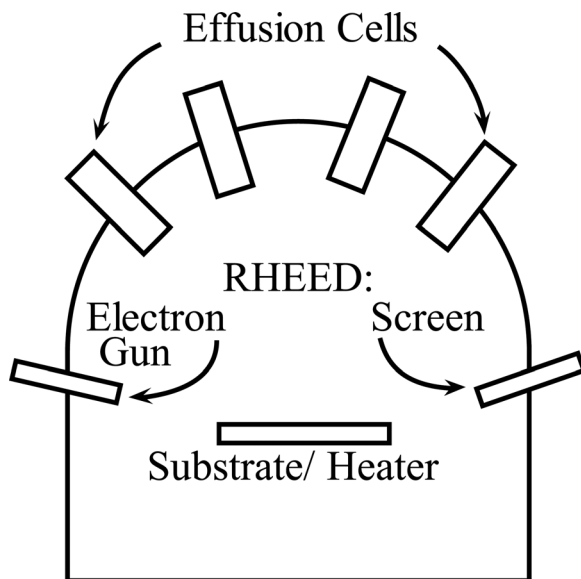


FIG. 15. Schematic representation of molecular beam epitaxy apparatus.

greater sticking coefficient. Typically, Si and Ge decomposition occurs in effusion (Knudsen) cells,¹⁸¹ Fig. 15. The gas is collimated into a beam and directed toward a heated substrate. The particles in the beam travel ballistically and thus undergo molecular flow.¹⁸²

The details of deposition depend on the number of dangling bonds at the surface.¹⁸¹ Once the particles in the beam are deposited on the substrate, the second step in QD formation is migration of the deposited species on the surface prior to their incorporation in the growing material. There are three different growth morphologies:¹⁸⁰ Frank-van der Merwe (FM) morphology via laying a flat single crystal layer (important for quantum well growth, Sec. II C 3), Volmer-Weber (VM) morphology characterized by the formation of 3D islands leaving part of the substrate exposed,¹⁸⁴ and Stranski-Krastanov (SK) morphology with the formation of 3D islands over a complete wetting layer.¹⁸³

When the deposited layer and the substrate have a similar lattice spacing, FM and VM growth can be understood through thermodynamic wetting arguments based on interfacial free energies. If the strain energy due to lattice mismatch becomes larger than the interfacial free energy, then SK growth is favoured.¹⁸³ Strain leads to dislocation defects in the lattice. In the case of Ge on Si(001), strain relaxation happens through dislocation formation through the SK growth mode.¹⁸³ Ge island formation corresponds with the formation of {105} planes, which are accompanied by {113} and {102} planes as the island grow. The formation of defects due to strain is complicated due to the interplay of strain and interfacial energies.

The morphology of the deposited structure is determined by the deposition rate, surface temperature, surface material, and the crystallographic orientation, to name a few growth parameters. If the temperature of the substrate is too low, defects can become a problem. On the other hand, if the temperature is too high, inter-diffusion at the interface between the deposited material and the substrate will occur. Since the chamber is under UHV, one can use reflection high-energy

electron diffraction (RHEED) to monitor the growth process. RHEED provides information about the crystallographic symmetry, long-range order, imperfections in each layer, and whether the growth process is 2D or 3D. Generally, MBE growth yields abrupt interfaces and is highly reproducible, although contamination can be a problem.

Several novel routes toward island formation exist in the literature. Carbon was used to induce Ge QD formation leading to radiative recombination between electrons confined in the underlying wetting layer and holes confined in the Ge islands.¹⁸⁵ Novel shapes were produced using micro-shadow masks on non-planar pre-patterned substrates, though the structures are too large to observe QC effects.¹⁸⁶ Reference 187 produced Si QDs on Gd₂O₃ and capped them with Gd₂O₃, producing a system where tunnelling effects can be observed.¹⁸⁸ In this system, there is little change in the valence band and a large shift in the CB, which is aligned with the CB of Gd₂O₃.¹⁸⁷ Si and Ge QDs grown on LaAlO₃ are reproducible, defect free, form a diamond structure, and exhibit strain at the interface.^{189,190} Sapphire substrates provide a high density of homogeneous Si islands with respect to their dimensions.¹⁹¹

a. Characterization of MBE QDs. As mentioned in Sec. II A, Si and Ge tend to form an alloy, Si_{1-x}Ge_x. In the work of Ref. 192, highly ordered Ge QDs were formed on a Si(100) substrate. The Raman spectrum confirms the existence of a Si-Ge vibrational mode, which is located at the interface of the QD and the substrate. In addition, the Raman spectrum shows a red-shift in the Ge vibrational mode due to strain. These samples show weak confinement effects with a PL band at 0.767 eV. Therefore, the change in E_G is associated with strain effects in the Ge islands. Furthermore, oxide states were found capping the Ge QDs.¹⁹² These results indicate the need for more control during QD formation if QC effects are to be observed.

In another approach, Ref. 193 grew multilayers of weakly strained Ge QDs on SiO₂ with Si layer spacers, where Ge adatoms formed stable islands. These structures exhibit a weak confinement band at \approx 0.8 eV with a type-I band alignment between the Ge QDs and the Si buffer layer. This PL signal was measured at low temperature with a bulk Ge band gap of 0.74 eV.¹⁹⁴ In addition to the low energy PL band, a PL band between 2 \rightarrow 3 eV was also observed. This band is associated with radiative defect states at the Ge/SiO₂ interface, along with stress. In the work of Ref. 195, the same samples as in Ref. 193 were measured using XPS. Ref. 195 measures only the change in the VB position as a function of QD diameter and observes a noticeable shift. The authors claim that if a similar shift in the CB was observed, then the change in E_G would match the work of Ref. 124, Sec. II A 1. The results here are similar to the work of Ref. 192, discussed above.

High quality Ge QD samples were prepared on SiO₂ and TiO₂ substrates, in the work of Refs. 194 and 196. In this work, care was taken to ensure that all sample preparation was done *in-situ*, thus eliminating oxide contamination prior to annealing. Also, the Ge QDs were capped with an amorphous-Si (a-Si) layer. The PL for the two substrates is

similar, Figs. 16 and 17. In either case, weak confinement effects can be seen by a PL band slightly blue-shifted from the bulk E_G and its variation with QD diameter. Since the annealing was done prior to capping the QDs with Si, Raman measurements do not indicate a SiGe vibrational mode.¹⁹⁷ The wide PL band is partly due to defect states from the oxide layer that were relieved during annealing.¹⁹⁶ In addition, Raman measurements do indicate that the Ge QDs are slightly stressed as expected from an MBE set-up.

4. Ion implantation

A general overview of QD fabrication via ion implantation is given here. More detailed information can be found in Ref. 198. Ion implantation is a broad subject of study in itself. An ion beam can be used for a variety of purposes including modifying the properties of a material, causing a phase transformation of the implanted material, and creating silicon on insulator wafers, to name a few. In addition, there is still extensive work under way toward understanding the energy loss process and defect production in implanted materials.^{199,200}

The design of an ion accelerator facility can vary greatly. A schematic of the essential design for an ion accelerator is given in Fig. 18. The principle of operation is the same for all accelerators. Typically, a sputter source is used to produce a gas of ions. The ions are then subject to a potential difference accelerating them to the terminal end and are diverted with a series of magnets (injector magnet, quadrupoles, and high energy magnet). A substrate of any material is placed at the terminal end of the ion beam, denoted as the

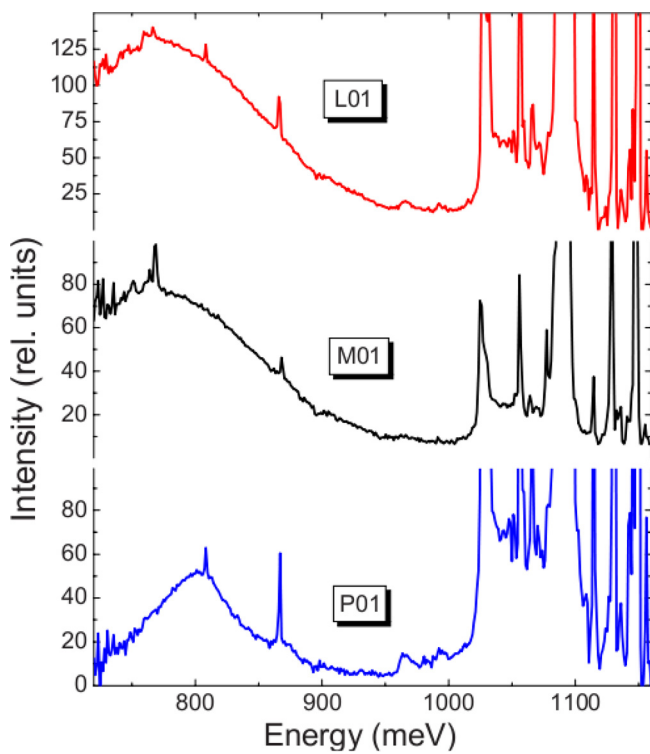


FIG. 16. PL of Ge QDs grown on TiO_2 by MBE and corrected for the PL instrument response. Sample L01 has an average QD diameter of 20.3 nm, M01 20.7 nm, and P01 18.4 nm. Reproduced by permission from Lockwood *et al.*, J. Electrochem. Soc. **157**, H1160 (2010). Copyright 2010 by The Electrochemical Society.

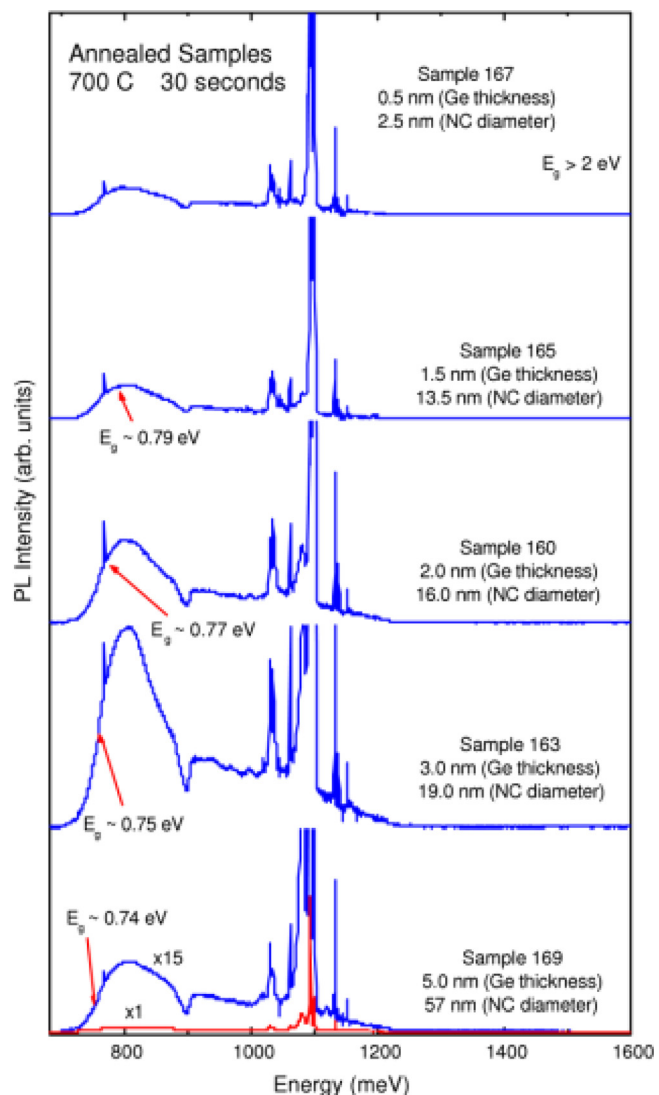


FIG. 17. PL of Ge QDs grown on SiO_2 by MBE and corrected for the PL instrument response. The Ge QD size is given in the figure. Reproduced by permission from Rowell *et al.*, Superlattices Microstruct. **44**, 305 (2008). Copyright 2008 by Elsevier.⁴²⁵

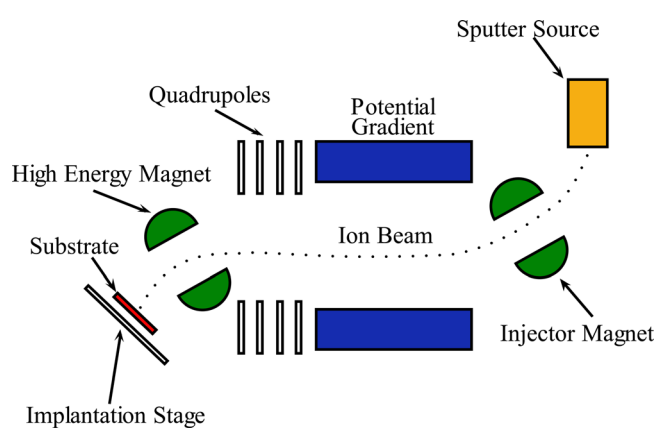


FIG. 18. Schematic of an ion accelerator. The sputter source produces an ion beam. The injector magnet selects the correct ion charge to be accelerated through a potential gradient. The quadrupoles and high energy magnet focus and direct the beam to a substrate on the implantation stage.

“implantation stage” in Fig. 18. During implantation, the beam energy, dose of implanted ions, substrate temperature, pressure, angle of incidence, and beam current are all precisely known.

QD formation in this set-up happens through the proper control of the implantation energy, dose, and the correct annealing conditions. From the implantation energy and dose, the implanted ion concentration at a certain depth can be determined using the program SRIM.¹²⁹ Typically, the concentration needs to be on the order of $10^{21} \rightarrow 10^{22}$ atoms/cm³, requiring a dose on the order of 10^{16} atoms/cm². Following implantation, QD formation is facilitated by annealing the substrate, thus giving enough thermal energy to the implanted ions for diffusion. The actual details of QD formation can be quite complicated, because of the nature of defects produced during the implantation step. Notably, defects in the Si QD nucleation zone facilitate the formation of QDs via a transient enhanced diffusion mechanism.^{199,201} The defect concentration varies with depth, leading to a depth profile of QD size and concentration, which can be investigated by depth resolved PL.²⁰² In addition, during the annealing step, Si QDs oxidize, implying the formation of a thick interface.²⁰³ However, there are good models for the formation of QDs during annealing.^{204–206} The most effective way to control the size of the QD is to vary the implantation dose, thus varying the amount of material available for nucleation.²⁰⁶ The QD size can also be affected by the thermal budget.²⁰⁴

Many authors have considered a variety of implantation conditions. It should be noted that variations in the implantation conditions will produce QDs with different structural properties, while a range of implantation conditions do still produce QC-related PL, see Sec. II A 4 a. A secondary implantation with a high dose leads to a high defect concentration.²⁰⁷ Reference 208 uses rapid thermal annealing to enhance the PL intensity. High temperature implantation will allow many of the defects produced during the initial implantation step to diffuse.²⁰⁹ Multiple implant energies create increased defect based PL.^{210,211}

Ion implantation is fundamentally different from both co-sputtering (Sec. II A 1) and PECVD (Sec. II A 2). In the latter two cases, one produces a sub-stoichiometric SiO₂ or GeO₂, whereas ion implantation produces a super-saturation of Si or Ge in a matrix material (often SiO₂). These differences lead to different growth kinetics and thermodynamics and produce different interface structures. Defect-interface states (which were discussed in Secs. II A 1 and II A 2) form as the Si⁰⁺ phase separates from the initial sub-oxide deposited layer. On the other hand, ion implantation is characterized by the production of a large number of oxygen vacancy defects in the matrix material, discussed below. As mentioned, these defects enhance the mechanism of QD formation and finally the formation of the sub-oxide interface states. In principle, all defect types (point, line, planar, and volume) including radiation induced defects during implantation can be observed; see Chaps. 7 and 9 of Ref. 198. In addition, the implantation process causes sputtering along with swelling of the substrate material with a net effect of around 1 nm for typical energy and dose ranges.²¹²

A comprehensive study of defects in SiO₂ is given in Ref. 213. Oxygen vacancy defects, V_O, are represented as O₃≡Si—Si≡O₃. When the bond between the Si atoms is broken, through electron excitation or hole capture, this defect becomes positively charged, V_O⁺, and is called an E' centre defect, represented as O₃≡Si•—Si≡O₃ (• is an unpaired electron and ○ is the trapped hole). A study of E' centre defects at the interface of Si and sub-stoichiometric SiO₂ as a function of the annealing condition is given in Ref. 214. The dominant defect observed after implantation into SiO₂ is the E' centre defect.²¹⁵ This state is reported to be a non-radiative recombination centre, thus quenching the PL from Si in an as-implanted sample. However, there is PL emission observed from the neutral V_O at 470 nm,^{215,216} Fig. 19. In addition, there is PL from nonbridging oxygen hole centres (NBOHC), denoted O₃≡Si—O[•]. This defect has a PL band around 630 nm,²¹⁵ Fig. 19. The defect-associated PL is removed by annealing the sample, allowing the reconstruction of the SiO₂ structure and formation of QDs²¹⁷ (see PL curve obtained after annealing at 1100 °C in Fig. 19). There is the potential for the formation of other defect structures including double defects.²¹⁸

We noted that implantation produces E' centre defects. During the nucleation phase of Si in SiO₂, these defects are almost completely removed and crystalline QDs are observed,^{204,215,219} Fig. 19. Defect production and removal is studied in Ref. 220 establishing a model relating the number of non-radiative centres, PL intensity, and lifetime. It is clear that not all defect states can be removed, because there must exist an interface between the Si QD and the matrix, which will contain sub-oxide states. The most notable state is the P_b defect, which is an under-coordinated Si atom (Si₃≡Si[•]) and is detected in an annealed sample.²¹⁵ Three different charge states exist for the P_b dangling bond defect: D⁺, D⁰, and D⁻ corresponding to zero, one, or two electrons

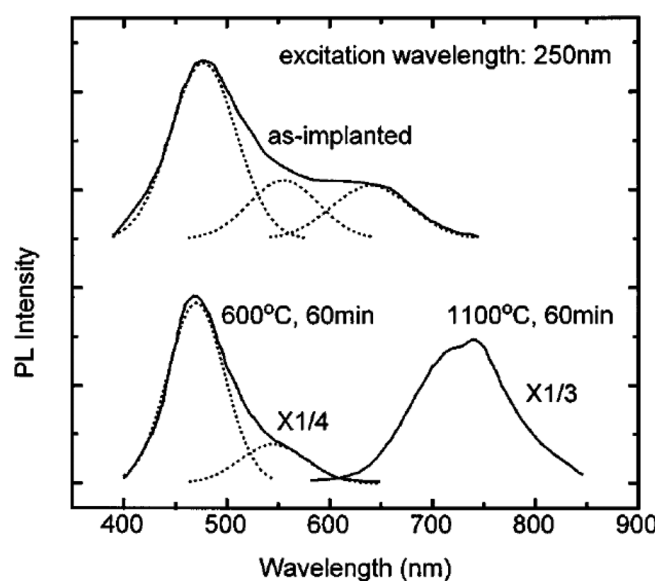


FIG. 19. PL spectra for an as-implanted SiO₂ substrate with Si, and annealed at 600 °C and 1100 °C. The defect bands are shown by the dashed curves at 470, 550, and 630 nm. Reproduced by permission from Song and Bao, Phys. Rev. B 55, 6988 (1997). Copyright 1997 by American Physical Society.

in the dangling bond, respectively. The positive charge state pulls the under-coordinated Si atom into the plane of the other three Si atoms, while the negative charge states have the opposite effect,⁷ which can cause stress in the system. These defect states also act as non-radiative traps; however, they can be controlled by annealing in forming gas (95% N₂:5% H₂), which acts to passivate the dangling bonds.²²¹ Such an anneal increases the PL intensity without causing a shift in the peak position. The interaction of P_b defects with molecular hydrogen is studied in Ref. 222.

Another substrate material that researchers have looked at for both Si and Ge is Al₂O₃, because of its optical transparency. However, QD formation is difficult in this matrix material. Also, Al₂O₃ is a highly contaminated material from the manufacture. In the case of Si implantation, a PL band around 750 nm was observed, but this same band was also observed in the unimplanted sample.²²³ In the case of Ge, one observes significant out-diffusion of Ge and stress.^{224,225}

a. Characterization of ion implanted QDs. While dangling bonds at the interface can be passivated, suboxide interface states will still exist. In the work of Ref. 212, the Si³⁺ state, Si₂O₃, was found at the interface with a concentration that depends on the implantation energy and dose. This state was observed in the work of Ref. 5, where it was also noted that the interface is sharp as compared to co-sputtered and PECVD QDs, Figs. 7, 8, 12, and 20. For a high-dose low-energy implant, the interface state has a low

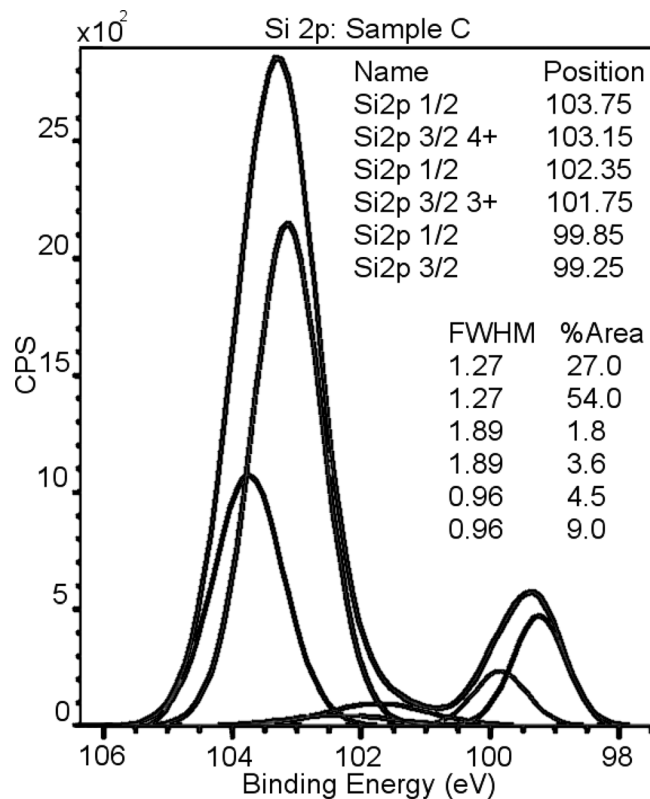


FIG. 20. XPS spectra of the Si 2p state for Si QDs embedded in SiO₂ formed by ion implantation with an average QD diameter of 1.7 nm. Oxidation states are labelled in legend. Reproduced by permission from Barbagiovanni *et al.*, Phys. Rev. B 83, 035112 (2011). Copyright 1997 by American Physical Society.

concentration, while the opposite is true for the high-dose high-energy implant.²¹² When the sub-oxide interface is thick, the system is under increased stress.²²⁶ The interface thickness can be controlled and stress is generally relieved with annealing.⁵ Similar to our discussion in Secs. II A 1a and II A 2a, the interface states couple to electronic states in the QD. These states are noted to exist as mid-gap states where primarily the Si-O vibrational mode (0.13 eV) was observed to cause a Stoke's shift between the PL emission and absorption, and caused pinning of the VB states,^{134,219} Fig. 21.

Fig. 21 demonstrates differences in the observed PL for different implantation conditions. As mentioned above, high energy and high dose implants can produce many interface defect states, and this condition leads to increased stress in the QDs. Comparing the work of Refs. 219 and 227, a larger blue-shift of E_G is noted in the case of Ref. 227 as seen in Fig. 21. In the case of Ref. 227, multiple implant energies are used, which increases the concentration of defect states produced in the matrix material. This measured PL is comparable to that from PECVD and sputtering samples due to the nature of the complicated interface. In the work of Ref. 219, the interface is noted to cause a Stoke's shift between the PL and absorption spectra. PL from Ref. 199 shows a much smaller change in E_G with the use of a moderate implantation energy. These samples were analyzed in the work of Refs. 5 and 20, where it was found that these samples have an Si³⁺ interface state, are crystalline, and likely experience a pinning due to the interface states.

Si QDs formed by ion implantation also exhibit complicated decay dynamics, owing to their high packing density. Size dependency of the radiative lifetime and non-linear state-filling effects are reported.^{30,228} A stretched exponential decay in the radiative lifetime is characteristic of the existence of multiple decay channels.²²⁹ Some of these channels include tunnelling effects and defect states. Fast and slow time-resolved PL similar to Sec. II A 1a is observed due to high energy interface states and low energy QC states.^{43,230}

While Si QDs can be controlled through proper implant and annealing conditions, Ge does not produce such well

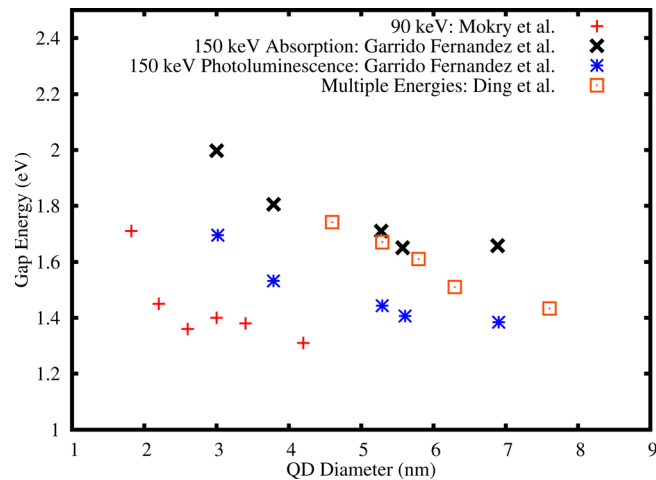


FIG. 21. Variation in the gap energy as a function of QD diameter for Si implantation at different energies in a SiO₂ matrix. Data points are taken from Mokry *et al.*,¹⁹⁹ Garrido Fernandez *et al.*,²¹⁹ Ding *et al.*,²²⁷

defined PL. Ge more readily diffuses leading to desorption during annealing compared with Si.^{225,231,232} Ge easily oxidizes; thus, in the neutral V_O defects formed after implantation, Ge is able to substitute the place of Si in either one or two positions and readily desorbs.^{233,234} In addition, Ge remains stressed after annealing partly due to incorporation in the matrix material.^{234–236} Therefore, after annealing, the only PL observed is defect related PL around 350 nm and 450 nm.²³⁷ In addition, red PL has been observed for Ge implanted in SiO_2 . However, it has still been attributed to V_O defects at the interface.^{238–241}

5. Porous silicon (por-Si)

A general overview of fabrication via chemical etching to form por-Si is given here. More detailed information can be found in Ref. 242. Fabrication of por-Si spawned much of the original interest in NSs and the desire to explore a range of fabrication methods. The number of publications on this subject is staggering, and it is not possible to cover them all. Similar to the case of ion implantation (Sec. II A 4), there are a wide range of conditions that one can use to fabricate por-Si NSs.²⁴³ Traditionally, there was much debate about whether por-Si structures are more wire or dot-like.²⁴⁴ Generally speaking, short chemical treatments form QDs, while longer treatments lead to the formation of Q-wires.²⁴³ Annealing in an O environment forms SiO_2 on the surface that will consume the inner Si core, thus forming spherites,²⁴³ Fig. 22. A spherite is described as a state in between a QD and a Q-Wire, like an “American football” or a “Rugby ball.”

In this section, we describe por-Si results that exhibit properties closer to those of QDs. In Sec. II B 3, we discuss por-Si Q-Wires, but it is understood that many of the properties of a por-Si Q-wire and a QD are the same, apart from the dimensionality of confinement. The PL data generally lies close to a model for Q-wires, though in some cases it may lie between the Q-wire and QD model (see Sec. II B 3, Fig. 30). Therefore, much of the information presented here carries over to Sec. II B 3. A few review articles on por-Si are Refs. 75, 243, 245–249.

In principle, the process of por-Si QD formation is quite straight forward. Different planes in the Si crystal structure etch at different rates leading to the formation of irregular structures when etched. However, most etching is unidirectional and perpendicular to the substrate surface. Still, etching creates a rough surface. When pores sizes are down to a few nanometres, it becomes energetically favourable for the hole to etch Si at the bottom of a pore, thus elongating an irregular nanometre thick wire.²⁴⁹ This etching leads to the

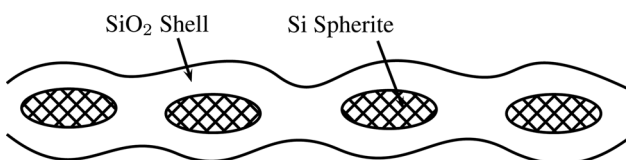


FIG. 22. Schematic of Si spherite formed by oxidation of a por-Si Q-Wire. Note that the spherite is dimensionally an elongated quantum dot.

formation of pores that are regularly oriented with an average pore diameter.

A piece of Si can be etched using chemical, photochemical, or electrochemical methods.²⁴² Purely chemical based etching using an HF solution is very slow, and this can be speeded up by using an electrochemical method.²⁴³ Electrochemical methods are frequently used for QD formation, while a purely chemical method gives greater control for the formation of Q-wires.^{243,250} Pure chemical etching yields great variability in the properties of the final sample, while galvanostatic anodization improves sample quality.²⁴² Ethanol is frequently used with HF to improve wetting of the substrate.

There are several different reactions occurring during electrochemical etching, but it is clear that it leads to oxidation of the surface and the formation of silicon hexafluoride.^{242,247} Initially, the surface is H terminated, but this is only a metastable state and leads to oxidation upon exposure to air. por-Si structures have a large surface area, and passivation (with H or O) of the surface changes the observed PL, Fig. 23. Other passivation methods include organic species.^{242,251} The nanoscale architecture (porosities, pore sizes, and surface area) depends on the doping of the Si substrate (e.g., spongelike for p-type substrates and columnar for n-type, Ref. 248), fluoride concentration, current density, and anodization time.²⁴²

There has been much debate as to the exact mechanism of radiative transitions in por-Si.²⁴³ Much of this has to do with the fact that por-Si leads to a complex surface chemistry, described above. In addition, large-scale structural inhomogeneities lead to broadening in the reported lifetimes and an increased exchange splitting, which can suppress radiative states.²⁴³ Nonetheless, it has been shown that no-phonon processes can dominate in por-Si under the condition of a strong confinement potential.^{25,26,75} Also, increased etching leads to a blue-shift in the radiative energy.²⁴³ We will focus on some of the general features of por-Si that, when fabricated appropriately, do allow for the observation of QC.

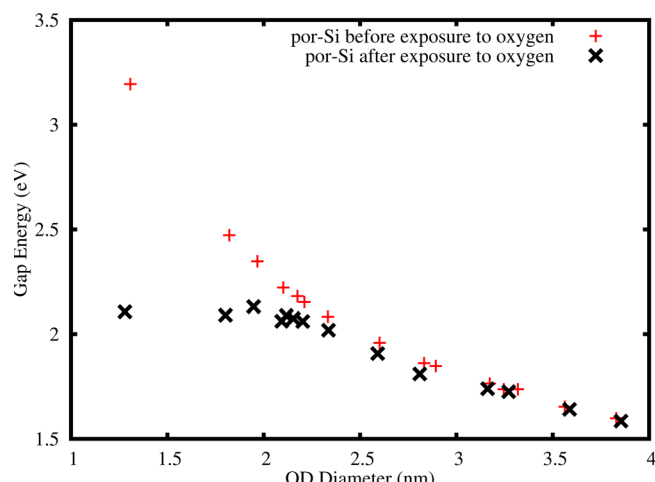


FIG. 23. QD size dependence of E_G in por-Si samples reported in Ref. 252. “Before exposure to oxygen” refers to samples kept in an Ar gas environment, eliminating surface oxide states. “After exposure to oxygen” refers to oxidized samples, where the effects of surface pinning due to localized states in $\text{Si}=\text{O}$ are seen.

a. Characterization of por-Si QDs. The effect of oxidizing the surface of por-Si was clearly demonstrated in the work of Ref. 252. In this work, when samples were kept under an inert Ar atmosphere there was a clear trend in the peak PL energy shifting to the blue with increased QC, Fig. 23. When the samples were exposed to air, there was a red-shift in the PL spectrum for most of the original porosities, Fig. 23. The authors attribute this shift to three different regimes in the recombination mechanism. At QD sizes larger than 3 nm, they conclude that the PL is from free excitons. Between \approx 1.7 and 3 nm, the radiative recombination comes from an electron localized on a Si=O (Si^{2+}) bond and a free hole. For less than \approx 1.7 nm, the PL is from an electron and hole localized on a Si=O bond. This observation indicates that if the samples are not passivated with H, then one can expect to observe QC in a very limited range of QD sizes.

The effect of surface state vibrational modes along with phonon effects has been extensively studied. In the work of Refs. 56 and 75, phonon resonances were observed in the PL band. It is likely that the phonon resonances are due to the inhomogeneous broadening of the porosity. However, single QD PL spectroscopy was carried out verifying that emission is atomiclike with the observation of TO-phonon modes along with a replica mode at 6 meV.²⁵³ This second mode is responsible for the ‘broad’ PL spectrum from single QD emission at room temperature. Vibrational modes are also seen as a shift between PL and absorption (discussed in Secs. II A 1 a and II A 4 a) as seen in Ref. 254, Fig. 24.

In the above sections, we have mentioned the influence that a thick oxide interface has on the optical properties of NSs. Stress placed on por-Si due to the surrounding oxide was studied in the work of Ref. 255. They found an increasingly large tensile stress on the surface with increasing

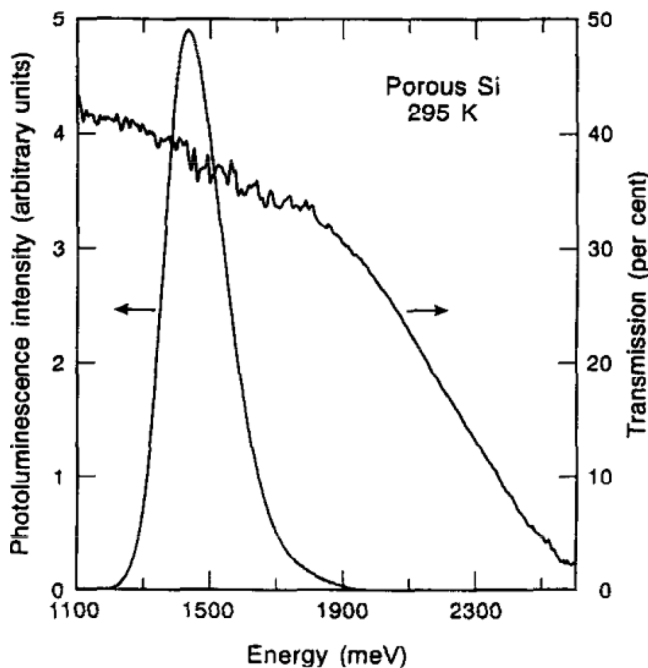


FIG. 24. Transmittance and photoluminescence spectra for por-Si comprised of 3.1 nm diameter spherites. Reproduced by permission from Lockwood *et al.*, Solid State Commun. **89**, 587 (1994). Copyright 1994 by Elsevier Limited.

porosity, which decreased in the radial direction, along with a compressive component at the interface with the Si substrate. Raman spectra indicate a very broad peak that is red-shifted from the bulk peak position,^{254,256} Fig. 25. Stress in por-Si samples was modelled in the work of Refs. 257 and 258 using a bond order length correction model. The por-Si samples studied showed PL due to QC states.²⁵⁷ Nonetheless, due to the complicated nature of the interface, it was found that a model which included a modification to the coordination number due to imperfect surface states improved the fit with experimental data. This model includes stress to the Si-Si bonded states, which contract by \approx 20% at the surface as measured by a Si 2p shift in the XPS data.

Oxide states are also noted, with respect to the radiative properties of por-Si. Radiative lifetime measurements reveal a fast (defect related) and slow (QC related) lifetime component.²⁵⁹ The fast and slow components exist in a freshly prepared sample of por-Si, while an exclusively fast component exists in an oxidized sample. Spectral hole burning measurements report two TO phonon modes.²⁶⁰ Increasing the sample temperature of the PL measurements heals the spectral hole in accordance with exchange splitting and indicates that radiative PL comes from QC states. In addition, Ref. 261 reports tunnelling through oxide-connected spherites. Therefore, it appears that surface/interface oxide states play an important role in por-Si. The effects are readily seen, because the etching process creates a much larger surface area of dangling bonds for O to bond with. Indeed, a relationship between the ratio of Si-O:Si-H bonds and the observed PL has been reported.²⁴³

B. Q-Wires

Q-Wire research focuses principally on the electron transport properties, e.g., for use in transistor applications.^{11,262,263} In general, Q-Wires are not ideal for optoelectronic applications, because they have a high defect concentration leading to a high scattering rate.¹¹ Nevertheless, there has been a

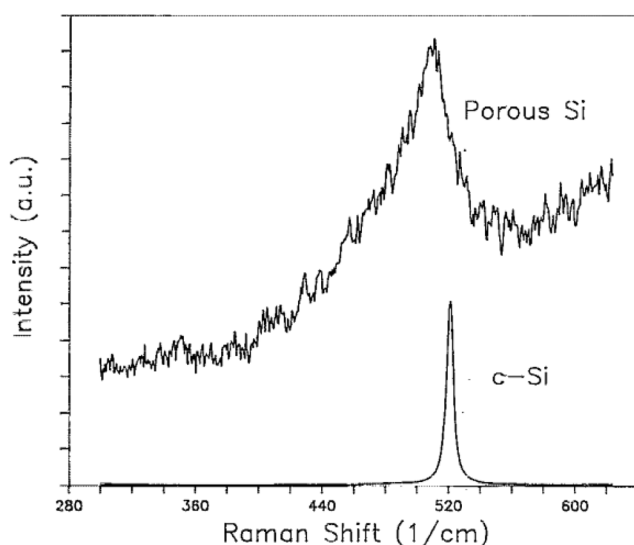


FIG. 25. Raman spectrum of por-Si compared with crystalline Si (c-Si). Reprinted with permission from Sui *et al.*, Appl. Phys. Lett. **60**, 2086 (1992). Copyright 1992 American Institute of Physics.

concerted effort to engineer functional devices.^{245,246,263,264} Traditionally, vapour-liquid-solid (VLS) growth and oxide assisted growth (OAG) produce wires that are on the order of tens to hundreds of nanometres in diameter,^{19,265,266} making it difficult to observe QC effects. Recent work on the OAG method produced Q-wires on the order of a few nanometres,⁸³ and por-Si wires tend to be of a similar diameter.^{243,244,248}

1. VLS technique

The vapour-liquid-solid growth method was originally described in Ref. 267. In principle, the details of VLS growth can be quite complicated, but control over the physical properties of the Q-Wires is fairly well understood.¹⁹ Details of Ge Q-Wire growth are given in Refs. 268–270.

VLS growth produces single crystal and highly anisotropic Q-Wires of fairly uniform diameter with little or no amorphous oxide.^{271,272} A catalyst particle (typically Au, although other materials can be used) is deposited on a substrate.^{19,273} At this stage, the rate of change of the radius of the Q-Wire ($\frac{dr}{dt}$) is positive.²⁷⁴ A gas source of silane or germane is continuously supplied to the catalyst particle to form a eutectic liquid droplet (the phase diagram for the eutectic state is given in Ref. 270 for Ge and in Ref. 19 for Si). Note that while eutectic point is often used to describe phenomena accompanying the growth, typical growth temperatures are higher than predicted by bulk phase diagrams. The eutectic point has a lower activation energy for nucleation, and thus growth in the axial direction happens only at the catalytic site ($\frac{dr}{dt} \approx 0$), where material is transported to the eutectic droplet/Q-Wire interface. The radius can taper ($\frac{dr}{dt} < 0$) if no material is supplied or the temperature is reduced.²⁷⁴ (NB: In certain cases a related growth method called solution-liquid-solid (SLS) is proposed as the growth mechanism, where Q-Wire diameter control is an issue.²⁷⁰)

There are two interfaces that determine the Si-wire growth conditions.²⁶⁵ There is a gas (reactant) solid (substrate) interface implying vapour-solid growth and thickening in the radial direction through dissociative adsorption. Second, there is a liquid (eutectic) solid (Q-Wire) interface implying vapour-liquid-solid growth in the axial direction. The dominant interface depends on the pressure, gas flow rate, temperature, reactant species, and any background gases.²⁶⁵ H can mitigate radial growth by terminating the Q-Wire surface and also reduce roughening.²⁶⁵ Therefore, one has a high degree of control over the radial/axial directions.

The Q-Wire diameter is connected with the growth axis.^{272,275} The observed growth axis is based on minimizing the total free energy. For a Si plane of (111), the growth direction is $\langle 111 \rangle$. Changing the pressure during growth will alter the growth axis and thus change the diameter.^{276,277} For Au catalysed Q-Wires, small, medium, and large Q-Wires are associated with the $\langle 110 \rangle$, $\langle 112 \rangle$, and $\langle 111 \rangle$ directions, respectively.²⁷² For silicon wires of relatively small diameter, the lateral surface energy contributions dominate over the Au/Si interface energy, and its minimization determines the preferential growth direction.

In addition, the growth axis determines the defect structure.²⁶⁶ (001) is the second lowest energy plane, implying

that (001) facets can appear along with (111) facets. High concentrations of stacking faults and twin defects are observed in VLS Q-Wires.²⁶⁶ Growth temperatures below the eutectic point will introduce more defects, whereas high temperatures generally produce high quality crystalline Q-Wires.²⁷⁸ Other defects arise from contamination due to the Au-catalyst, which introduces deep level defects in either Si or Ge.^{19,279}

a. Characterization of VLS Q-Wires. Ge Q-Wires experience several complications from the surface oxide layer. Generally, no oxide will form on the surface of the Q-Wire, but depending on the annealing conditions a thick oxide can change the Q-Wire core into NS spheroids.²⁶⁶ The growth substrate is typically Si with a native oxide layer. This native oxide reacts with the Ge forming a GeO_x sheath around the Q-Wire.²⁶⁹ The additional oxide is removed with HF, but will return with prolonged exposure to air.²⁶⁹ An oxide layer leads to stress in the Q-Wire as clearly seen in Raman measurements.²⁸⁰ Furthermore, O related defect states are seen in Ge Q-Wire photoluminescence measurements,²⁸⁰ Fig. 26. Therefore, direct observation of QC is difficult in Ge Q-Wires as transitions near E_G are not observed.^{279,281} Thus, any observed shift in the optical absorption or emission energy is likely associated with changes in O defect states due to stress. Note that the origin of these complications is similar to what was described in Sec. II A for Ge QDs. However, since the growth method produces an exposed surface with a high volume of dangling bonds, one expects an increased role from the oxygen states at the interface.

Si VLS Q-Wires suffer the same oxide problem as their Ge counterpart. In the work of Ref. 276, Si Q-Wires of varying diameter were made by changing the pressure according to the principles described above. VLS Si Q-Wires of 4 and 5 nm diameter were made and produced a strongly blue-shifted PL signal at 3.75 and 3 eV, respectively.²⁷⁶

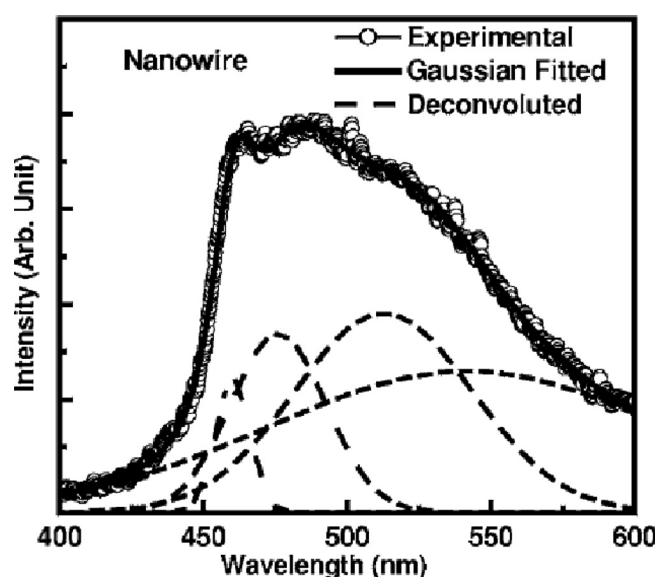


FIG. 26. PL of VLS Ge Q-Wires grown at 700 °C. Reprinted with permission from Das *et al.*, J. Appl. Phys. 101, 074307 (2007). Copyright 2007 American Institute of Physics.

Considering the fact that the Q-Wire diameter is on the order of the Bohr radius for Si, it is not likely that this large shift in the optical gap is due to QC, but rather oxide defect states.²¹³ A similar defect related PL is seen in the work of Ref. 282, Fig. 27. In the work of Ref. 283, it was shown that defect related PL increases by increasing the oxide thickness.

A thick oxide layer is known to increase E_G by increasing the stress in the system.²⁸⁴ Thus, if one takes caution to remove the oxide layer, then QC PL should be observed. In the work of Ref. 278, defect free Q-Wires were produced and QC states were observed solely through an increase in the full width half max of the Raman spectrum. PL potentially due to QC was shown in the work of Ref. 285, where the authors observe an optical gap at 1.9 eV for Q-Wires of diameter 4.9 nm. However, this PL demonstrates a larger shift in E_G than expected for Q-Wires of the stated size. It is also possible that Q-Wires of this size exhibit a direct band structure;²⁸⁶ however, this behaviour has not been observed directly.

2. Oxide assisted growth

The oxide assisted growth method produces a higher density of Q-Wires in comparison with the VLS method; however, diameter control is a challenge.²⁸⁷ Control over the outer oxide thickness yields wires with a thin Si core, where a clear demonstration of QC is given in Ref. 83. The details of OAG can be found in Refs. 19, 266, and 289. Ge OAG Q-Wires undergo a similar process of formation as with Si.^{290,291} Ge Q-Wires still suffer from oxide defect states, stress, and other defects during formation^{290–292} similar to VLS Ge Q-Wires.

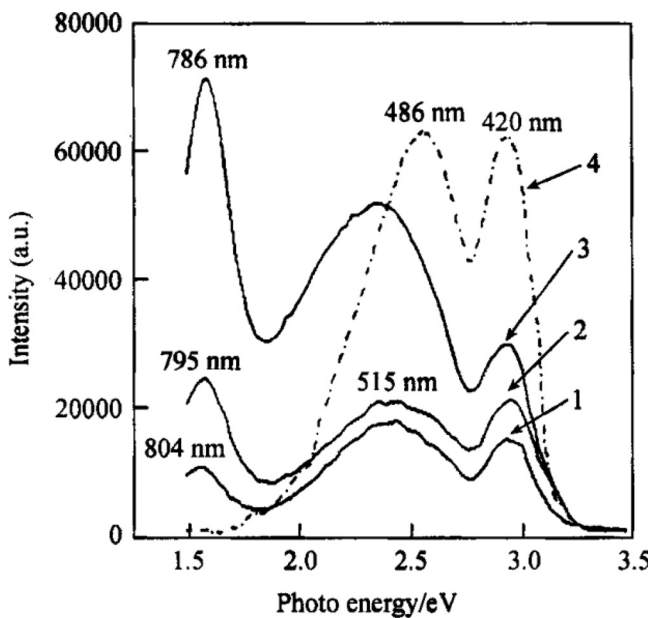


FIG. 27. PL spectra of VLS Si Q-Wires annealed under different oxidation conditions. Sample 1 is as-grown, sample 2: 700 °C for 5 min., sample 3: 700 °C for 10 min., and sample 4: 700 °C for 15 min. Reproduced by permission from Sunqi et al., Sci. China Ser. A 42, 1316 (1999). Copyright 1999 by Springer.

OAG does not use a metal catalyst and for this reason does not suffer from deep defect states as in the case of VLS growth. Some work has been done using a metal catalyst in conjunction with OAG.²⁹³ First, a gas of SiO is generated by either heating Si and SiO₂ at 1200 °C via the reaction: Si(s) + SiO₂(s) → 2SiO(g), or by laser ablation.²⁹² SiO gas is generated in a tube furnace under a flowing inert gas environment, which causes the SiO gas to flow downstream through a thermal gradient to a region of lower temperature. In the second stage, the SiO decomposes on the substrate surface through two reactions: Si_xO(s) → Si_{x-1}(s) + SiO(s) ($x > 1$) and 2SiO(s) → Si(s) + SiO₂(s). Therefore, Si dangling bonds form on the Si substrate, which act as nucleation centres for Q-Wire growth.

Si-Si bond formation is preferred for Q-Wire formation. The reactivity of Si-Si bond formation is determined by the stoichiometry of the system; see Fig. 10.5 of Ref. 289. O in the SiO clusters diffuses to the surface of the Q-Wire to form a SiO sheath, which is terminated by SiO₂, thus limiting radial growth.²⁹⁴ In the [112] orientation, diffusion of O is lower and so this direction is a reactive surface of Si_xO, which is the dominant axial growth direction.^{294,295} Variations in the pressure can also be used to control the orientation of the Q-Wires.²⁹⁶

During growth a high density of stacking faults along the ⟨112⟩ direction is produced.^{19,266,289} These defects include micro-twins and dislocations, which facilitate fast Q-Wire growth.²⁹² Fig. 28. In addition, the formation of {111} surfaces (lowest energy surface) parallel to the axis of growth facilitates the formation of SiO₂, which retards growth in this direction. Therefore, OAG Q-Wires are comprised of a Si core surrounded by a sub-oxide layer, which is terminated by SiO₂. This method leads to a large number of defects in the Si Q-Wire including oxide defect states as seen in the PL spectrum.²⁹² These defect states are potentially removed with an additional annealing step. However, annealing increases the oxide thickness, producing stress in the Q-Wire.^{83,287,292}

a. Characterization of OAG Q-Wires. Novel growth was achieved in the work of Ref. 288, where zeolite is used to limit radial growth. This method leads to the formation of a

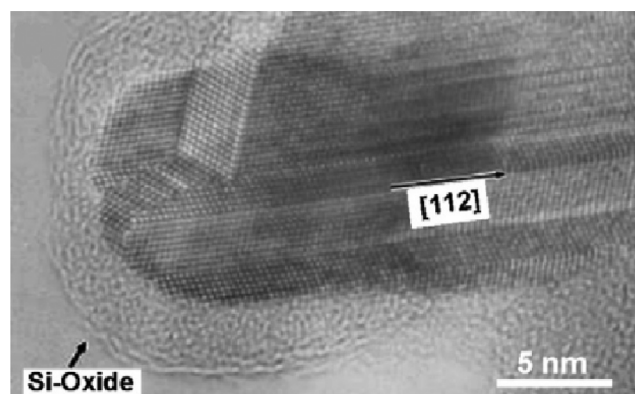


FIG. 28. OAG Si Q-Wire. Micro-twin defects are marked by the arrow. Reproduced by permission from Wang et al., Mater. Sci. Engi. R 60, 1 (2008). Copyright 2008 by Elsevier Limited.

thick oxide shell and a thin Si core, which exhibits PL at 720 nm.²⁸⁸ However, since Al is observed in the Si Q-Wire structure, it is possible that the observed PL is due to Al states.²²³ Oxide related defect states have been clearly demonstrated in the work of Ref. 297. Thus, proper control of this oxide shell is essential for the observation of QC from the crystalline Si core.²⁹⁸

Si Q-wires were produced in Ref. 83 by heating SiO powders. The wires were cleaned with HF to remove the oxide, thus forming a H-terminated surface. A clear demonstration of QC is seen in Ref. 83, Fig. 29. The energy gap was determined using scanning tunnelling spectroscopy, which also indicated doping levels in the wires as seen by an asymmetrical shift of E_G around 0 V. The formation of SiH₂ and SiH₃ was observed on the facets of the Q-wires, which leads to bending stresses in the wires.⁸³ The inherent role of O in the growth process of OAG Q-wires means we might expect their properties to be similar to those of por-Si, Secs. II A 5 a and II B 3 b. Indeed, the PL data of Ref. 83 (Fig. 29) are very similar to the work of Refs. 244 and 299 (Fig. 30).

3. por-Si

The fabrication of por-Si was described in Sec. II A 5. To make por-Si Q-Wires from QDs one needs to control the etch rate.²⁴³ Chemical and electrochemical processes were used together in the work of Ref. 250 to produce Q-Wires. Reference 250 reported a notable shift in the PL spectrum with changing porosity or Q-Wire diameter. Novel methods have been used to produce highly ordered Q-Wires arrays.³⁰⁰ More details on Q-Wire fabrication are given in Refs. 247–249.

a. Characterization of reactive ion etching nanopillars. We have been discussing fabrication of por-Si principally based on electrochemical etching. Por-Si can also be produced using reactive ion etching, which produces anisotropic etch profiles compared with electrochemical etching.³⁰¹ This method is versatile, because it can be used to make a variety of porous structures beyond Si.^{302,303} Reactive ion etching increases the etch rate by combining chemical etching with a

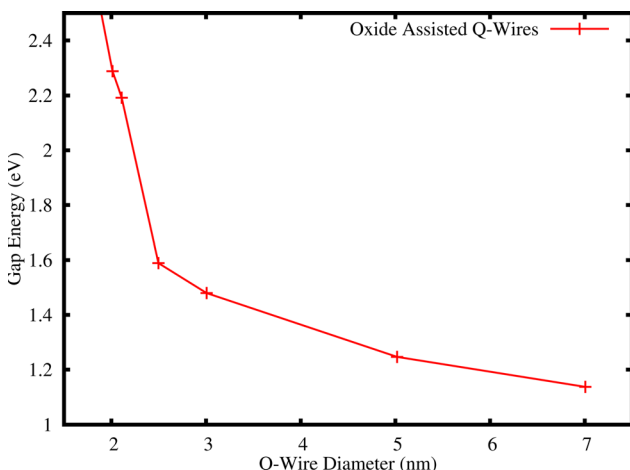


FIG. 29. Variation in the gap energy as a function of OAG Si Q-Wire diameter. Data points are taken from Ref. 83.

plasma environment. The plasma serves the same function as described in Sec. II A 2 by directing high energy particles to the substrate.^{301,304} The increased etch rate produces a large fraction of defect states.³⁰⁵

Reactive ion etching produces nanopillars. To potentially observe QC effects requires an oxidation step to thin the nanopillars, forming a structure similar to spherites. The combination of defects states from the reactive process and the oxidation process produces a highly stressed structure, where an expansion of E_G is seen in large nanopillars.³⁰⁶ In addition, defects states are seen in the PL spectrum,^{307,308} similar to the results in Secs. II A 3 and II A 2.

b. Characterization of por-Si Q-Wires. Here we discuss a few details concerning the optical properties of por-Si Q-Wires. The structural details are carried over from Sec. II A 5 a. QC effects are clearly seen in por-Si Q-Wires. A weak exchange splitting has been observed that is just enough to lift the degeneracy in the ground state between the singlet and triplet states.⁵⁷ A radiative band in the μ s range indicates an indirect structure and a fast (ns) band is observed due to interface defect states.⁵⁷

As noted in Sec. II A 5, the high fraction of dangling bonds plays an important role on the electronic states. In Ref. 309, the interface effects of the oxide vibrational modes were measured. A high H:Si ratio was found, due to the high surface to volume ratio, where the surface can additionally be passivated with O.³⁰⁹ If the surface is well passivated with H, then OH states are not significant as noted in the absorption spectrum.³⁰⁹ On the other hand, Raman measurements show an increased broadening of the Raman peak with porosity, due to stress.³¹⁰ Since oxidation reduces the Q-Wire core size until it becomes composed of spherites, the peak PL energy undergoes an increasing Stoke's shift with respect to the absorption energy as the size decreases.³¹¹

The complex array of properties that exist in por-Si Q-Wires can be seen in Fig. 30. The theoretical curves for

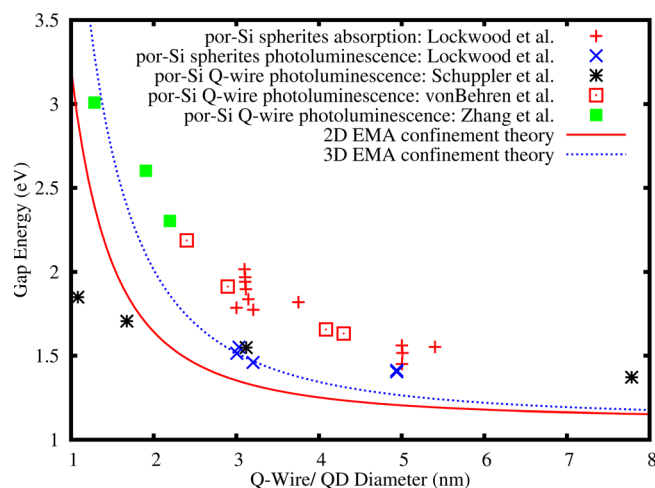


FIG. 30. Variation in the gap energy as a function of Q-Wire/QD diameter. Data points are taken from Lockwood *et al.*²⁵⁴ for spherite absorption, Lockwood and Wang²⁹⁹ for spherite PL, Schuppler *et al.*,²⁴⁴ von Behren *et al.*,³¹⁰ and Zhang and Bayliss³¹¹ EMA theoretical curves are given to guide the eye as a comparison of Q-wire (2D) versus QD (3D) confinement, from Ref. 20.

QD versus Q-Wire confinement are shown in Fig. 30 to illustrate differences due to dimensionality. In the work of Refs. 254 and 299, spherites were created. The absorption and PL data are shown in Fig. 30, where a clear Stoke's shift is noted. Reference 244 states that the structures produced were QDs and not wires. Fig. 30 demonstrates that the QD data are nearly identical to spherite PL. In addition, both Refs. 310 and 311 claim to have made Q-Wires, yet the strength of confinement in these samples is much larger than shown by spherite data, Fig. 30. This difference is an indication of increased stress due to a thick oxide layer. Finally, in terms of confinement strength, we noted in Sec. II A 2 a that amorphous materials experience stronger confinement effects. This effect is clearly seen in Ref. 312 where both a-por-Si and c-por-Si structures were fabricated, and the amorphous structures show stronger confinement effects.

C. Quantum wells

In our discussion of quantum wells here, we include superlattices (multiple layers of QWs). The QC properties of a superlattice structure are similar to those of a single QW. The PL intensity is generally larger, but there is the additional possibility of tunnelling between layers, and the interface between layers can degrade as the number of layers increases.^{313–316} For either single QWs or superlattices, stress at the interface is a common feature. The stress is due to lattice mismatching at the interface (Sec. II A 3) governed by Vergard's law.

On the whole, the fabrication methods described here tend to form amorphous layers during the initial deposition step. The layers become crystalline with a postannealing step, which can also “blur” the interface between layers.³¹⁷ Dangling bonds at the interface are the most common structural limitation for a-QWs. Defects at the interface lead to increased scattering events. Annealing a-QWs to remove these structural defects leads to greater diffusion of O at the interface compared with a c-QW.³¹⁷ However, a controlled annealing step can reduce defect concentration and results in the fabrication of a c-QW. For these reasons, one observes high variability in the results from QWs. Generally, QWs produced by sputtering and PECVD are not as reproducible as MBE and silicon-on-insulator (SOI) methods.³¹⁵

SiGe QDs were discussed in Sec. II A. The same situation of Si and Ge alloying during annealing leads to the production of SiGe QWs. Substantial work has been carried out on SiGe QWs. Some of their properties were discussed in Sec. II A. Here we list references for SiGe QWs: review article; Ref. 315, PECVD fabrication; Refs. 318–323, and MBE fabrication; Refs. 324–331.

1. Magnetron sputtering

The principles of sputtering were described in Sec. II A 1 and forming sputtered QWs follows these same general principles.^{115–117} The only difference is that instead of using reactive or co-sputtering to produce a single layer, one deposits a layer of Si preceded and followed by a barrier layer of say SiO₂. The SiO₂ layer can be created by simply oxidizing the pre-existing Si layer,³¹⁵ or by using

co-sputtering in conjunction with sputtering of pure Si.³³² It should be noted that the two methods can produce very different interfaces. In the case of co-sputtering, a sub-stoichiometric oxide is deposited, and this situation can create greater mixing at the interface after annealing.³¹⁵

Many of the essential structural characteristics of a QW formed by sputtering are identical to the QD system. However, an important difference is that QW fabrication does not require precipitation out of a sub-stoichiometric phase. Depending on the fabrication details, precipitation can occur if there is a sub-stoichiometric layer deposited. In both sputtered and PECVD wells (Sec. II C 2), QD formation is seen.¹⁵² Sputtering initially deposits an amorphous layer of Si or Ge. The amorphous structure is seen in both Raman and X-ray diffraction measurements.³³³ Fig. 31 shows that as the annealing temperature is increased the Raman peak of Si moves toward the crystalline state. Also, the increased full-width-half-maximum (compared to bulk Si) demonstrates phonon confinement, QD formation, and Si-O diffusion. Similarly, Ref. 334 reported QD formation. This indicates that the SiO₂ layer is diffusing into the Si layer producing Si QDs with a thick oxide layer.³¹³ After annealing at 1100 °C, full crystallization is observed and the Raman peaks narrows, Fig. 31.

a. Characterization of magnetron sputtered QWs. Atomic diffusion is seen in QWs because of the stress at the interface due to lattice mismatch.³³⁵ Strong diffusion at the interface indicates that defect states are important in this system, similar to our discussion in Secs. II A 5 and II A 1. Defect PL was observed at ≈600 nm, because of interfacial mixing.³³⁵ The origin of the PL band was confirmed by performing excitation wavelength and temperature dependent measurements on the PL spectrum and observing no correlation.³³⁵ Localized defect states provide a rapid decay path for excited electrons. The same 600 nm PL band was seen in the work of Ref. 332, using electroluminescence.

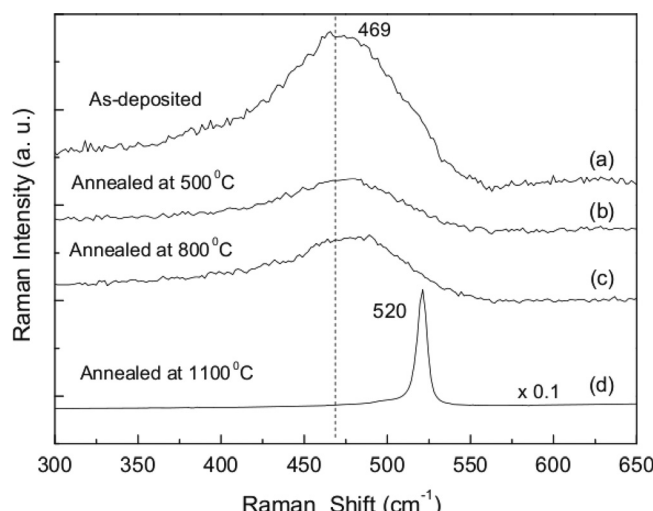


FIG. 31. Raman spectra of Si/SiO₂ superlattice annealed at the temperatures given in the figure. All annealing is performed for 30 min in a pure argon atmosphere. Reproduced by permission from Xiao *et al.*, Microelectron. Eng. 86, 2342 (2009). Copyright 2009 by Elsevier Limited.

In addition to a distinct defect PL band, there also exists a PL band at ≈ 790 nm,³¹³ Fig. 32. This red PL behaves differently than what is expected from the theory of QC since it does not move as a function of QW thickness,³³⁶ Fig. 32. In addition, the defect PL band at 600 nm does move as a function of QW thickness,^{313,333,336,337} Fig. 32. Due to the strong diffusion that happens at the interface, the 600 nm PL band was considered to arise from QC owing to holes localized in the interface layer and confined electrons.³³⁷ These results are universal to all studies in this area. Therefore, we conclude that sputtering produces a poor quality interface dense with Si dangling bonds, which leads to strong diffusion at the interface. For these reasons, it appears that the interface has a much larger impact on the pinning of hole states as compared with ion implanted QDs (Sec. II A 4a), or co-sputtered QDs (Sec. II A 1a). Therefore, high luminescence efficiencies are not likely to be achieved in sputtered QWs.

In a recent study, a significant advance was made in the fabrication of Ge QWs. In the work of Ref. 338, the authors deposited a $\text{SiO}_2/\text{Ge}/\text{SiO}_2$ QW structure using magnetron sputtering. There was no post-annealing step, and thus, the Ge QW remained amorphous. A TEM image of the Ge QW revealed that no QDs formed in the Ge layer. With no Ge-O diffusion at the interface between Ge and SiO_2 , the sub-stoichiometric oxide was reduced and thus stress was reduced, compared to Ref. 152. Furthermore, oxygen defect states were reduced by not annealing the substrate, because Ge-O bonds were reduced.²²⁴ Therefore, the blue-shift in the absorption peak measured by Cosentino *et al.* was most likely due to QC. Furthermore, the authors measured a change in E_G with reduced QW thickness (Fig. 33). The authors fitted a simple effective mass model to E_G and found the bulk gap to be 0.8 eV, which varied according to the expression: $(0.8 + 4.35/D^2)$ eV, where D is the QW thickness. Comparing this expression to the one obtained by Barbagiovanni *et al.*²⁰ ($(0.8 + 1.97/D^2)$ eV), Cosentino *et al.* found increased dispersion from the theoretical

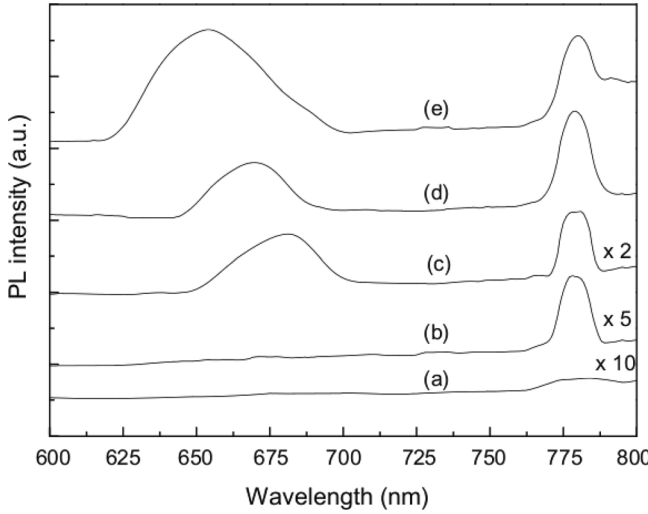


FIG. 32. PL spectra of Si/SiO_2 superlattices. Si layer thickness: (a)–(c) 4.5 nm, (d) 3 nm, and (e) 1.5 nm. (a) as-deposited, (b) annealed at 800°C , and (c)–(e) annealed at 1100°C . Reproduced by permission from Xiao *et al.*, Microelectron. Eng. **86**, 2342 (2009). Copyright 2009 by Elsevier Limited.

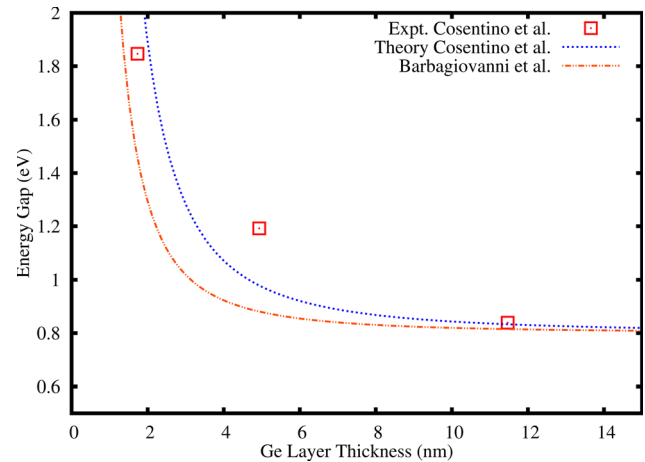


FIG. 33. Variation in the gap energy as a function of magnetron sputtered Ge QW thickness. Data points are taken from Ref. 338. Cosentino *et al.* theory curve is given by $(0.8 + 4.35/D^2)$ eV, Ref. 338. Barbagiovanni *et al.* theory curve is given by $(0.8 + 1.97/D^2)$ eV, Ref. 20.

prediction. The reason for the increased dispersion was related to a reduction of the effective mass, which was reported to be a tenth of the bulk value. This result is in agreement with the prediction of increased confinement in amorphous NSs due to a reduction of the effective mass.²⁰

2. Plasma enhanced chemical vapour deposition

PECVD fabrication is described in Sec. II A 2. As described in Sec. II C 1, to produce a QW, one simply needs to deposit a Si layer preceded and followed by an SiO_2 layer.^{155–157} PECVD is characterized by a high deposition rate (3 nm/min), and this can lead to inconsistent layer thicknesses.³¹⁵ It is also important to note that this method produces unrepeatable structures.³¹⁵ Basic CVD can also be used to produce QWs, but results in isolated islands with rough layers.³³⁹

As described in Sec. II A 2, PECVD produces amorphous layers with a high concentration of stressed (Si-O-Si) bonds, which are unstable and break at the interface forming -OH defects in the oxide layer. Raman spectra³⁴⁰ of PECVD QWs are shown in Fig. 34. The as-deposited layer shows a

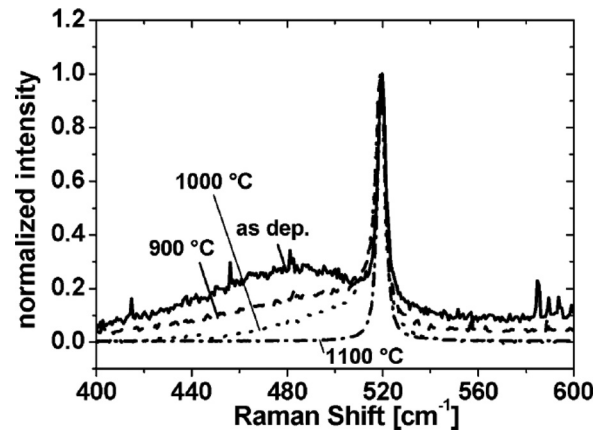


FIG. 34. Raman spectra for 10 period 4 nm thick Si QWs. Various annealing temperatures are indicated in figure. Reproduced by permission from Röller *et al.*, Microelectron. Reliab. **45**, 915 (2005). Copyright 2005 by Elsevier Limited.

strong amorphous signal. Upon annealing that signal moves toward the crystalline state peak and like sputtered QWs (Sec. II C 1), QD structures tend to form within the a-Si layer.^{340,341} Ultimately, the Raman peak is narrower than in the case of sputtered QWs, and the c-Si peak is at 510 cm^{-1} compared with the bulk value of 520 cm^{-1} , indicating stress in the system. However, the same degree of interface mixing as with sputtered QWs is not seen here.^{340,341}

a. Characterization of PECVD QWs. Stress in a PECVD QW is actually more complicated than what was described above in Sec. II C 2. Fig. 35 shows Raman spectra from Ref. 342. One can see that as the layer thickness is reduced, crystallization is also reduced. A 2 nm thick QW remains mostly amorphous with a broad Raman peak. The authors conclude that interface stress is larger for thinner layers and for a greater number of layers. In addition, this stress prevents full crystallization³⁴³ of the Si layer.^{316,342,344,345} In this work, a rapid thermal anneal was performed in forming gas, but it was also found that this method of annealing is correlated with the stress in the system.³¹⁶ Reference 316 found that the stress is tensile with SiO_2 and compressive with Al_2O_3 substrates. Thus, PECVD QWs exhibit mixing at the interface, although not as pronounced as with sputtered QWs (Sec. II C 1), due to differences in the stress levels at the interface.

From the above description, we see that there is a correlation between the interface and the quality of the QWs. IR measurements confirm that the interface is of better quality compared to sputtered QWs (Sec. II C 1a) through not observing a large concentration of Si-OH and Si-H bonds.³⁴⁶

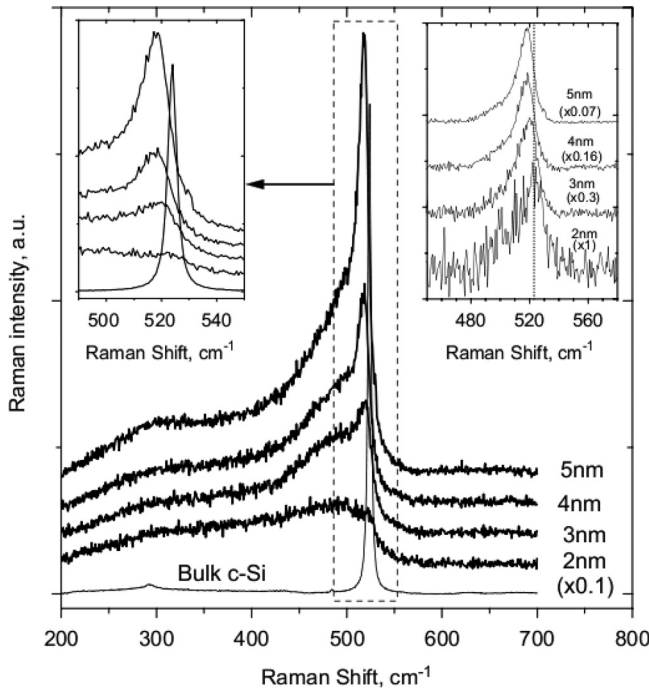


FIG. 35. Raman spectra for 10 period Si QWs. Layer thicknesses are indicated in figure. Rapid thermal annealing was performed at 1100°C . Left inset is an enlargement of the spectra indicated by the dotted box. Right inset shows the peak position after subtraction of the amorphous contribution. Reproduced by permission from Mchedlidze *et al.*, Physica E. **38**, 152 (2007). Copyright 2007 by Elsevier Limited.

The dominant interface state is $\text{Si}=\text{O}$ (Si^{2+}).³⁴⁶ Note that this comparison between sputtering and PECVD is similar for both QWs and QDs, Secs. II A 1a, II A 2a, and II C 1a.

Temperature dependent PL measurements of Si/SiO_2 superlattices do show a clear sign of exchange splitting.³⁴⁷ Furthermore, Ref. 347 deconvolutes the PL spectrum into QC and defect bands. A SiN matrix also reveals QC and defect PL,³⁴⁸ although SiN leads to more diffusion at the interface³¹⁴ as noted in Sec. II A 2a. Time-resolved PL measurements indicate a single exponential decay spectrum, due to the fact that the PECVD method tends to form isolated QDs³⁴⁹ similar to por-Si, Secs. II A 5a and II B 3b. Furthermore, the optical absorption shows a distinct shift with QW thickness.³⁵⁰ Fig. 36 demonstrates that absorption does not go to zero below E_G , which indicates absorption due to defect states along with QC states.³⁵⁰

We show many different sets of experimental data for the change in E_G as a function of QW thickness in Fig. 37. Two sets of data appear for two different annealing temperatures from the work of Ref. 342. There is a slightly higher PL energy correlated with higher annealing temperature as a result of crystallization of the QD structures and removal of defect states.^{315,342} In the second case, quartz and sapphire substrates were examined in Ref. 316. The quartz substrate shows a slightly higher PL energy, due to different stresses at the interface. The label “a/c-Si” for the data from Refs. 316 and 342 means partly crystallized. Ten period multilayers were created in Ref. 347, which shows defect PL and QC PL. The variation in results is best noted by comparing with PL from Ref. 346, where their ten period c-Si multilayer QWs show a lower PL energy as compared with Refs. 347 and 350.

The samples of Ref. 315 show the strongest confinement effects of all PECVD QW samples, and these results follow more closely with MBE results. Fig. 38 shows the results from Ref. 315 in comparison with the data described above from Fig. 37. The reason for this difference in QC is because the layers produced by Ref. 315 are a-Si:H layers. Therefore,

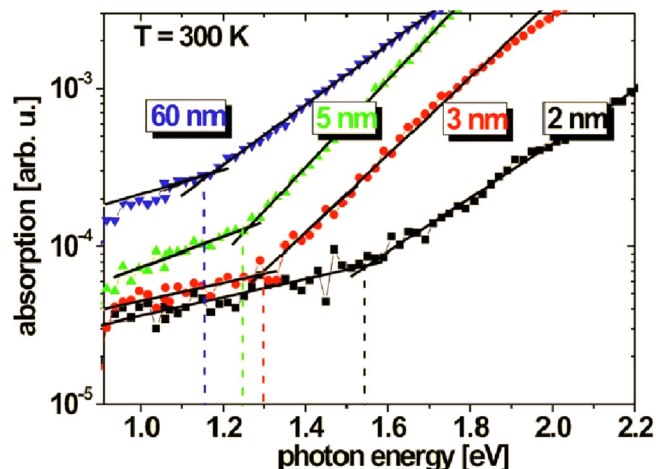


FIG. 36. Absorption spectra for Si QWs. The well thickness is indicated in the figure. The dashed line gives the gap energy for each QW size. Absorption below the gap energy is due to defect states. Reprinted with permission from Röller *et al.*, Appl. Phys. Lett. **92**, 212108 (2008). Copyright 2008 American Institute of Physics.

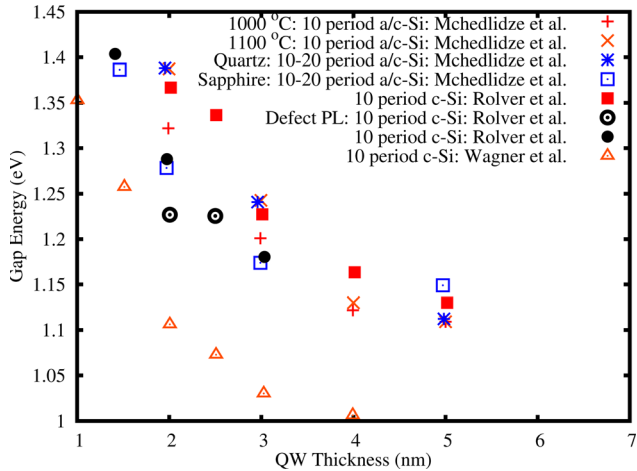


FIG. 37. Variation in the gap energy as a function of Si QW thickness. Data points are taken from Mchedlidze *et al.*³⁴² for the two different annealing temperatures, Mchedlidze *et al.*³¹⁶ for the two different substrates, Ref. 347 for ■ and the defect PL, Ref. 350 for •, and Wagner *et al.*³⁴⁶

we again see stronger confinement effects in a purely amorphous structure (Sec. II A 4 a). In addition, Ref. 315 noted that the PL moves to the red upon annealing, suggesting the important role of defects similar to the case of Refs. 313, 333, 336, and 337], described above, Sec. II C 1 a.

3. MBE

The details of fabrication are given in Sec. II A 3, where we described three growth modes: Frank-van der Merwe, Volmer-Weber, and Stranski-Krastanov.¹⁸⁰ FM growth is favoured for the production of a QW. For QW growth complete wetting of the substrate is desired.¹⁸⁰ For this to happen, one must pay attention to the surface diffusion energy with respect to the interfacial energy due to lattice mismatch. In the case of incomplete wetting, 2D formation will only be stable up to a critical thickness¹⁸⁰ and will switch to island growth based on thermodynamics. Therefore, in the face of incomplete wetting, one must supersaturate the substrate so that the 2D layer thickness is comparable to the 3D island height.¹⁸⁰

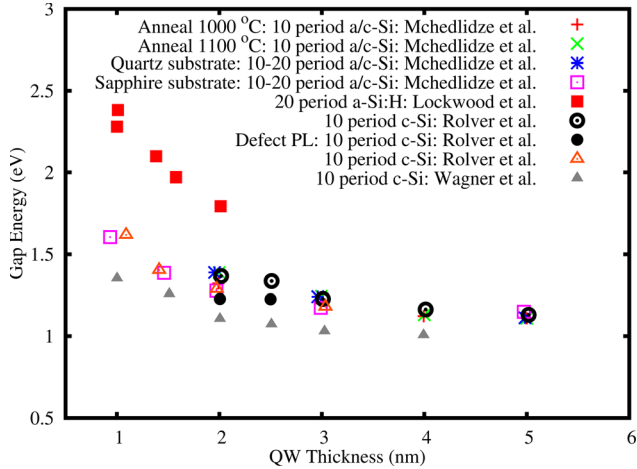


FIG. 38. Variation in the gap energy as a function of Si QW thickness. Data points are the same as in Fig. 37 with the addition of data from Lockwood.³¹⁵

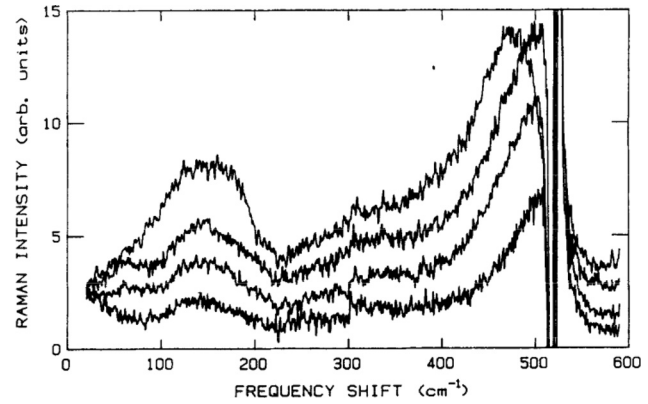


FIG. 39. Raman spectra of a Si QW for different annealing temperatures. From top to bottom: as-grown and after annealing for 30 s at 1000, 1050, and 1100 °C, respectively. The feature at 520 cm⁻¹ is an artifact from subtracting the strong Si substrate signal. Reproduced by permission from Lu *et al.*, Solid-State Electron. **40**, 197 (1996). Copyright 2006 by Elsevier Limited.

In the case of Si/SiO₂ QWs, the QWs are amorphous. The uniformity of each layer is less than the previous as monitored using RHEED.³⁵¹ In a typical set-up an a-Si layer is deposited and the SiO₂ layer is formed by exposing the sample to oxygen under controlled conditions.³⁴³ We can see the structural results from the Raman spectra in Fig. 39. The data are from Ref. 343, and there is a strong signal at 470 cm⁻¹ from the a-Si as-deposited layer, which moves toward c-Si upon annealing. X-ray diffraction shows the density of the QWs to be 97% that of c-Si.³⁴³ Therefore, some stress in the sample is relieved upon annealing, but we also see a reduction in the Si concentration. This reduction is a sign of Si incorporation into the SiO₂ layer, similar to Sec. II C 1.

a. Characterization of MBE QWs. Si/O inter-diffusion at the interface has a notable effect on the PL of MBE QWs. XPS data (Fig. 40) clearly shows that upon annealing there is a reduction in the Si⁰⁺ state and a rise in the Si³⁺ state.³⁴³ This result indicates the formation of a thick interfacial layer

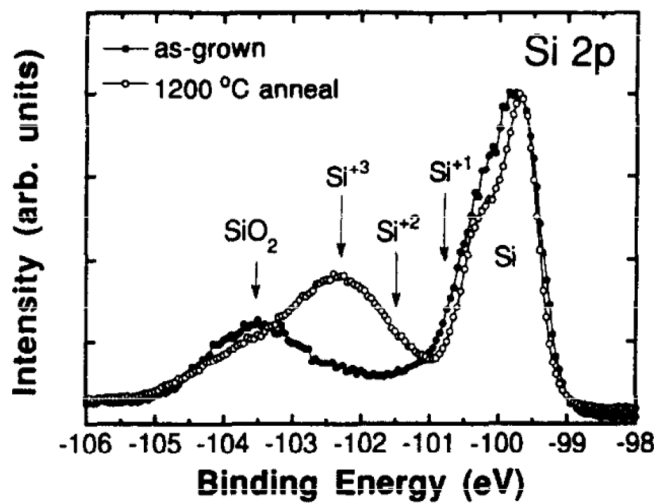


FIG. 40. Si 2p XPS spectra for a Si QW before and after annealing. Various oxide states are labelled in the figure. Reproduced by permission from Lu *et al.*, Solid-State Electron. **40**, 197 (1996). Copyright 2006 by Elsevier Limited.

(see also Sec. II C 1 a), which further means the reduction of the Si QW thickness. As a result, the as-deposited Si QW has a red PL band \approx 730 nm, Fig. 41. Upon annealing that band reduces and we see the formation of a defect band \approx 570 nm.³⁴³ Therefore, we conclude that MBE QWs are very similar structurally to sputtered QWs, Sec. II C 1 a. In both cases, we see a high energy PL band that is associated with trapped holes in defect states and QC due to confined electrons.

The variation in E_G with QW thickness is shown in Fig. 42 from results given in Refs. 352 and 353. As we mentioned, these structures are not completely crystallized and when fitting the bulk E_G the authors found the value to be 1.6 eV, which is close to that of a-Si. XPS measurements were also performed for the change in the valence band maximum (VBM) and the conduction band minimum (CBM),³⁵³ Fig. 42. A change in both the hole and electron energy is seen. This result is in agreement with structural studies of ion implanted QDs, Sec. II A 4 a. In Sec. II A 4 a, we noted that the Si^{3+} state is the dominant interface state and this causes pinning of the hole state. This pinning is not as significant as in the case of a sputtered well, Sec. II C 1 a, because the interface state is different. However, we also note that the PL energy is higher than the data from Ref. 199, Fig. 21. This observation is because these QWs are mostly disordered (not crystalline). Interfacial stress prevents complete crystallization of Si even at annealing temperatures as high as 1100 °C.^{343–345}

4. Thermal/chemical processing (SOI)

All of the fabrication methods for QWs discussed thus far produce an a-Si layer that partly or fully crystallizes with

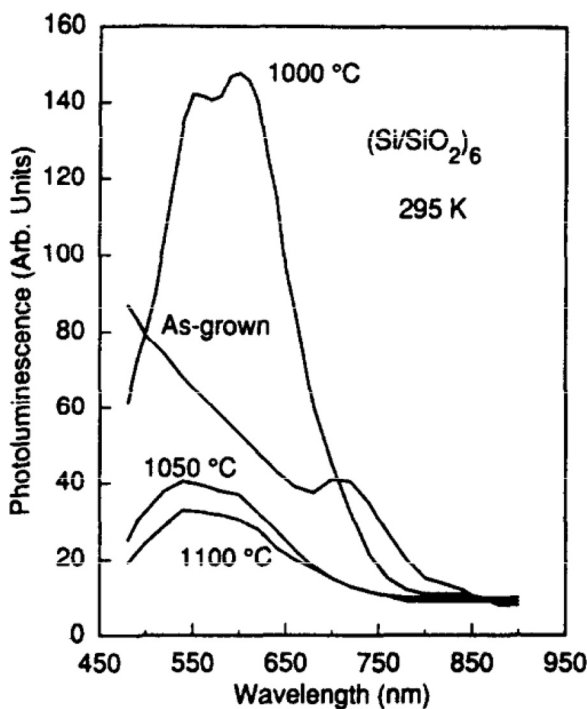


FIG. 41. PL spectra of a Si QW before and after annealing for 30 s at the temperatures indicated in the figure. Reproduced by permission from Lu et al., Solid-State Electron. 40, 197 (1996). Copyright 2006 by Elsevier Limited.

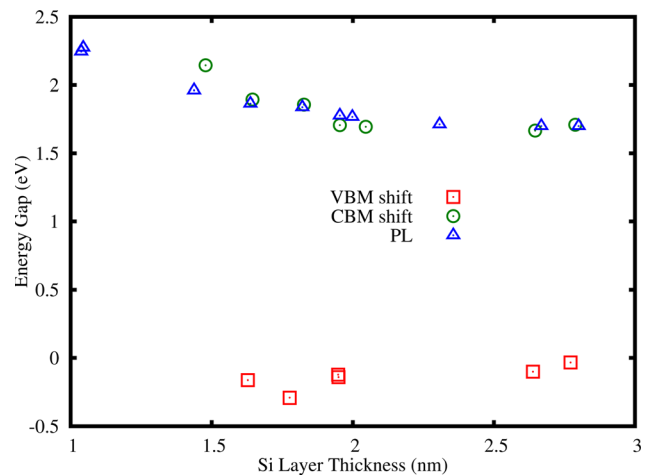


FIG. 42. Variation in the gap energy as a function of Si QW thickness. Valence band maximum, conduction band minimum, and PL data taken from Ref. 353.

thermal annealing. In addition, these methods produce QWs with a high degree of Si-O interdiffusion at the interface owing to the a-Si dangling bonds. From these perspectives, it is desirable to make c-Si QWs.

Thermal and chemical processing of silicon-on-insulator wafers produces crystalline QWs. The basic principles of fabrication are given in Ref. 198. The methodology is to produce a clean interface between a c-Si layer and an a-SiO₂ layer. SOI wafers are typically produced via the ion cut process. A clean Si substrate is implanted with H at a particular depth creating a gaseous H layer. This gaseous layer will cleave the substrate so that the upper surface can be removed. The removal of the Si layer is done by bonding it to a Si substrate with a thin SiO₂ surface layer. This forms a substrate of Si/SiO₂/Si. The separation by implantation of oxygen (SIMOX) process can also be used to form SOI substrates. SIMOX requires the implantation of high doses of O, followed by annealing. The ion cut process produces better quality interfaces than SIMOX.¹⁹⁸

The use of SIMOX along with thermal/chemical processing to produce c-Si QWs is described in Ref. 354. In this work they implant O at 200 keV and then anneal the sample for several days. This step produces a buried SiO₂ layer. The surface Si layer is then reduced by annealing in dry O to form a surface SiO₂ layer where Si-O interdiffusion thins the Si layer. A variation of SIMOX-SOI fabrication was performed in the work of Refs. 355 and 356. In this work, they produced epitaxial layer transfer SOI substrates (epi-SOI). This method produces a higher quality interface compared with SIMOX-SOI. The surface Si layer is thinned by annealing in dry O. In both cases, further thinning of the substrate happens through chemical etching. The final crystallinity of the Si-QW is verified using X-ray photoelectron diffraction.³⁵⁶

In either fabrication method thermal/chemical processing is used to thin the surface Si layer. However, in the case of Ref. 355, epi-SOI wafers have sharper (fewer sub-oxide states) interfaces comprised of different sub-oxide states compared with the SIMOX-SOI process. Variations in the interface states can be seen in Fig. 43 for two different QW

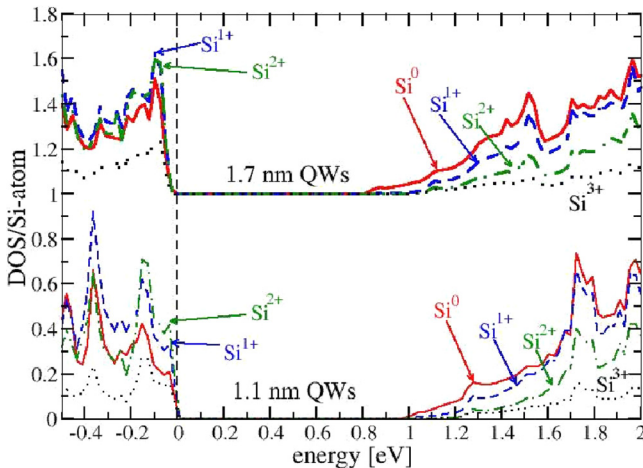


FIG. 43. Density of states calculated for Si QWs of thickness indicated in the figure. Sub-oxide states are labelled in figure. Reproduced by permission from Lockwood *et al.*, Mater. Res. Soc. Symp. Proc. **737**, F1.1.1 (2003). Copyright 2003 by Materials Research Society.

thicknesses.³⁵⁵ Recalling that fabrication requires thinning QWs with an oxidation step, Fig. 43 represents an increase of the interface thickness and thinning of c-Si. It can be seen that the Si^{1+} and Si^{2+} states dominate, while the Si^{3+} state is also increasing as the QW thins.³⁵⁵

a. Characterization of SOI QWs. Differences due to interface and defect states between different fabrication methods can be clearly seen in the PL spectrum. In the case of epi-SOI,^{355,356} there is a consistent PL peak at 1.8 eV, Fig. 44. The PL spectrum was deconvoluted to reveal a peak fixed at 1.8 eV and another PL peak due to QC. The shift in the VBM and CBM position was measured in the work of Ref. 356, Fig. 44. In addition, Fig. 44 reports the combination of the VBM position and the CBM position, which represents the change in E_G as would be seen in absorption measurements. PL measurements are reported in Ref. 355, Fig. 44. It is clear that the QC PL is Stoke shifted from the absorption data (CBM+VBM). This result indicates pinning

due to interface states. These results are similar to Secs. II A 1 a and II A 5 a.

Comparing epi-SOI results with data from SIMOX-SOI c-QWs, there is a distinct difference in the PL data,^{354,357,358} Fig. 44. We noted that SIMOX-SOI produces a blurred interface, therefore, a stronger effect from the interface is observed. In the work of Ref. 354, they also found a defect (1.65 eV) and QC PL band. Fig. 44 shows the data from Ref. 354, where one can see that the PL data are red-shifted from the epi-SOI data and lie closer to the SIMOX-SOI defect PL. Deep defect centres are formed in these samples. Annealing shows an initial PL at 1.5 eV that transforms into a PL band at 1.8 eV.³⁵⁴ This result indicates a strong pinning due to interface states, similar to our discussion in Secs. II C 1 a and II C 2.

III. NANOSTRUCTURE PARAMETERS

The primary objective of this section is to provide an overview of the salient features of Si and Ge nanostructures revealed by our general discussion in Sec. II. We emphasize the relevance of each structural parameter discussed in Sec. II for each fabrication method on the observed experimental results. It is clear that there are general properties applicable to any Si or Ge NS. All NSs show a clear distinction between defect related photoluminescence and quantum confinement related PL, Sec. II. Defect states potentially couple with confined carriers, effectively lowering the observed confinement energy. Although, if the PL is strictly related to defects, the emitted wavelength will not change as a function of NS size, while QC PL is size-dependent. O defect states are particularly a problem in the case of Ge NSs due to Ge diffusion and GeO desorption.²²⁵

There is a high probability that dangling bond, P_b , defects will form at the interface between the NS and matrix material, which can be passivated with H by using a forming gas anneal. P_b defects, which are broken sp^3 bonds ($\mathcal{O}(0.2$ to 0.3 eV)), have an interfacial energy of ≈ 0.6 eV and can become hole trap states.^{7,359,360} In many structures, it is energetically favourable for Si-O-Si (Si^{1+} state) to form at the interface during annealing.³⁶¹ However, prolonged annealing increases the interface thickness by consuming Si, increasing tensile stress and breaking Si-O-Si bonds, thus forming $\text{Si}=O$ (Si^{2+} state), which is a deep defect state. $\text{Si}=O$ captures electron carriers in the p-state of Si and holes are trapped in the p-state of O. While, Si-O-Si and Si-OH are not deep level defects they do cause pinning of the hole. The Si^{3+} state was reported for a few structures (Secs. II A and II C) and was noted to relieve stress in the system.

Differences in NS fabrication create variations in the observed interface states, along with the thickness of the interface. Universally, we noted that a thick interface increases the stress observed in the NS and modifies the gap energy, E_G . Stress also results from lattice mismatch at the interface. In the case of sub-oxide states at the interface, the confinement energy is lowered.^{142,359} Lowered confinement energy implies increased carrier diffusion and scattering at the interface, thus modifying the boundary condition and potentially the effective mass.³⁶² The question of how the

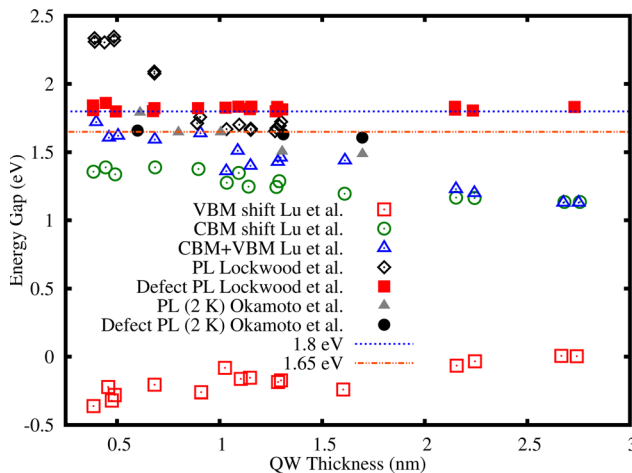


FIG. 44. Variation in the gap energy as a function of Si QW thickness. Valence band maximum, conduction band minimum, and VBM+CBM data taken from Ref. 356. PL and defect PL from Ref. 355. PL and defect PL at 2 K from Ref. 354. Defect PL is indicated by the lines at 1.8 and 1.65 eV.

effective mass changes according the dimension and the boundary conditions of a NS is complicated and does not have a clear solution at the moment.^{20,363} While the search for proper treatments of boundary conditions finds novel solutions in theoretical models,³⁶⁴ see also Sec. IV.

Another general difference in NS properties arises from the degree of crystallinity of the structure. Amorphous NSs exhibit stronger effects, as clearly seen in measurements for the confinement energy²⁰ and lifetime.³⁶⁵ Structural differences affect pinning of the hole state at the interface. It was noted (Sec. II) that certain systems exhibit a Stoke's shift between the emission and absorption spectrum due to bridging bond vibrational modes at the interface, which couple to the hole state. In addition, a modification in the confinement strength comes about from a change in the effective mass between the crystalline and amorphous structure. Carriers in an amorphous structure have a lower effective mass compared with their crystalline counterpart.^{20,366}

The precise details of how these features manifest depends on the fabrication method. In particular, how the concentration of Si³⁺ states will vary at the interface, the magnitude of stress, or dielectric effects from the matrix material will all vary depending on the fabrication method. Relevant energy scales such as the fine structure, and Coulomb energy (Sec. I) can be accurately considered in a theoretical model of NSs and dealt with on an individual basis according to the fabrication technique. The principle parameters identified are the stress, interface states and thickness, crystal structure, defect states, boundary conditions, effective mass, and dielectric matrix effects. Many of these parameters are interconnected and manifest with varying magnitude. In our discussion below, we have classified the main features of each fabrication method according to their interface states, stress, and defect states. The label “defect states” is intended to refer to defects in the oxide matrix or impurity type defects. It is important to note that these are broad classifications. In many cases, there is not enough information available to completely classify the effect a parameter has on the NS. For example, information about how the interface states modify the local charge environment allows one to model interface dielectric effects.

A. QD parameters

QDs have a large surface to volume ratio, which leads to an enhancement of the spatial confinement effect.³⁶⁷ Spatial confinement can be clearly distinguished from QC. Nonetheless, the increase in the surface to volume ratio means that there is a stronger influence on the QC PL from interface states in a QD as compared with other NSs. On the other hand, as mentioned in Sec. IA2, the selection rules are more strongly broken in a QD structure.

1. Co-sputtering

Co-sputtering produces SiO_x or GeO_x films and exhibits large variability in film stoichiometry based on the experimental parameters. Sub-stoichiometric films are thermodynamically unstable and thus form QDs upon annealing. Co-sputtered QDs are crystalline.

a. Interface states. Deposited films typically exhibit all sub-oxide states. Magnetron co-sputtering primarily exhibits the Si¹⁺ state at the interface upon annealing.³⁸ Reactive magnetron sputtering produces a relatively equal contribution from all three sub-oxide states.¹³³ This method of fabrication does yield variability in the final structure. Such variations in the interface state are observed in the PL spectrum.^{134,140}

b. Stress. Reactive sputtering produces a thick interface, which implies increased stress in the QD and causes the observed change in E_G.¹⁴³ Raman measurements confirm confinement effects and stress in QDs.^{132,144} Magnetron co-sputtered Ge QDs also experience high levels of stress.¹⁵² Stress in Ge QDs potentially changes the band gap structure to direct.^{131,150,151}

c. Defect states. O defect state are dominant in Ge QDs,¹³¹ whereby E' defect PL is observed.¹⁵³ However, if the O states are controlled properly in Ge samples, then QC PL is detected in the red to near-infrared range.¹³⁵

2. PECVD

Like co-sputtered QDs (Sec. III A 1), PECVD deposits a sub-stoichiometric film that is annealed to form QDs. MPD and laser pyrolysis have similar properties with PECVD since they are also based on the decomposition of silane gas. PECVD QDs are commonly amorphous in a nitride matrix and crystalline in an oxide matrix. Surface structures are crystalline or polycrystalline.^{173–175}

a. Interface states. PECVD produces a low concentration of Si-Si bonds. The interface is comprised of roughly an equal contribution of Si³⁺ and Si¹⁺ states.³⁸ The Si₃N₄ matrix exhibits finite confinement due to a graded interface structure.^{169–171}

b. Stress. PECVD QDs form a thick interface.³⁸ Raman measurements often indicate significant stress.¹⁶⁸ Surface structures exhibit a strong blue-shift in the PL energy due to lattice mismatch.¹⁶⁷ Si₃N₄ embedded QDs are typically under large stress.¹⁷⁰

c. Defect states. Surface structures suffer from defects at the interface due to mixing.¹⁶⁶ The PECVD deposition process produces Si-O-Si with a low bond angle.^{156,164} Si-O-Si bonds break and defect centres form, which include Si-H, Si-N, Si-OH, and N-H bonds.^{155,164} Nitrogen contamination comes from the use of N₂O. Initially, Si-N is observed and annealing produces Si-O-N.¹⁶⁴ Nitrogen contamination blue-shifts E_G and lowers the absorption efficiency.³⁸ A Stoke's shift between absorption and emission is observed.¹⁶⁸

3. MBE

MBE QDs are surface grown structures similar to CVD or evaporation based methods. QD island forms due to strain at the interface and can be capped with another material.

MBE QDs are crystalline structures. Several novel substrates have been used for the production of MBE QDs.^{185–191} LaAlO₃ substrates exhibit strain at the interface.^{189,190} Gd₂O₃ substrates create a large change in the conduction band energy.^{187,188}

a. Interface states. The interface of an as-deposited film and/or island is sharp. If the temperature during deposition is too high, diffusion at the interface may occur leading to a general “blurring” or grading of the interface. MBE growth is highly reproducible, although contamination can be a problem.¹⁸⁰

b. Stress. Ge grown on Si tends to form an alloy, Si_{1-x}Ge_x, and the Raman spectrum shows signs of strain.¹⁹² Ge grown on SiO₂ shows signs of stress at the interface.^{193,195}

c. Defect states. Ge QD formation on a Si(001) substrate exhibits a combination of strain induced formation at the interface and strain relaxation through dislocations.^{181,183} If O is introduced or if O diffusion at the interface occurs, then O defect states are also observed.¹⁹² Ge QDs on SiO₂ or TiO₂ exhibit a wide PL band associated with defect states along with a QC PL band.^{193,194,196}

4. Ion implantation

QDs formed by the ion implantation method show wide variability in their final optical properties, owing to the existence of a wide range of experimental parameters one can choose for the formation of QDs. Ion implantation produces a super-saturation of Si or Ge in a substrate material. Subsequent annealing creates nucleation sites for the formation of QDs. Defect generation during the fabrication process is essential for the production of QDs.^{199,201} The final QD structure is crystalline.

a. Interface states. P_b defects at the interface can be passivated with forming gas to increase the PL intensity.^{215,221} Typically, the interface is comprised of the Si³⁺ state.^{5,212} The interface is sharp for moderate implantation conditions but does vary with implantation energy and dose.^{5,212} In addition, the Si¹⁺ state is found at the interface.²¹⁹ High energy interface states and low energy QC states are observed.^{43,230}

b. Stress. QDs produced under high energy and high dose conditions²¹⁹ or with multiple implant energies²²⁷ have a thick interface leading to increased stress in the system. For moderate implantation conditions stress is relieved due to interface relaxation via the Si³⁺ state.⁵ Ge QDs are highly stressed due to the nature of the interface.^{234–236}

c. Defect states. Defects formed during the implantation process include oxygen vacancy defects, V_O, E' centres, and non bridging oxygen hole centres (NBOHC).^{215,216} Defects are almost completely removed during annealing.^{204,215,219} In the case of Ge, one observes significant out-diffusion of Ge and stress.^{224,225,231–234,237–241} Ge oxidizes during the

annealing process, GeO species desorb from the substrate, and O defect PL is observed.

5. Por-Si

Por-Si features are determined largely by the etch rate. Short etches with a high etch rate produces QDs, or spherites. The etching process creates a large surface area full of dangling bonds and a complicated surface chemistry is produced.²⁴³ Large structural inhomogeneity is also observed. Either crystalline or amorphous Si can be produced by etching.

a. Interface and defect states. The porosity of por-Si QDs varies with QD size, thus the interface structure also changes. Large QDs have a well-defined interface, while small QDs exhibit predominantly the Si²⁺ interface state.²⁵² Vibrational modes at the interface create a Stoke's shift between the absorption and emission spectrum.^{56,75,254} Clear defect related PL is observed in highly oxidized samples.^{259,260}

b. Stress. Large tensile stresses are observed on the surface with a compressive component at the interface.²⁵⁵ Raman spectra indicate significant stress in por-Si.^{256–258}

B. Q-Wire parameters

Q-Wire systems reported to date do not, in general, exhibit strong confinement effects due to the large concentration of defects that are produced. Traditionally, diameter control down to the Bohr radius has been a problem. Q-Wire diameter is dependent in large part on the crystallographic orientation of the substrate.

1. VLS

VLS Q-Wires produce anisotropic arrays, are crystalline, and of uniform diameter.^{271,272}

a. Interface and defect states. Metallic state contamination is inherent to the growth method and introduces deep level defects in Si and Ge.^{19,279} The growth axis and temperature during formation determine the type of observed defects.^{266,278} Oxide interface states depend on the annealing conditions, which transform the Q-Wire into NS spheroids.²⁶⁶ Strong defect related PL is observed due to oxidation.^{276,282,283} Ge Q-Wires react with the native oxide and form a GeO_x sheath leading to defect PL.^{269,279–281}

b. Stress. Oxide annealing is used to reduce the diameter of the VLS Q-Wires, which increases the observed stress.²⁸⁰

2. OAG

Diameter control is obtained by increasing the oxidation step, yielding a thin Si core.²⁸⁸ The strong dependence on the oxidation process for the production Q-Wires means that only defect PL will be observed for Ge structures.^{290–292} Crystalline structures typically are produced.

a. Interface and defect states. Micro-twin and dislocation defects are observed.^{19,266,289,292} OAG Q-Wires have a SiO

sheath terminated by SiO_2 .²⁹⁴ Oxide defect PL is observed,^{292,297,298} in addition to Al defect PL when zeolite is used.²²³

b. Stress. Sub-oxide states can be modified to the SiO_2 state by additional annealing in oxygen, but this also increases the observed stress.^{83,287,292} HF etching leads to H termination and the formation of SiH_2 and SiH_3 states, which creates bending stresses in the wires.⁸³

3. Por-Si

Por-Si wire fabrication is characterized by a longer etch with a slow etch rate through the use of both chemical and electrochemical processes.^{243,250} Reactive ion etching (RIE) incorporates a plasma environment for an increased etch rate producing anisotropic etch profiles.³⁰¹ RIE can be used to make a variety of Q-Wire structures beyond Si.^{302,303}

The structural properties of por-Si wires are identical to their QD or spherite counter part. Spherites were created in the work of Refs. 254 and 299, QDs in Ref. 244, which exhibits a PL spectrum similar to spherites, and Q-Wires were produced in Refs. 310 and 311. Both amorphous and crystalline structures were studied in Ref. 312.

a. Interface and defect states. Reactive ion etching has a high etch rate producing a large fraction of defect states.³⁰⁵ Oxidation is used to reduce the diameter, implying the introduction of stress and defect states.^{306–308}

C. QW parameters

Apart from the case of SOI QWs, as deposited QWs tend to be amorphous with a large fraction of dangling bonds at the QW layer interfaces. Strain at the interface is a common feature in QWs. Annealing can relieve the strain, but this leads to increased diffusion at the interface.³¹⁷ Increased imperfections are seen with subsequent layer formation in the case of multilayer superlattices.

1. Magnetron sputtering

Magnetron sputtered wells have very similar properties to co-sputtered QDs, Sec. IIIA 1. Sputtering initially deposits an amorphous layer of Si or Ge, which becomes crystalline upon annealing.³³³

a. Interface and defect states. In the case of sub-stoichiometric layer deposition, QDs are found in the sample after annealing.³³⁴ Diffusion at the interface leads to deep level defect states coupled with hole carriers.^{313,332,333,335–337}

If the annealing step is neglected, the QW will remain amorphous, and diffusion at the interface is alleviated thus QDs will not be observed.³³⁸ This procedure produces QWs with strong confinement effects.

2. PECVD

The properties of PECVD QWs are similar to their QD counterpart, Sec. IIIA 2. Experimental results are

inconsistent between experimental set-ups. QDs structures tend to form in the a-Si layer.^{340,341}

a. Interface and defect states. Si-O-Si bonds are unstable and break, forming defect centres. The dominant interface state is $\text{Si}=\text{O}$.³⁴⁶ Distinct QC and defect PL is observed.^{347,348} QC PL is mainly due to the formation of QD structures.^{315,316,342,346,350} The work of Ref. 315 produces clear QC PL, because the structures remained amorphous.

b. Stress. Raman measurements do indicate high stress levels in the QWs. However, stress is ultimately determined by the experimental set-up depending on whether the QW fully crystallizes or not.^{316,342}

3. MBE

The properties of MBE QWs are similar to MBE QDs, Sec. IIIA 3. The crystalline structure of MBE QWs is disordered, i.e., not completely amorphous.³⁴³

a. Interface and defect states. Diffusion occurs at the interface.³⁴³ XPS measurements report the Si^{3+} state concentration at roughly half the Si-Si concentration, thus forming a relatively thick interface.^{343,352,353}

4. SOI

SOI QWs are crystalline. Samples are produced either using a SIMOX-SOI,³⁵⁴ or an epitaxial layer transfer of SOI (epi-SOI)^{355,356} fabrication method.

a. Interface and defect states. Si^{1+} and Si^{2+} states are observed in epi-SOI QWs, which have a sharper interface than SIMOX-SOI QWs.^{355,356} epi-SOI exhibits QC and defect PL and there is a Stoke's shift between the absorption and emission.^{355,356} SIMOX-SOI QWs reveal deep level defect PL.^{354,357,358}

IV. THEORETICAL MODELLING

In this section, we review commonly used theories for modelling nanostructures. We will highlight salient features of each theoretical model and how they pertain to the experimental observations. Before doing this, it is worth mentioning some features of the most common experimental methods used to measure the variation of the gap energy, E_G .

Photoluminescence is the process of absorbing electromagnetic radiation and re-emitting this radiation at the same or different energy.⁵⁵ Many of the details concerning how a material absorbs this radiation are given in Sec. I (in particular, see Sec. IA 2). Here we discuss the qualitative features of a PL spectrum.

PL is a widely used experimental method in NS studies, because it directly measures the effects of quantum confinement. When a photon of energy $\hbar\omega$ is absorbed by a material, an electron, e , given sufficient energy, is excited into the conduction band from the valence band, thus creating a hole, h , in the VB. As discussed in Sec. IA 1, this process, in principle, requires a phonon of energy $\hbar\Omega$ for momentum

conservation in an indirect gap material, see Fig. 45. If the excitation energy is higher than E_G , the electron will relax ($\mathcal{O}(10^{-13} \text{ s})$) to the conduction band minimum, before finally returning to the ground state, or the valence band maximum. During the final relaxation step, the emitted photon energy, $\hbar\omega'$, is characteristic of the energy gap ($\hbar\omega' = E_{\text{CBM}} - E_{\text{VBM}} = E_G$). Therefore, a blue-shift in $\hbar\omega'$ from the bulk value of the band gap is evidence of QC. However, the picture can become complicated by defect or interface states that might exist in the mid-gap region, as discussed throughout Sec. II.

The intensity of the PL spectrum, I_{PL} , is characteristic of the number of carriers involved in the PL process. For a carrier concentration, $n(E) = f(E)\rho(E)$, where $f(E)$ is the Fermi-Dirac distribution and $\rho(E)$ is the density of states (DOS) (Eq. (2)), $I_{PL} \sim \int n(E)\delta(\hbar\omega - E)dE$. $\delta(\hbar\omega - E)$ maintains energy conservation and for the situation described here $E \rightarrow E_G$. In the case of a quantum dot, the DOS is a δ -function; thus, the PL spectrum should become a single vertical line for transition across the band gap. Single transitions are never observed primarily due to inhomogeneous broadening (Sec. IA 2); thus; the actual PL spectrum represents a distribution of QD sizes.

It is important to note that this distribution of QD sizes can create inherent complications while analysing the experimental data with QC models. The problem is in accurately associating a single QD diameter with the correct PL energy, E_{PL} . The convention is to assume that E_{PL} measured at the peak of the PL is associated with the peak in a measured NC size distribution (often measured using high-resolution transmission electron microscopy (HRTEM)) and these two numbers are checked against the theoretical model. Generally, one can check that the distribution of sizes and energies agree, and thus, the convention is justified.³³⁵ However, it is also possible that interactions between QDs can shift the

peak energies.^{141,163} The exact effect of this shift is difficult to determine at present. Nonetheless, if we consider a simple model of QC⁵ to compare with the PL spectrum from single QDs of porous Si (Fig. 2 of Ref. 253), there is good agreement with the porous Si QDs of Refs. 243 and 299. Therefore, one can be reasonably confident in this convention.

Other methods used to measure E_G include absorption spectroscopy,³⁰ PL excitation spectroscopy,²¹⁹ scanning tunnelling spectroscopy,⁸³ or X-ray absorption methods (X-ray photoemission spectroscopy or X-ray absorption near band edge) combined with ultra-violet spectroscopy.³⁵² The principle behind each of these methods is similar to PL and so our discussion also applies to each of these methods. Note that the above stated methods are size selective, and so one obtains better error bars in the measurement.

A final important feature in theoretical modelling concerns the exact magnitude of the NS properties stated in Secs. II and III. Throughout this manuscript, we emphasized how certain effects such as stress placed on a NS as a function of the interface thickness modify E_G , or the effect of the Si-O-Si vibrational mode at the interface. The complication is in accurately modelling each parameter for the different types of NSs. The effect of surface and interface states is more important in the case of QDs, than in the case of quantum wells. This fact can be seen in VB measurements. In Sec. IIC 1a, pinning due to the Si^{1+} state at the interface on the VB level was noted. In Sec. IIC 3a, however, this same interface state was found, and VB measurements do show a slight shift in the energy, Fig. 41. The difference between these results is thus due to the different surface to volume ratio between a QD and a QW. Therefore, to properly model NSs it is not sufficient to know only what parameters exist in that system, one must also know how the parameter manifests itself according to the dimensionality of the NS.

A. Overview of theoretical methods

Electronic (band) structure calculations are well understood for bulk materials. The many-body Hamiltonian describing the interactions between the electrons and ions in the material is approximated by a single electron Hamiltonian.⁴⁰ This Hamiltonian contains an effective crystal potential with the periodicity of the lattice

$$\left[-\frac{\hbar^2}{2m_o} \nabla^2 + V_c(\mathbf{r}) \right] \Psi(\mathbf{r}) = \mathcal{E} \Psi(\mathbf{r}), \quad (16)$$

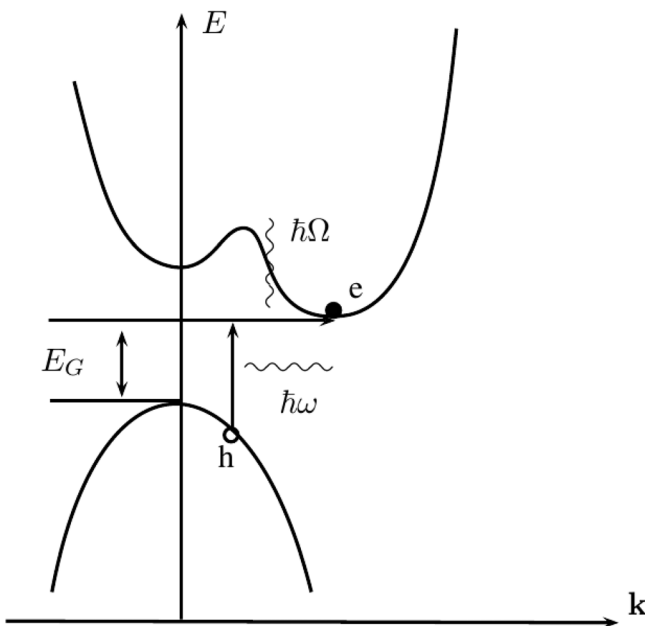


FIG. 45. Schematic of an electron, e , hole, h , transition in an indirect semiconductor via the aid of a phonon, $\hbar\Omega$, and a photon, $\hbar\omega$.

where m_o is the free or bare electron mass, $V_c(\mathbf{r})$ is the crystal potential, and $\Psi(\mathbf{r})$ is a product of the free electron function and the Bloch function. Bloch's theorem describes the long range periodic order of a crystal and gives solutions to the effective single electron Hamiltonian (Eq. (16)) yielding electronic band states.³⁶⁸ Further approximations to the calculation depend on the details of the particular theory: EMA with the $\mathbf{k} \cdot \mathbf{p}$ generalization (Sec. IV B), empirical tight-binding (ETB, Sec. IV C), or empirical pseudopotential method (EPM, Sec. IV D).

In general, the form of the crystal potential is complicated. However, the properties of an electron in a crystal potential may be simplified with the use of the EMA.^{8,369} The EMA is a first order approximation within the envelope function approximation (EFA), which is well-suited to describe electron and hole states.^{74,370,371} Physically, one can understand the EMA by taking the time derivative of the group velocity and relating it to the net force on an electron in a periodic potential. Thereby, the effect of the potential at each lattice site is averaged out, yielding

$$\frac{1}{m^*} = \frac{1}{\hbar^2} \frac{\partial^2 E}{\partial \mathbf{k}^2}, \quad (17)$$

where m^* is called the effective mass and E can be assumed to be the free electron energy. Since m^* contains the effect of the crystal potential, in Eq. (16) $m_o \rightarrow m^*$ and $V_c(\mathbf{r})$ is dropped from the expression. The effective mass can be used in all theories for band structure calculations as a first approximation.^{7,372,373} In the tight-binding model, the effective mass is related to the hopping parameter and carrier mobility.³⁷⁴ However, since this parameter depends on periodic symmetry, it may be hard to justify in a NS.^{5,20} Accurate theoretical modelling of the electronic structure for NSs faces many challenges. The first and most obvious problem is the lack of long-range periodicity. Still, a NS is generally ‘many’ times larger than the lattice spacing, and thus Bloch’s theorem is still applicable, while not rigorously justified. This issue is particularly difficult to justify in the case of the EMA, but there are corrections that can be made.^{18,375,376} The EMA has been justified down to 100 atoms.³⁷⁷

For an amorphous material, in the absence of long range order, there is still well defined short-range order, which is utilized by invoking spatially dependent parameters.³⁷⁸ A reduction of long range order means poorly defined momentum vectors and thus momentum selection rules are relaxed for optical transitions. Recalling from Sec. IA 2, breaking of the selection rules results in an increase of the oscillator strength. Modelling the electronic structure in the amorphous material either uses cluster sets according to existing short range order, or super-cells are amorphized and repeated.³⁷⁹ Many of the properties of amorphous Si and Ge are similar to their crystalline counterparts provided that the dangling bonds are passivated with H.^{380,381} However, an important difference is that the amorphous material exhibits localized band tail states in the mobility gap due to defects (or disorder), in contrast to a crystalline system. It is around the mobility edge that one defines the effective mass in the amorphous material.³⁶⁶

An overview of the theoretical models along with various results for Si and Ge NSs is given in the remainder of this section. More detailed information is provided in the references given below for bulk and NS calculations. The main focus is on how to calculate the effect of QC on the oscillator strength and E_G , Secs. IA 1 and IA 2. Each theoretical model ($\mathbf{k} \cdot \mathbf{p}$, ETB, EPM) provides different insights into the essential physics of the system. Nonetheless, all theories are empirical, and therefore, caution must be exercised to ensure all of the experimental parameters are being properly

considered. It should further be noted that many variations and alternative theories exist, with varying degrees of success. Still, these alternatives are derived from the same basic assumptions of band structure calculations.^{382–386}

B. Effective mass approximation, $\mathbf{k} \cdot \mathbf{p}$ method

A good introduction to the method is given in Ref. 40. A full detailed treatment is given in Ref. 387. Reference 370 describes symmetry considerations within the method and how to include perturbations such as strain. Reference 369 is concerned with the wave-mechanics of the method for heterostructures. References 7 and 74 provide applications of the method within a low-dimensional system.

1. $\mathbf{k} \cdot \mathbf{p}$ method applied for bulk phase

The $\mathbf{k} \cdot \mathbf{p}$ method is a perturbation based calculation where the band structure over the entire Brillouin zone is extrapolated from the zone centre. One solves Eq. (16) by using the basis set $\Psi(\mathbf{r}) \rightarrow \Psi_{n\mathbf{k}}(\mathbf{r}) = \exp(i\mathbf{k} \cdot \mathbf{r}) u_{n\mathbf{k}}(\mathbf{r})$ in the reduced zone scheme, such that Eq. (16) becomes

$$\left[\frac{\mathbf{p}^2}{2m_o} + \frac{\hbar \mathbf{k} \cdot \mathbf{p}}{m_o} + \frac{\hbar^2 \mathbf{k}^2}{2m_o} + V_c(\mathbf{r}) \right] u_{n\mathbf{k}}(\mathbf{r}) = E_{n\mathbf{k}} u_{n\mathbf{k}}(\mathbf{r}), \quad (18)$$

where \mathbf{p} is the momentum operator, there is a sum over the wavevector, \mathbf{k} , and $E_{n\mathbf{k}}$ is the energy of the n^{th} band. Equation (18) is greatly simplified in the case of $\mathbf{k}=0$, where E_{n0} is fitted from experiment and u_{n0} is assumed to be given by the corresponding atomic orbital.

The $\mathbf{k} \cdot \mathbf{p}$ term in Eq. (18) is treated as a perturbation, so that energy solutions around all points in the Brillouin zone, up to second order, are given by

$$E_{n\mathbf{k}} = E_{n0} + \frac{\hbar^2 \mathbf{k}^2}{2m_o} + \frac{\hbar^2}{m_o^2} \sum_{n' \neq n} \frac{|\langle u_{n0} | \mathbf{k} \cdot \mathbf{p} | u_{n'0} \rangle|^2}{E_{n0} - E_{n'0}}. \quad (19)$$

What is left to be determined for the band structure is the matrix elements, $\langle u_{n0} | \mathbf{k} \cdot \mathbf{p} | u_{n'0} \rangle$. These terms are simplified using symmetry arguments and found by fitting to experiment.³⁶⁸ A more accurate treatment includes such effects as degenerate bands, multi-bands (Kane model), hole states, and spin-orbit coupling for hole states (Luttinger Hamiltonian).^{28,387}

The band energy can be expressed as $E_{n\mathbf{k}} = E_{n0} + \frac{\hbar^2 \mathbf{k}^2}{2m^*}$ for small values of \mathbf{k} . Comparing with Eq. (19) gives an expression for m^*

$$\frac{1}{m^*} = \frac{1}{m_o} + \frac{2}{m_o^2 \mathbf{k}^2} \sum_{n' \neq n} \frac{|\langle u_{n0} | \mathbf{k} \cdot \mathbf{p} | u_{n'0} \rangle|^2}{E_{n0} - E_{n'0}}. \quad (20)$$

For this reason, the EMA is the lowest order case of the general $\mathbf{k} \cdot \mathbf{p}$ theory. Since the $\mathbf{k} \cdot \mathbf{p}$ method is a perturbation based theory, it is very easy to include extra terms, such as hydrogenic impurities, strain, defects, and interface states.^{7,370,372} The $\mathbf{k} \cdot \mathbf{p}$ method is versatile in its ability to describe the symmetry of the system,³⁷² the physical

relevance of results,³⁸⁸ and the effect of external fields,³⁸⁹ to name a few.

2. $\mathbf{k} \cdot \mathbf{p}$ theory for nanostructures

Generally, the EMA is used to describe the CBM while the $\mathbf{k} \cdot \mathbf{p}$ method is used for the VBM.³⁷³ Application of the method is based on the EFA.³⁹⁰ In this approximation, one considers a perturbing potential that does not vary significantly over the lattice constant, such that Eq. (16) becomes,

$$\left[-\frac{\hbar^2}{2m_0} \nabla^2 + V_c(\mathbf{r}) + V_{conf} \right] \Psi(\mathbf{r}) = \mathcal{E} \Psi(\mathbf{r}), \quad (21)$$

where V_{conf} is the confinement potential due to the boundary conditions of the NS. Typically, this potential is determined by the E_G mismatch at the interface of two materials.⁸ Then, the basis set is modified to a product of an envelope function (slowly varying over the NS), $F_{nk}(\mathbf{r})$, and the Bloch function, such that: $\Psi(\mathbf{r}) \rightarrow \Psi_{nk}(\mathbf{r}) = F_{nk}(\mathbf{r})u_{nk}(\mathbf{r})$. $F_{nk}(\mathbf{r})$ can be chosen based on the symmetry of the problem. For example, if one has a spherically symmetric QD, then spherical harmonics can be used. Gaussian envelopes are also a common choice. Once the basis set is chosen E_G is calculated following the formalism above,^{28,372,391} Sec. IV B 1.

It is clear that it is difficult to rigorously justify the EFA in a NS, where the boundary conditions become a problem.⁷ As the confined wave-function spreads into the matrix material, the effective mass and dielectric constant changes,³⁹² thus perturbing the wave-function.¹⁸ The EFA is defined in the Luttinger-Kohn representation,³⁷⁰ which defines periodic boundary conditions near the band extrema, where the perturbation expansion occurs, and the Bloch states and energy levels are well defined. However, as real space is reduced, the spread in the momentum space increases and this causes an apparent coupling between higher excited states, which may not be real. This effect results in an increase of the dispersion curve, typically far greater than is predicted by the ETB or EPM method.^{5,373} The increased dispersion exemplifies the need to carefully consider what states are included in a calculation.

a. EMA results. Isolated spherical QDs (infinite confinement potential) were considered in the work of Ref. 28. The Luttinger Hamiltonian was used to model the VB and mass anisotropy was included in the CB along with valley degeneracy. The central feature of this work was to consider the role of excitons in an indirect-gap QD where the bulk dielectric constant was used in the Coulomb term. To this end, the authors used spherical harmonic states for the electrons and the $l=0, 2$ eigenstates of the Luttinger Hamiltonian were used with the radial part given by spherical Bessel functions. The exciton wave-function was written as a product of the electron and hole wave-function including a variational parameter used to minimize the exciton binding energy. The results of Takagahara and Takeda are shown in Fig. 46. Though the method of finding the exciton states is novel, it is clear that the calculated energies are too large for the systems we discussed in Sec. II. From our discussion above and

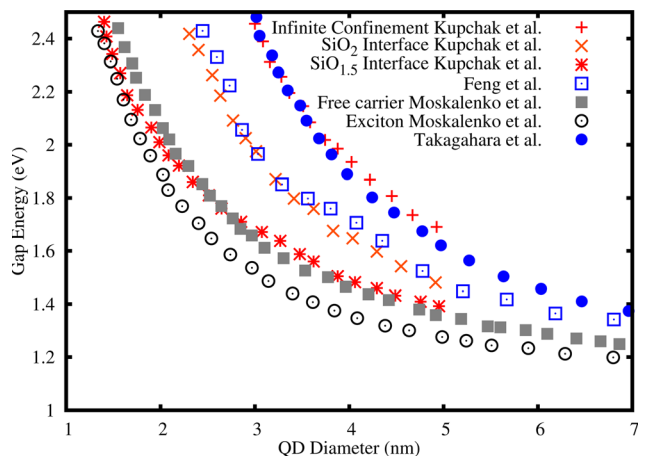


FIG. 46. Theoretical calculations under the effective mass approximation for Si QDs surrounded by SiO_2 , or for the case of infinite confinement. Results for infinite confinement, SiO_2 interface, and $\text{SiO}_{1.5}$ interface are from Ref. 393. Feng *et al.* calculation is from Ref. 29. Free carrier and exciton calculation from Ref. 394. Takagahara and Takeda calculation is from Ref. 28.

from Sec. II, the effect of a sub-stoichiometric interface can not be theoretically overlooked.

In the work of Kupchak *et al.* a novel method was used to deal with the interface issue.³⁹³ The authors considered only a heavy hole state at the Γ -point and an electron state in the X-valley. Therefore, they considered only two-band effects as opposed to the case of Takagahara and Takeda.²⁸ Kupchak *et al.* included exciton effects by considering a product of electron and hole spherical Bessel functions. The result of an infinite confinement potential (Fig. 46) shows no significant difference from the model of Takagahara and Takeda. The effect of the interface was included by modelling a spherical QD embedded in a dielectric medium. Kupchak *et al.* included in the Hamiltonian a polarization (or self-energy) correction term. This potential energy results from the Coulomb interaction with an image charge in the matrix material. The polarization energy was found using a Green's function expansion of a spherical harmonic basis set in Poisson's equation. To model the effect of different interfaces, the authors considered a relative permittivity and effective mass defined between the Si QD and the corresponding interface (SiO_2 or $\text{SiO}_{1.5}$). Such a model both increases the electron and hole energy due to the polarization effect and lowers the confinement barrier. However, it was noted in Refs. 377 and 393 that the polarization energy is not significant and can be treated as a small perturbation for s-like wave-functions. Therefore, the results in Fig. 46 for the SiO_2 and $\text{SiO}_{1.5}$ interface mainly model the effect of finite confinement for excitons. The SiO_2 and $\text{SiO}_{1.5}$ results show good agreement with experimental data from Secs. II A 1, II A 4, and II A 5. We further note that the physics described by this model is a fair representation of QDs created by ion implantation (Sec. III A 4) apart from the correlation effects due to a densely packed distribution of QDs.

A sophisticated model for the interface boundary conditions was given in the work of Moskalenko *et al.*³⁹⁴ The authors considered the same Hamiltonian as in Ref. 393 while retaining VB degeneracy. The central difference in the

model of Moskalenko *et al.* was the inclusion of a modified Bastard type boundary condition considering an SiO₂ interface. The Bastard boundary condition includes the variation of the effective mass at the NS interface.³⁹² The modified wave-functions due to the boundary conditions do not show significant penetration into the matrix material (SiO₂), but do produce more accurate electron and hole energy levels.^{18,394} The interface model of Moskalenko *et al.* (SiO₂) agrees with the SiO_{1.5} interface model of Kupchak *et al.* (Fig. 46). Therefore, the Bastard boundary conditions produce more pronounced and accurate interface effects. Additionally, Moskalenko *et al.* noted that since the polarization effect partly cancels with the electron-hole Coulomb energy (as noted in Ref. 393), the Coulomb energy was calculated as a perturbation to the single particle Hamiltonian. The difference between the exciton and free electron-hole model are shown in Fig. 46. Hence, the models of Refs. 393 and 394 do well to reproduce the experimental data in terms of the interface effects, while strain still should be included per our discussion in Sec. II.

The anisotropy of the CB and the Luttinger Hamiltonian for the VB (similar to Ref. 28) was considered in the work of Feng *et al.*²⁹ Besides the extra VB states, the treatment of the electron, hole, and exciton wave-functions agrees with the formalism of Kupchak *et al.* However, to model exciton effects, the authors included the exchange interaction and considered its effect on bright-dark exciton splitting (Sec. IA 4). Additionally, the authors included a dimensionally dependent effective mass and dielectric constant. The effective mass is known to depend on NS dimension,^{20,363} but how this parameter varies is unclear. Problems with models of a low-dimensional dielectric constant were discussed in Sec. IA 3. Feng *et al.* used a dielectric constant reduced from the bulk value ($\epsilon = 6.52$ from Ref. 395) and slightly larger transverse effective mass ($m_{\perp} = 0.30$). Interestingly, under an infinite confinement model, Feng *et al.* produced the same results (Fig. 46) as Ref. 393 with an SiO₂ interface. We mentioned in Sec. IA 4 that while the exchange interaction is important for understanding the selection rules, the magnitude of the interaction is negligible compared to E_G . Therefore, in the model of Feng *et al.* the variation of the dielectric constant and effective mass were the main contributions in the calculated reduced confinement energy. Caution must be exercised while interpreting these results, because the magnitude of dimensionally dependent parameters is difficult to determine under current theoretical models.

Finally, we briefly mention a few models with the EMA that illustrate the versatility of the theory. A novel approach to the interface problem was given in the work of Ref. 396. In this work, the authors considered interface diffusion according to Fick's model. By inputting this model into the confinement potential and the effective mass, they obtained a temperature and time dependent expression for each parameter. EMA models similar to Refs. 393 and 394 were used in Refs. 384 and 397. However, the authors also included the effect of spatial anisotropy in the wave-functions to simulate non-spherical QDs. This model does well in the case of por-Si (Sec. II A 5). Additionally, spatial anisotropy breaks the

selection rules (Sec. IA 2). Therefore, while the model needs to be rigorously justified in low-dimensional cases, it can be made to agree with experiment and produces physically relevant results.

C. ETB method

A good introduction to this method is given in Ref. 40. A fully detailed treatment is given in Ref. 398. References 7 and 18 provide a survey of the method in low-dimension. Important discussions on the ETB method are given in Refs. 373 and 399.

1. General features of the ETB method for bulk phase

The ETB method is based on solving the Hamiltonian for a lattice built from single atomic Hamiltonians and the interaction term for the lattice (Eq. (16)) using a linear combination of atomic orbitals (LCAO). The valence electrons are considered to be in tightly bound states given by atomic orbitals centred around each atom. As the electrons from neighbouring atoms are brought close together, on the order of the lattice constant, these orbitals will overlap, thus forming a bound state, and when there are sufficiently many atoms an energy band will form.

In the simplest case, it is assumed that only the nearest neighbours interact and that the interaction between the atomic cores is weak. The LCAO is built from Löwdin orbitals, which are constructed such that the wave-functions from neighbouring atoms are orthogonal. Because of the interaction term with the lattice, the full basis set of orbitals includes Bloch functions. With these assumptions, the full Hamiltonian matrix is given in the atomic basis. The energy in a particular band is given by solving the secular equation

$$\det|\mathbb{H} - \mathcal{E}| = 0, \quad (22)$$

where \mathbb{H} is the matrix element between two neighbouring atoms. Considering a simple basis set of s, p orbitals and the two-centre approximation, the only non-zero elements are: $\langle s|H|s \rangle$, $\langle s|H|p_z \rangle$, $\langle p_z|H|p_z \rangle$, and $\langle p_x|H|p_x \rangle$, which are fitted to experiment.

Since the method inherently is concerned with the valence electrons, the valence band is well modelled, while the conduction band is not. There are many corrections one can make for more accurate calculations. For example, 3-centre integrals can be included, using three nearest neighbours, and increasing the basis set to include d-orbitals.⁷ One difficulty is in dealing with corrections due to local charge build-up. A vacancy state can be easily handled by removing it from the basis set, but the local charge correction is not well understood.

2. ETB theory for nanostructures

The validity of the ETB method in a NS is based on the assumption that the parameters fitted from the bulk can be transferred to the NS system. These parameters include fitting the anisotropic CB effective masses along with the VB heavy and light hole masses, and the bulk E_G .³⁷³ Improvements to the model include incorporating

calculations from EPM³⁹⁹ or density functional theory (DFT)⁴⁰⁰ to find the hopping integrals. The boundary conditions are handled by limiting the LCAO basis set.^{54,401–403} Typically, one will model the interface of the NS with a Si-H bond, by fitting the matrix elements of Eq. (22) to the optical gap of SiH₄. Hydrogen termination at the interface and the effect of non-radiative dangling bonds are discussed in Refs. 373 and 399.

ETB is an atomistic method providing an accurate description of atomic states and the boundary conditions, as opposed to the EMA.³⁷³ Since a NS is an atomic-like structure, this is an important advantage of ETB. However, a NS typically has a more complicated interface than being passivated by H alone. H-passivation alone leads to an overestimation of E_G .^{54,394} Additionally, truncation of the basis set means that effects such as tunnelling cannot be directly handled and the inclusion of stress is computationally consuming.¹⁸ Modelling of excitons is a challenge, because the exchange and Coulomb interaction are not well-defined within ETB.^{18,404,405}

NSs with high dimensional anisotropy (e.g., por-Si spheroids or surface grown CVD structures) cannot be accurately modelled within ETB.³⁷³ To a first approximation the shape of a NS can be modelled by varying the size of the basis set along different crystallographic orientations.⁴⁰⁶ However, at the interface, there is a change in the local charge environment from Si-Si (or Ge-Ge) bonds to the bonding environment of the matrix material. On the surface of the NS, D-state defects and dangling bonds exist (Sec. II A 4). Si-O overlap integrals are known and the local density approximation (LDA) is used to correct for the local charge environment.⁷ However, this approach is known to underestimate the gap energy by ≈ 0.5 eV. NS shape has been modelled by replacing TB orbitals with Gaussian envelopes of varying width for different orientations.³⁸⁸ To model the variations in the charge environment, DFT has been used to obtain the hopping integrals within ETB and thus obtain models for NS shape.⁴⁰⁰

a. ETB results. Many of the challenges faced by ETB were carefully addressed in the work of Ref. 373. Niquet *et al.* improved the accuracy by fitting the TB parameters on the bulk band energies along with the electron and hole effective masses. The bulk E_G was fitted with the GW band structure calculation. This fit included the CB anisotropic effective masses and sub-band states. Additionally, Ref. 373 used an sp^3 model up to third-nearest-neighbour and three-centre integrals, including the spin-orbit interaction. The boundary conditions were given through Si-H parameters and charge transfer calculated within LDA. The results of this calculation are shown in Fig. 47. Delerue *et al.*³⁹⁹ obtained identical results with Ref. 373 by fitting the TB parameters to EPM calculations when exciton effects were included. The results of Niquet *et al.* are comparable to Refs. 393 and 394 in Fig. 47 and thus reasonable agreements are obtained with experiment; however, the interface does not represent experimental results (Sec. III).

The H-passivation scheme was considered in great detail in Ref. 403. Tit *et al.* used an sp^3 model up to

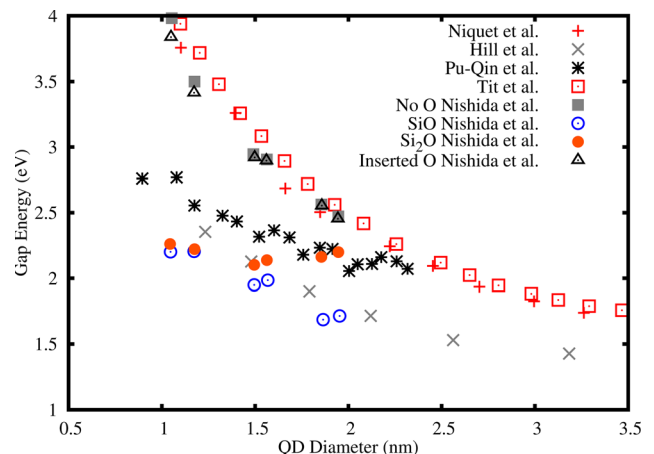


FIG. 47. Theoretical calculations under the empirical tight-binding model for Si QDs. Calculations are from Niquet *et al.*,³⁷³ Hill and Whaley,⁵⁴ Pu-Qin *et al.*,⁴¹⁰ and Tit *et al.*⁴⁰³ Variations in the oxygen configuration at the interface (“No O,” “SiO,” “Si₂O,” and “Inserted O”) are from Ref. 402. “Inserted O” is for an oxygen atom placed between an Si-H bond at the interface.

second-nearest-neighbour, and the atomic positions were calculated within DFT. The Si-H overlap integral was set to reproduce an electronegativity for Si higher than H, because of the ionic character of the Si-H covalent bond. The authors concluded that the effect of a relaxed lattice and their H-passivation scheme enhances the effects of QC and yields a direct-gap character. The results of this calculation (Fig. 47) are identical with Niquet *et al.* In the work of Nishida,^{402,407} sixth-nearest-neighbour interactions were considered in an extended Hückel-type nonorthogonal tight-binding model. The author considered several passivation schemes. In the first case, the Si QD was terminated with H, labelled as “No O” in Fig. 47. Nishida included an oxygen state between the Si-H bond, which is labelled as “Inserted O” in Fig. 47. The overlap integral for ‘Inserted O’ was determined by fitting the molecular orbitals of H₂O. The results are identical with all of the models we have discussed so far. Therefore, it is clear that the number of nearest-neighbours and the parametrization method does not make a significant difference in the final calculated E_G .

To improve the interface configuration, Nishida considered double-bonded (SiO) and backbonded (Si₂O) oxygen configurations (Fig. 47).^{402,407} The backbonded situation was simulated by placing an O atom between two Si atoms at the interface, which were terminated with H. The average bonding angle used was in accordance with nuclear magnetic resonance analysis. The double-bonded configuration was achieved by fitting with ab-initio calculations for silanone. In either case, the overlap integrals were obtained by fitting with O or H-terminated Si surfaces and the charge configuration was included with a charge-dependent potential. The Si₂O interface produced only defect related results, i.e., there is no change in E_G as a function of diameter. The defect energy is very similar to O-related defects discussed in Sec. II C 4a. The SiO configuration agrees with the por-Si QD data in the case of QD oxidation (Sec. II A 5a). Furthermore, Nishida considered the role of oxygen at the interface for the case of QWs.⁴⁰⁸ In Ref. 408, the Si-O-Si bond angle is 180°

for an SiO_4 interface. The author found direct transition behaviour blue-shifting with reduced QW thickness, which does not agree with the predictions of the direct-gap for Si or Ge.⁴⁰⁹ Nishida did find good agreement with the experimental data for MBE QWs of Ref. 352 from Sec. II C 3 a. However, it was stated that the dominant interface state was the Si^{3+} state for this system (Sec. II C 3 a).

The effect of excitons was considered in the work of Ref. 54 (and more detail of the Coulomb and exchange energies was given in Ref. 405). Hill *et al.* used extended Hückel parameters similar to Nishida. In addition, the authors included the Coulomb interaction into the Hamiltonian nonperturbatively by considering the time evolution of a two-particle electron-hole state. The charge configuration was calculated directly over the exciton eigenfunction, which improves the accuracy of the local charge environment. They also included a dimensionally dependent dielectric function. The results of this calculation are shown in Fig. 47. The calculation agrees with the SiO interface of Nishida, demonstrating that accurate charge determination is essential. For comparison, the work of Ref. 410 used 3s and 3p Si orbitals, and ignored overlap integrals (Vogl, Hjalmarson, and Dow parametrization) producing weaker confinement effects, as expected (Fig. 47). The same result was observed for the case of Ge QDs. In the work of Ref. 401, Ge QDs were calculated using the same methods as in the work of Ref. 373. Reference 27 considered the parameters of Vogl for Ge QDs, which produced weaker confinement effects compared with Ref. 401. The Vogl parameters were also considered in the work of Ref. 404 for the case of QWs. Therefore, the incorporation of oxygen at the interface is still a challenge for ETB, while the local charge configuration found a novel solution in the work of Ref. 54.

D. Empirical pseudopotential method

A good introduction to the method is given in Ref. 40. A full detailed treatment is given in Ref. 411. Application of this method for NSs is given in Ref. 7.

1. Bulk theory

The EPM is based on considering the potential due to only valence electrons by removing the effect of core electrons where the potential diverges quite rapidly. This method is based in the orthogonal plane wave method, where the core electron wave functions are made orthogonal to the valence states so they may be diagonalized out of the Hamiltonian. This procedure is accomplished by defining the valence states, $|V\rangle$ (with potential V and energy E), in terms of a projection operator of the core states, $|C\rangle$, such that: $|V\rangle = (1 - \sum |C\rangle\langle C|)|\phi\rangle$. Thus, a pseudo-function, $|\phi\rangle$, is defined in terms of a new pseudopotential, V_{ps}

$$V_{ps} = V + \sum (E - E_C) |C\rangle\langle C|. \quad (23)$$

Since the strong fluctuations at the core are removed, which the valence electrons are assumed not to feel, V_{ps} gives a smoother potential.

With V_{ps} defined in Eq. (23), the Hamiltonian for $|\phi\rangle$ is defined. By the assumptions of the theory, V_{ps} are smooth functions. Therefore, to a first approximation, $|\phi\rangle$ is assumed to be a summation of plane waves, which are periodic in the reciprocal lattice according to Bloch's theorem. Like in the ETB method, the secular equation is formed between $|\phi\rangle$ at two different points in the Brillouin zone. This equation contains the Fourier transform of V_{ps} , which is written as a product of structure and form factors known as the pseudopotential form factors. These factors are fitted to experiment to determine the energy of a particular band.

The Fourier transform of V_{ps} is defined along a discrete lattice of reciprocal vectors. Symmetry can be used to simplify the number of factors to the lowest five.⁴⁰ Thus, like the ETB, this method is an atomistic method, which means it has many of the same features.⁷ In EPM, one determines the form of the crystal potential (pseudopotential) through the underlying crystal structure. Once this potential is known, the psuedo-function is known. On the other hand, in ETB, the form of the wave-function (basis set) is assumed to represent the atomic structure (atomic orbitals). Once the basis set is determined the crystal potential (hopping integrals) is known. Therefore, these two methods have been used in conjunction to improve computational accuracy as we described above (Sec. IV C 2). Hence, many of the results regarding the treatment of the interface and fitting of bulk parameters are carried over in this section from Sec. IV C 2. Furthermore, it should be emphasized that these methods are not strictly applicable to amorphous NSs.⁴⁰⁸

2. EPM for nanostructures

Like in the EMA, one wants to consider a continuous slowly varying confinement potential across the NS. This means that the V_{ps} must be redefined and fitted to experiment with H terminated surfaces.⁴¹² The boundary conditions are dealt with by limiting the basis set of $|\phi\rangle$, and thus the form factors are limited to a finite set. Atomic positions can be dealt with using relaxation models.⁷ Results of this method are found to be nearly identical with the ETB model.^{60,395,412-414} An advantage of EPM is in the ability to treat large NSs.⁴¹² A review of the EPM for NSs is given in Refs. 413 and 415.

a. EPM results. A method was developed in the work of Ref. 412 and 416 to handle large QDs. Wang *et al.* wrote the total crystal potential as a sum of atomic potentials, which were fitted to the bulk Si band structure, effective mass, and surface work function. The atomic positions were determined using relaxation models. They were able to obtain good agreement with the screened LDA bulk potential, which is commonly used in ETB. The Si QDs were passivated with H and the Si-H potentials were obtained by fitting to experimental data for H covered Si surfaces. Wang *et al.* used a plane-wave expansion for the carrier states, which does not represent the atomic nature of the QD, but does allow for computational simplicity. To handle large-sized clusters the authors solved for the expansion coefficients in their basis set variationally within an “energy window.” This

“window” was obtained by only minimizing the energy around a reference energy, which is placed inside E_G . Therefore, only transitions near the CBM and VBM were considered. The results of this calculation are shown in Fig. 48. The results of Wang *et al.* agree with the ETB method of Ref. 373 (Sec. IV C 2). Their calculation is in good agreement with the experimental data from por-Si and co-sputtering (Secs. II A 5 a and II A 1), but does not reflect the correct surface passivation. As we noted (Sec. IV C 2), when oxygen is included a reduction of the E_G is found, which does not agree with experimental data. A similar agreement was seen for calculations of por-Si Q-Wires.⁴¹⁷

A slightly different approach was taken in the work of Bulutay,⁴¹⁴ which produced identical results with Ref. 412. Bulutay developed a method to incorporate sub-band states. The same Hamiltonian and the same basis set (plane-waves) was used by Bulutay as by Wang *et al.* However, Bulutay used a different approach for embedding the QD in a matrix material. The QDs were embedded in an artificial wide-gap matrix material with the same lattice constant as the QD and with an energy offset to simulate an oxide matrix. This entire structure was then placed in a supercell. The result was that Bulutay retained a discrete grid of points in reciprocal space (Sec IV D 1), but explicitly disregarded strain. Discretization allowed Bulutay to incorporate more states and to handle large QDs without the need for an “energy window.” Additionally, Bulutay used semiempirical pseudopotentials as opposed to Wang *et al.* These considerations clearly do not effect E_G , but Bulutay was able to calculate optical absorption spectra with this method.

In the work of Ref. 395, Öğüt *et al.* addressed the problem of computational demand by considering a real-space method. The problem of underestimating E_G within LDA was circumvented by defining the gap energy as the energy of a system with $n+1$ plus $n-1$ electrons including the self-energy (polarization energy) correction. The self-energy correction was rigorously argued for in the work of Ref. 420.

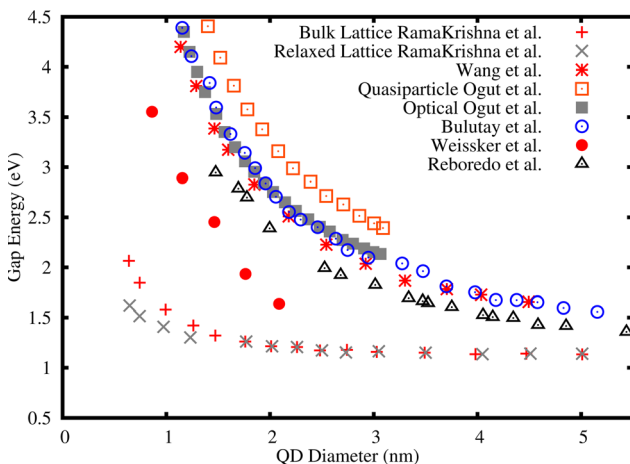


FIG. 48. Theoretical calculations under the empirical pseudopotential method for Si QDs. Calculations are from Wang and Zunger,⁴¹² Bulutay,⁴¹⁴ Weissker *et al.*,⁴¹⁸ and Reboredo *et al.*⁴¹⁹ Krishna and Friesner⁶⁰ calculates for a bulk lattice constant and a relaxed (reduced) lattice constant. Öğüt *et al.*³⁹⁵ calculation for ‘quasiparticle’ refers to an electron-hole pair and ‘optical’ refers to the exciton state.

However, we noted above (Sec. IV B 2) that this effect can be treated as a perturbation. The problem was then redefined in terms of the charge configuration, which was solved using finite-difference EPM. This result is shown in Fig. 48 and labelled as “quasiparticle.” The calculation represents the energy of a free electron-hole pair, which produces a slightly larger E_G than Refs. 412 and 414.

Öğüt *et al.* included exciton effects by calculating the Coulomb energy with a pseudo-function and the dielectric function was given by a generalized Penn model. This result is labelled “optical” in Fig. 48. This correction puts Öğüt *et al.* in perfect agreement with Refs. 412 and 414. In the work of Ref. 419, the same model as Ref. 412 was used with the inclusion of Coulomb and exchange energies, and a dimensionally dependent dielectric function.^{59,421,422} Fig. 48 shows the result of Reboredo *et al.*⁴¹⁹ The inclusion of exciton effects lowers the E_G and gives better agreement with experimental data. The reason for the difference with the calculation of Öğüt *et al.* is that the self-energy term in their calculation was not cancelled out by the corresponding Coulomb interaction arising from the self-energy. Therefore, the results of Refs. 395, 412, and 414 all perfectly agree, while Ref. 419 gives an accurate treatment of the exciton. This agreement shows that the form of the pseudopotential does not make a significant difference in the calculation.

The arrangement of the atoms and the allowed states can dramatically change the calculated energy. In the work of Ref. 418, the Si and Ge atoms were placed within a simple cubic lattice with a Ge-Ge and a Si-Si distance of 0.24 nm and 0.23 nm, respectively. E_G was calculated using DFT-LDA with pseudopotentials. The results of Weissker *et al.* (Fig. 48) show a significant reduction of E_G . Another dramatic change in E_G was obtained in the work of Ref. 60. The method of Krishna *et al.* was similar to all of the results discussed so far. The main difference comes from the fact that Krishna *et al.* considered only transitions between the Γ and X-points. Therefore, coupling with higher energy states was ignored. The results of this calculation (labelled “bulk lattice”) and when the lattice constant was reduced (labelled “relaxed lattice”) are shown in Fig. 48. The same reduction of E_G is seen in Ref. 60 as in Ref. 172, which does not agree with the experimental measurements for a stressed NS (Sec. III). However, the calculation of Krishna *et al.* does agree with experimental results of Secs. II A 4 a and II A 1 a. The same reduction of energy was seen between the EMA and ETB, where it was argued that the EMA exhibits too much dispersion due to artificial coupling.³⁷³

E. Comparison of theories

It is clear that all of the theories presently available face challenges in accurately modelling experimental data. A notable example of this problem was shown in the work of Ref. 219. In this work, Si QDs were formed using ion implantation; the results were discussed in Sec. II A 4 a. The main feature of their results was a measured coupling with the interface states that created a Stoke’s shift between the absorption and emission spectra. Garrido Fernandez *et al.* compared their experimental results with the theoretical

calculations of Delerue *et al.*³⁹⁹ (Sec. IV C 2), Wang and Zunger⁴¹² (Sec. IV D 2), and Takagahara and Takeda²⁸ (Sec. IV B 2). All calculations demonstrated adequate agreement with experimental data, although none use the correct interface states and their calculations were concerned with por-Si. The calculations of Takagahara and Takeda²⁸ and Wang and Zunger⁴¹² are shown in Fig. 49 against por-Si data from Wolkin *et al.*²⁵² (Sec. II A 5 a).

A crystalline NS has a well-defined atomic arrangement that can be modelled by either ETB or EPM, assuming there is no modification of the bulk parameters or atomic states. A NS also has symmetry that can be utilized within the EMA, assuming that the EFA is still valid. The interface is where the picture becomes complicated for any theory. Therefore, it is useful to combine the positive features of each method. The essential feature of the EMA is in the treatment of the confinement potential, whether it is finite or infinite and of what functional form. The $\mathbf{k} \cdot \mathbf{p}$ matrix elements are a product of the orbital quantum numbers, while the radial component is determined by the form of the confinement potential, e.g., spherical harmonics. On the other hand, in ETB atomic orbitals are chosen and then the hopping integral is left to be determined. In the case of EPM, the pseudo-potentials determine the pseudo-functions. In either ETB or EPM, the underlying feature is the atomic lattice.

Several issues have been addressed concerning the validity of any theoretical model for NSs. In the case of the EMA, the initial application of this method used the same assumptions from the bulk state in the NS, such as the inclusion of sub-band states and spin-orbit coupling. This was done in the work of Takagahara and Takeda²⁸ and the result was far too much dispersion in E_G (Fig. 49). This result was criticized by many groups.^{373,399,412,416} Some authors demeaned the method as inherently flawed and pushed to never use this method in the case of a NS.⁴¹³ Several authors have worked to correct this situation and their results are in much better agreement with experimental data. The work of

the group of Moskalenko *et al.*³⁹⁴ provides a realistic picture of NSs. In Fig. 49, Moskalenko *et al.* shows reduced dispersion for small QD diameters from the two-band infinite confinement model of Ref. 20. Experimental data for ion-implanted Si QDs (Fig. 49, Sec. II A 4 a, Ref. 199) is in good agreement with these theoretical models. Furthermore, Refs. 18, 376, and 393 include improvements to the confinement potential by incorporating dielectric screening effects, corrections to the effective mass, and fourth order terms. Stress and defects can also be modelled with the EMA.

The ETB and EPM share the same set of criticisms and advantages. While the main advantage of these methods is the treatment of the atomic configuration, the boundary states cannot be treated accurately at the moment.^{18,393,394} Terminating the NS with H leads to an artificial increase in E_G and we discussed the complications of O termination in Sec. IV C 2. In Fig. 49, excellent agreement is demonstrated between the por-Si experimental data, and the ETB and EPM calculations, which both use H termination methods. Another challenge is to accurately model stress, defects, and the exchange and Coulomb interactions. Several authors have addressed these issues and more sophisticated pseudo-potentials have been used in conjunction with tightly bound states to improve the accuracy of the calculations (Secs. IV D 2 and IV C 2).

No single calculation has considered all of the available experimental data. Some calculations ignore the interface, while others ignore stress, and therefore it is difficult to ascertain the exact magnitude of each parameter. To accurately model a NS, it is essential that all experimental parameters pertaining to a particular method of preparation are included in the model. Likely the biggest challenge is how to accurately model the interface. None of the theoretical methods were initially developed for NSs, which is why the interface is a problem. In the case of the EMA, one can easily vary the strength of the confinement potential to represent the E_G offset corresponding to different sub-stoichiometric states at the interface. However, such a treatment does not account for interface coupling that may present. We noted above (Sec. IV) that interface pinning differs between QDs, QWs, and Q-Wires. Potentially, DFT could be used to calculate the pinning energy and this could be easily included in an ETB or EPM calculation.

The Coulomb energy correction due to the self-energy effect was described in Ref. 420 in order to correct the calculation of Ref. 395. It is not clear how important this term is since the dielectric function is not accurately known. The dielectric function should vary with NS dimension, but the magnitude of this effect is not clear (Sec. I A 3). The effective mass must also vary with dimension and across the interface, but again the magnitude is not clear (Secs. II C 1 a). The surface polarization effect was argued to be not important in the work of Ref. 393. An improved model for surface trapped states was given in the work of Refs. 18 and 423. Another effect that is commonly ignored in calculations is the size distribution of QDs, which is central to understanding QDs produced by ion implantation (Sec. II A 4 a). This effect was studied in the work of Ref. 424 and used to improve the calculation of Ref. 395. All of these

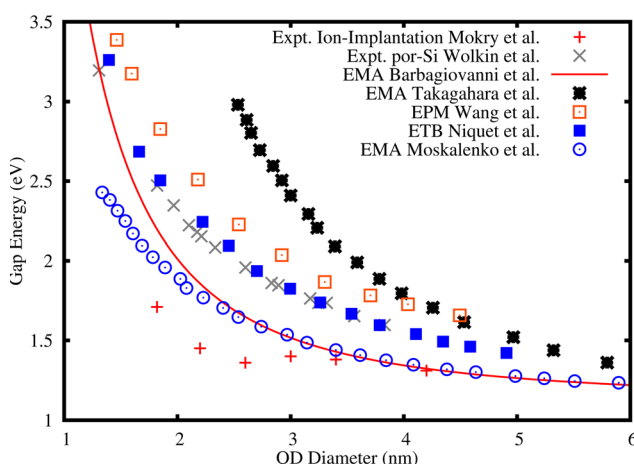


FIG. 49. Comparison of different theoretical models with experimental data. “Expt. Ion-Implantation” data are from Ref. 199. “Expt. por-Si” data are from Ref. 252. “EMA Barbagiovanni *et al.*” are from Ref. 20. “EMA Takagahara and Takeda” are from Ref. 28. “EPM Wang and Zunger” are from Ref. 412. “ETB Niquet *et al.*” are from Ref. 373. “EMA Moskalenko *et al.*” are from Ref. 394.

considerations must be closely examined for accuracy since all methods are inherently empirical.

V. CONCLUSIONS

We have reviewed a variety of fabrication methods in Sec. II and the physical parameters that arise for each method. Special attention was paid to the fact that within a single fabrication method, there is variety in the observed experimental results and also between fabrication methods. We found that in the case of Si NSs embedded in or layered with SiO_2 , the role of sub-oxide interface states was important. The Si^{1+} state pins hole states, Si^{2+} acts as a deep level defect, and Si^{3+} tends to relieve stress in the NS. Dangling bonds at the interface can shift the energy by roughly 0.6 eV. NSs with a thick interface exhibit higher levels of stress. Interface states lower the confinement energy and increase interface scattering. Lattice mismatch is also a source of stress. The value of the effective mass can change due to interface scattering, crystallinity, and dimensionality. In addition, amorphous NSs exhibit stronger effects compared to the crystalline system. Ge NSs are inherently more difficult to control during fabrication than Si. O defect states are particularly a problem in the case of Ge NS due to Ge diffusion and GeO desorption. Ge NSs routinely exhibit stress due to the formation of a thick oxide interface.

The magnitude of the above-stated structural effects is enhanced in the case of QDs, due to the large surface to volume ratio. Co-sputtered QDs tend to exhibit Si^{1+} at the interface. Reactive sputtered QDs have a thick interface containing all sub-oxide states and are highly stressed. PECVD QDs also have a thick interface, which dominates the Si-Si bonds. Si_3N_4 states in embedded PECVD QDs have a large change in the E_G , partly due to N contamination. MBE Ge QDs experience alloying in the case of a Si substrate, while SiO_2 or TiO_2 substrates exhibit a wide PL band associated with defect states along with a QC-induced PL. Ion implantation suffers from a large concentration of oxide defect states. For moderate implantation conditions, the interface is well controlled and QC PL is clearly seen, though the hole state is pinned. Por-Si QDs or Q-Wires have a large concentration of dangling bonds at the interface, which increases the influence of sub-oxide states, and their number increases for smaller structures.

Q-Wires do not show strong signs of QC, due to a large fraction of defects produced during fabrication. VLS Q-Wires contain metallic state contamination with notable defect PL and stress. OAG Q-Wires require chemical etching to thin the wires and remove the effect of a thick oxide sheath.

QWs are characterized by a lattice mismatch induced strain and exhibit strong diffusion at the interface during annealing. Magnetron sputtered and PECVD QWs tend to form QDs within the Si layer due to oxide diffusion. However, in the case of PECVD QWs, if the Si layer remains amorphous, clear signs of QC PL are observed. MBE QWs suffer a similar diffusion problem; however, it predominantly leads to a thinning of the Si QW layer. Epi-SOI QWs

have a sharper interface than SIMOX-SOI QWs; in either case, defect and QC PL is observed.

From a theoretical perspective, the effective mass approximation, the tight-binding model, and the pseudopotential method were reviewed. In each case, we highlighted how the method is best adapted to deal with variations in the experimental conditions. The effective mass approximation is not well designed to accurately model the boundary conditions but can consider perturbations to the NS. On the other hand, the opposite is true for the tight-binding and pseudopotential methods. In any case, each method must consider the experimental conditions appropriate to the method of NC fabrication.

- ¹V. Mitin, D. Sementsov, and N. Vagidov, *Quantum Mechanics for Nanostructures* (Cambridge Univ. Press, Cambridge, 2010).
- ²R. Feynman, *J. Microelectromech. Syst.* **1**, 60 (1992).
- ³W. D. Heiss, *Quantum Dots: A Doorway to Nanoscale Physics* (Springer, Berlin, 2005).
- ⁴M. Leijnse and K. Flensberg, *Phys. Rev. B* **84**, 140501(R) (2011).
- ⁵E. G. Barbagiovanni, L. V. Goncharova, and P. J. Simpson, *Phys. Rev. B* **83**, 035112 (2011).
- ⁶L. Jacak, P. Hawrylak, and A. Wójs, *Quantum Dots* (Springer, Berlin, 1998).
- ⁷C. Delerue and M. Lannoo, *Nanostructures: Theory and Modelling* (Springer, Berlin, 2004).
- ⁸P. Harrison, *Quantum Wells, Wires, and Dots*, 3rd ed. (John Wiley & Sons Ltd., West Sussex, 2009).
- ⁹J. H. Davies, *The Physics of Low-Dimensional Semiconductors: An Introduction* (Cambridge Univ. Press, Cambridge, 1998).
- ¹⁰F. Flory, L. Escoubas, and G. Berginc, *J. Nanophotonics* **5**, 052502 (2011).
- ¹¹R. Rurali, *Rev. Mod. Phys.* **82**, 427 (2010).
- ¹²A. D. Yoffe, *Adv. Phys.* **51**, 799 (2002).
- ¹³J. Fan and P. K. Chu, *Small* **6**, 2080 (2010).
- ¹⁴V. A. Belyakov, V. A. Burdov, R. Lockwood, and A. Meldrum, *Adv. Opt. Technol.* **2008**, 279502.
- ¹⁵C. Cimpean, V. Groenewegen, V. Kuntermann, A. Sommer, and C. Kryschi, *Laser Photonics Rev.* **3**, 138 (2009).
- ¹⁶J. Heitmann, F. Müller, M. Zacharias, and U. Gösele, *Adv. Mater.* **17**, 795 (2005).
- ¹⁷D. J. Lockwood, *J. Mater. Sci: Mater. Electron.* **20**, 235 (2009).
- ¹⁸O. B. Gusev, A. N. Poddubny, A. A. Prokofiev, and I. N. Yassievich, *Semiconductors* **47**, 183 (2013).
- ¹⁹Z. Zhang, R. Zou, L. Yu, and J. Hu, *CRC Crit. Rev. Solid State Sci.* **36**, 148 (2011).
- ²⁰E. G. Barbagiovanni, D. J. Lockwood, P. J. Simpson, and L. V. Goncharova, *J. Appl. Phys.* **111**, 034307 (2012).
- ²¹B. R. Nag, *Physics of Quantum Well Devices* (Kluwer Academic Publishers, Dordrecht, 2000).
- ²²J. D. B. Bradley, P. E. Jessop, and A. P. Knights, *Appl. Phys. Lett.* **86**, 241103.1 (2005).
- ²³S. S. Iyer and Y. H. Xie, *Science* **260**, 40 (1993).
- ²⁴L. Tsybeskov and D. J. Lockwood, *Proc. IEEE* **97**, 1284 (2009).
- ²⁵M. S. Hybertsen, *Phys. Rev. Lett.* **72**, 1514 (1994).
- ²⁶D. Kovalev, H. Heckler, M. Ben-Chorin, G. Polisski, M. Schwartzkopff, and F. Koch, *Phys. Rev. Lett.* **81**, 2803 (1998).
- ²⁷P. Alfaro, A. Miranda, A. E. Ramos, and M. Cruz-Irisson, *Braz. J. Phys.* **36**, 375 (2006).
- ²⁸T. Takagahara and K. Takeda, *Phys. Rev. B* **46**, 15578 (1992).
- ²⁹D. H. Feng, Z. Z. Xu, T. Q. Jia, X. X. Li, and S. Q. Gong, *Phys. Rev. B* **68**, 035334 (2003).
- ³⁰C. Garcia, B. Garrido, P. Pellegrino, R. Ferre, J. A. Moreno, J. R. Morante, L. Pavesi, and M. Cazzanelli, *Appl. Phys. Lett.* **82**, 1595 (2003).
- ³¹W. D. A. M. de Boer, D. Timmerman, K. Dohnalova, I. N. Yassievich, H. Zhang, W. J. Buma, and T. Gregorkiewicz, *Nat. Nanotechnol.* **5**, 878 (2010).
- ³²B. Delley and E. F. Steigmeier, *Phys. Rev. B* **47**, 1397 (1993).
- ³³A. Miranda, J. L. Cuevas, A. E. Ramos, and M. Cruz-Irisson, *Microelectron. J.* **40**, 796 (2009).

- ³⁴G. F. Grom, D. J. Lockwood, J. P. McCaffrey, H. J. Labbe, P. M. Fauchet, B. White, J. Diener, D. Kovalev, F. Koch, and L. Tsybeskov, *Nature* **407**, 358 (2000).
- ³⁵C. R. Pidgeon, P. J. Phillips, D. Carder, B. N. Murdin, T. Fromherz, D. J. Paul, W. X. Ni, and M. Zhao, *Semicond. Sci. Technol.* **20**, L50 (2005).
- ³⁶H. Haug and S. W. Koch, *Quantum Theory of the Optical and Electronic Properties of Semiconductors* (World Scientific Publishing Co., Singapore, 2004).
- ³⁷D. F. Walls and G. J. Milburn, *Quantum Optics* (Springer, Berlin, 2008).
- ³⁸S. Mirabella, R. Agosta, G. Franzò, I. Crupi, M. Miritello, R. L. Savio, M. A. D. Stefano, S. D. Marco, F. Simone, and A. Terrasi, *J. Appl. Phys.* **106**, 103505 (2009).
- ³⁹S. Glutsch, *Excitons in Low-Dimensional Semiconductors: Theory, Numerical Methods, Applications* (Springer, Berlin, 2004).
- ⁴⁰P. Y. Yu and M. Cardona, *Fundamentals of Semiconductors: Physical and Material Properties*, 3rd ed. (Springer, Berlin, 2001).
- ⁴¹M. L. Brongersma, P. G. Kik, A. Polman, K. S. Min, and H. A. Atwater, *Appl. Phys. Lett.* **76**, 351 (2000).
- ⁴²S. Lütjohann, C. Meier, M. Offer, A. Lorke, and H. Wiggers, *Europhys. Lett.* **79**, 37002 (2007).
- ⁴³L. Pavese, L. D. Negro, C. Mazzoleni, G. Franzò, and F. Priolo, *Nature* **408**, 440 (2000).
- ⁴⁴V. I. Klimov, *Science* **290**, 314 (2000).
- ⁴⁵Y. Suwa and S. Saito, *Phys. Rev. B* **79**, 233308 (2009).
- ⁴⁶S. Saito, Y. Suwa, H. Arimoto, N. Sakuma, D. Hisamoto, H. Uchiyama, J. Yamamoto, T. Sakamizu, T. Mine, S. Kimura, T. Sugawara, and M. Aoki, *Appl. Phys. Lett.* **95**, 241101 (2009).
- ⁴⁷M. J. Süess, R. Geiger, R. A. Minamisawa, G. Schiefler, J. Frigerio, D. Chrastina, G. Isella, R. Spolenak, J. Faist, and H. Sigg, *Nat. Photonics* **7**, 466 (2013).
- ⁴⁸J. Liu, X. Sun, R. Camacho-Aguilera, L. C. Kimerling, and J. Michel, *Opt. Lett.* **35**, 679 (2010).
- ⁴⁹R. S. Knox, *Theory of Excitons* (Academic, New York, 1963).
- ⁵⁰G. D. Scholes and G. Rumbles, *Nature Mater.* **5**, 683 (2006).
- ⁵¹R. D. Schaller, V. M. Agranovich, and V. I. Klimov, *Nat. Phys.* **1**, 189 (2005).
- ⁵²M. C. Beard, K. P. Knutsen, P. Yu, J. M. Luther, Q. Song, W. K. Metzger, R. J. Ellingson, and A. J. Nozik, *Nano Lett.* **7**, 2506 (2007).
- ⁵³A. J. Nozik, *Nat. Photonics* **6**, 272 (2012).
- ⁵⁴N. A. Hill and K. B. Whaley, *Phys. Rev. Lett.* **75**, 1130 (1995).
- ⁵⁵C. Klingshirn, *Semiconductor Optics* (Springer, Berlin, 2005).
- ⁵⁶T. Suemoto, K. Tanaka, A. Nakajima, and T. Itakura, *Phys. Rev. Lett.* **70**, 3659 (1993).
- ⁵⁷P. D. J. Calcott, K. J. Nash, L. T. Canham, M. J. Kane, and D. Brumhead, *J. Phys.: Condens. Matter* **5**, L91 (1993).
- ⁵⁸D. Babic and R. Tsu, *Superlattices Microstruct.* **22**, 581 (1997).
- ⁵⁹L. W. Wang and A. Zunger, *Phys. Rev. Lett.* **73**, 1039 (1994).
- ⁶⁰M. V. R. Krishna and R. A. Friesner, *J. Chem. Phys.* **96**, 873 (1992).
- ⁶¹H. Haken, *Nuovo Cimento* **3**, 1230 (1956).
- ⁶²O. Verzelen, R. Ferreira, and G. Bastard, *Phys. Rev. B* **64**, 075315 (2001).
- ⁶³J. Martin, F. Cichos, F. Huisken, and C. von Borczyskowski, *Nano Lett.* **8**, 656 (2008).
- ⁶⁴J. Singh, D. Birkedal, V. G. Lyssenko, and J. M. Hvam, *Phys. Rev. B* **53**, 15909 (1996).
- ⁶⁵G. Bacher, R. Weigand, J. Seufert, V. D. Kulakovskii, N. A. Gippius, A. Forchel, K. Leonardi, and D. Hommel, *Phys. Rev. Lett.* **83**, 4417 (1999).
- ⁶⁶E. K. Lee, D. J. Lockwood, J. M. Baribeau, A. M. Bratkovsky, T. I. Kamins, and L. Tsybeskov, *Phys. Rev. B* **79**, 233307 (2009).
- ⁶⁷M. Combescot and O. Betbeder-Matibet, *Phys. Rev. B* **80**, 205313 (2009).
- ⁶⁸A. Wojs and P. Hawrylak, *Phys. Rev. B* **55**, 13066 (1997).
- ⁶⁹T. M. Lu, N. C. Bishop, T. Pluym, J. Means, P. G. Kotula, J. Cederberg, L. A. Tracy, J. Dominguez, M. P. Lilly, and M. S. Carroll, *Appl. Phys. Lett.* **99**, 043101 (2011).
- ⁷⁰S. D. Sarma, R. Sousa, X. Hu, and B. Koiller, *Solid State Commun.* **133**, 737 (2005).
- ⁷¹Q. Li, Ł. Cywiński, D. Culcer, X. Hu, and S. Das Sarma, *Phys. Rev. B* **81**, 085313 (2010).
- ⁷²E. Poem, O. Kenneth, Y. Kodriano, Y. Benny, S. Khatsevich, J. Avron, and D. Gershoni, *Phys. Rev. Lett.* **107**, 087401 (2011).
- ⁷³L. Liu, *Phys. Rev.* **126**, 1317 (1962).
- ⁷⁴R. Winkler, *Spin Orbit Coupling Effects in Two-Dimensional Electron and Hole Systems* (Springer, Berlin, 2003).
- ⁷⁵D. Kovalev, H. Heckler, G. Polisski, J. Diener, and F. Koch, *Opt. Mater.* **17**, 35 (2001).
- ⁷⁶G. W. Hanson, *Fundamentals of Nanoelectronics* (Prentice Hall, New Jersey, 2008).
- ⁷⁷W. H. Lim, C. H. Yang, F. A. Zwanenburg, and A. S. Dzurak, *Nanotechnology* **22**, 335704 (2011).
- ⁷⁸F. A. Zwanenburg, C. E. W. M. van Rijmenam, Y. Fang, C. M. Lieber, and L. P. Kouwenhoven, *Nano Lett.* **9**, 1071 (2009).
- ⁷⁹A. L. Smirl, E. J. Loren, J. Rioux, J. E. Sipe, and H. M. van Driel, in *Quantum Electronics and Laser Science Conference* (Optical Society of America, 2010), p. 3.
- ⁸⁰C. Simmons, J. Prance, B. V. Bael, T. Koh, Z. Shi, D. Savage, M. Lagally, R. Joynt, M. Friesen, S. Coppersmith, and M. Eriksson, *Phys. Rev. Lett.* **106**, 156804 (2011).
- ⁸¹B. V. Kamenev, G. F. Grom, D. J. Lockwood, J. P. McCaffrey, B. Laikhtman, and L. Tsybeskov, *Phys. Rev. B* **69**, 235306 (2004).
- ⁸²L. Tsybeskov, G. F. Grom, P. M. Fauchet, J. P. McCaffrey, J.-M. Baribeau, G. I. Sproule, and D. J. Lockwood, *Appl. Phys. Lett.* **75**, 2265 (1999).
- ⁸³D. D. Ma, C. S. Lee, F. C. K. Au, S. Y. Tong, and S. T. Lee, *Science* **299**, 1874 (2003).
- ⁸⁴H. E. Schaefer, *Nanoscience: The Science of the Small in Physics, Engineering, Chemistry, Biology and Medicine* (Springer, Berlin, 2010).
- ⁸⁵*Nanostructure Science and Technology*, edited by A. Korkin, P. S. Krstić, and J. C. Wells (Springer, New York, 2010).
- ⁸⁶R. J. Martín-Palma and A. Lakhtakia, *Nanotechnology: A Crash Course* (Society of Photo-Optical Instrumentation Engineers, Bellingham, 2010).
- ⁸⁷*Single Semiconductor Quantum Dots*, edited by P. Michler (Springer, Berlin, 2009).
- ⁸⁸K. J. Vahala, *Nature* **424**, 839 (2003).
- ⁸⁹A. Amo, D. Sanvitto, F. P. Laussy, D. Ballarini, E. del Valle, M. D. Martin, A. Lemaitre, J. Bloch, D. N. Krizhanovskii, M. S. Skolnick, C. Tejedor, and L. Viña, *Nature* **457**, 291 (2009).
- ⁹⁰D. P. DiVincenzo, D. Bacon, J. Kempe, G. Burkard, and K. B. Whaley, *Nature* **408**, 339 (2000).
- ⁹¹S. Nadji-Perge, S. M. Frolov, E. P. A. M. Bakkers, and L. P. Kouwenhoven, *Nature* **468**, 1084 (2010).
- ⁹²F. Patolsky and C. M. Lieber, *Mater. Today* **8**, 20 (2005).
- ⁹³J. L. West and N. J. Halas, *Curr. Opin. Biotechnol.* **11**, 215 (2000).
- ⁹⁴S. K. Ray, S. Maikap, W. Banerjee, and S. Das, *J. Phys. D: Appl. Phys.* **46**, 153001 (2013).
- ⁹⁵V. Aroutiounian, S. Petrosyan, A. Khachatrian, and K. Touryan, *J. Appl. Phys.* **89**, 2268 (2001).
- ⁹⁶A. J. Nozik, *Physica E* **14**, 115 (2002).
- ⁹⁷K. Tanabe, *Energies* **2**, 504 (2009).
- ⁹⁸H. J. Joyce, Q. Gao, H. H. Tan, C. Jagadish, Y. Kim, J. Zou, L. M. Smith, H. E. Jackson, J. M. Yarrison-Rice, P. Parkinson, and M. B. Johnston, *Prog. Quantum Electron.* **35**, 23 (2011).
- ⁹⁹W. E. Hagston, T. Störner, and F. Rasul, *J. Appl. Phys.* **89**, 1087 (2001).
- ¹⁰⁰*Handbook of Luminescent Semiconductor Materials*, edited by L. Bergman and J. L. McHale (CRC Press, Boca Raton, 2011).
- ¹⁰¹L. Mangolini, *J. Vac. Sci. Technol. B* **31**, 020801 (2013).
- ¹⁰²Z. Xie, E. J. Henderson, O. Dag, W. Wang, J. E. Lofgreen, C. Kübel, T. Scherer, P. M. Brodersen, Z. Z. Gu, and G. A. Ozin, *J. Am. Chem. Soc.* **133**, 5094 (2011).
- ¹⁰³J. Wilcoxon, G. Samara, and P. Provencio, *Phys. Rev. B* **60**, 2704 (1999).
- ¹⁰⁴D. P. Puzzo, E. J. Henderson, M. G. Helander, Z. Wang, G. A. Ozin, and Z. Lu, *Nano Lett.* **11**, 1585 (2011).
- ¹⁰⁵M. W. Dashiell, U. Denker, C. Müller, G. Costantini, C. Manzano, K. Kern, and O. G. Schmidt, *Appl. Phys. Lett.* **80**, 1279 (2002).
- ¹⁰⁶G. E. Cirlin, P. Werner, G. Gösele, B. V. Volovik, V. M. Ustinov, and N. N. Ledentsov, *Tech. Phys. Lett.* **27**, 14 (2001).
- ¹⁰⁷D. Grützmacher, T. Fromherz, C. Dais, J. Stangl, E. Müller, Y. Ekinci, H. H. Solak, H. Sigg, R. T. Lechner, E. Wintersberger, S. Birner, V. Holý, and G. Bauer, *Nano Lett.* **7**, 3150 (2007).
- ¹⁰⁸Z. Yang, Y. Shi, J. Liu, B. Yan, R. Zhang, Y. Zheng, and K. Wang, *Mater. Lett.* **58**, 3765 (2004).
- ¹⁰⁹J. M. Baribeau, X. Wu, N. L. Rowell, and D. J. Lockwood, *J. Phys.: Condens. Matter* **18**, R139 (2006).
- ¹¹⁰J. M. Baribeau, N. L. Rowell, and D. J. Lockwood, “Self-assembled $\text{Si}_{1-x}\text{Ge}_x$ dots and islands,” in *Self-Organized Nanoscale Materials*, edited by M. Adachi and D. J. Lockwood (Springer, New York, 2006) pp. 1–70.
- ¹¹¹J. N. Aqua, I. Berbezíer, L. Favre, T. Frisch, and A. Ronda, *Phys. Rep.* **522**, 59 (2013).
- ¹¹²M. P. Halsall, H. Omi, and T. Ogino, *Appl. Phys. Lett.* **81**, 2448 (2002).

- ¹¹³J. H. Davies, *The Physics of Low-dimensional Semiconductors: An Introduction* (Cambridge University Press, Cambridge, 1998).
- ¹¹⁴K. Brunner, *Rep. Prog. Phys.* **65**, 27 (2002).
- ¹¹⁵D. Depla, S. Mahieu, and J. E. Greene, "Sputter deposition processes," in *Handbook of Deposition Technologies for Films and Coatings: Science, Applications and Technology*, 3rd ed., edited by P. M. Martin (Elsevier Inc., Oxford, 2010), pp. 253–296.
- ¹¹⁶M. D. Strikovski, J. Kim, and S. H. Kolagani, "Plasma energetics in pulsed laser and pulsed electron deposition," in *Springer Handbook of Crystal Growth*, edited by G. Dhanaraj, K. Byrappa, V. Prasad, and M. Dudley (Springer, Berlin, 2010), pp. 1193–1211.
- ¹¹⁷D. Mattox, *Handbook of Physical Vapour Deposition (PVD) Processing: Film Formation, Adhesion, Surface Preparation and Contamination Control* (Noyes Publications, New Jersey, 1998).
- ¹¹⁸S. Godefroo, M. Hayne, M. Jivanescu, A. Stesmans, M. Zacharias, O. I. Lebedev, G. V. Tendeloo, and V. V. Moshchalkov, *Nat. Nanotechnol.* **3**, 174 (2008).
- ¹¹⁹M. Molinari, H. Rinnert, M. Vergnat, and P. Weisbecker, *Mater. Sci. Eng., B* **101**, 186 (2003).
- ¹²⁰H. Rinnert, M. Vergnat, and A. Burneau, *J. Appl. Phys.* **89**, 237 (2001).
- ¹²¹G. Seguini, S. Schamm-Chardon, P. Pellegrino, and M. Perego, *Appl. Phys. Lett.* **99**, 082107 (2011).
- ¹²²L. Titova, T. Cocker, D. Cooke, X. Wang, A. Meldrum, and F. Hegmann, *Phys. Rev. B* **83**, 085403 (2011).
- ¹²³T. van Buuren, L. N. Dinh, L. L. Chase, W. J. Siekhaus, and L. J. Terminello, *Phys. Rev. Lett.* **80**, 3803 (1998).
- ¹²⁴C. Bostedt, T. van Buuren, T. M. Willey, N. Franco, L. J. Terminello, C. Heske, and T. Möller, *Appl. Phys. Lett.* **84**, 4056 (2004).
- ¹²⁵J. Derr, K. Dunn, D. Riabinina, F. Martin, M. Chaker, and F. Rosei, *Physica E* **41**, 668 (2009).
- ¹²⁶T. Orii, M. Hirasawa, T. Seto, N. Aya, and S. Onari, *Eur. Phys. J. D* **24**, 119 (2003).
- ¹²⁷D. Riabinina, C. Durand, J. Margot, M. Chaker, G. A. Botton, and F. Rosei, *Phys. Rev. B* **74**, 075334 (2006).
- ¹²⁸S. I. Shah, G. H. Jaffari, E. Yassitepe, and B. Ali, "Evaporation: Processes, bulk microstructures, and mechanical properties," in *Handbook of Deposition Technologies for Films and Coatings: Science, Applications and Technology*, 3rd ed., edited by P. M. Martin (Elsevier Inc., Oxford, 2010), pp. 135–252.
- ¹²⁹J. F. Ziegler, J. P. Biersack, and U. Littmark, *The Stopping and Range of Ions in Matter* (Pergamon Press, New York, 1985), see <http://www.srim.org/>.
- ¹³⁰L. V. Dao, X. Wen, M. T. T. Do, P. Hannaford, E. C. Cho, Y. H. Cho, and Y. Huang, *J. Appl. Phys.* **97**, 013501 (2005).
- ¹³¹Y. Maeda, *Phys. Rev. B* **51**, 1658 (1995).
- ¹³²S. Hayashi, Y. Kanzawa, M. Kataoka, T. Nagareda, and K. Yamamoto, *Z. Phys. D* **26**, 144 (1993).
- ¹³³W. Zhang, S. Zhang, and Y. L. T. Chen, *J. Cryst. Growth* **311**, 1296 (2009).
- ¹³⁴A. Sa'ar, Y. Reichman, M. Dovrat, D. Krapf, J. Jedrzejewski, and I. Balberg, *Nano Lett.* **5**, 2443 (2005).
- ¹³⁵S. Takeoka, M. Fujii, S. Hayashi, and K. Yamamoto, *Phys. Rev. B* **58**, 7921 (1998).
- ¹³⁶B. Zhang, S. Shrestha, M. A. Green, and G. Conibeer, *Appl. Phys. Lett.* **96**, 261901 (2010).
- ¹³⁷B. Zhang, S. Shrestha, P. Aliberti, M. A. Green, and G. Conibeer, *Thin Solid Films* **518**, 5483 (2010).
- ¹³⁸M. Fujii, S. Hayashi, and K. Yamamoto, *Appl. Phys. Lett.* **57**, 2692 (1990).
- ¹³⁹M. Dovrat, Y. Goshen, J. Jedrzejewski, I. Balberg, and A. Saar, *Phys. Rev. B* **69**, 155311 (2004).
- ¹⁴⁰M. Alonso, I. Marcus, M. Garriga, A. G. ni, J. Jedrzejewski, and I. Balberg, *Phys. Rev. B* **82**, 045302 (2010).
- ¹⁴¹X. Wen, L. V. Dao, P. Hannaford, E. C. Cho, Y. H. Cho, and M. A. Green, *New J. Phys.* **9**, 337 (2007).
- ¹⁴²J. S. de Sousa, E. W. S. Caetanoa, J. R. Gonçalves, G. A. Farias, V. N. Freire, and E. F. da Silva, Jr., *Appl. Surf. Sci.* **190**, 166 (2002).
- ¹⁴³S. Kim, M. C. Kim, S. Cho, K. J. Kim, H. N. Hwang, and C. C. Hwang, *Appl. Phys. Lett.* **91**, 103113 (2007).
- ¹⁴⁴S. Furukawa and T. Miyasato, *Phys. Rev. B* **38**, 5726 (1988).
- ¹⁴⁵X. Wen, L. V. Dao, and P. Hannaford, *J. Phys. D: Appl. Phys.* **40**, 3573 (2007).
- ¹⁴⁶S. Kim, Y. M. Park, S. H. Choi, K. J. Kim, and D. H. Choi, *J. Phys. D: Appl. Phys.* **40**, 1339 (2007b).
- ¹⁴⁷B. Julsgaard, Y. M. Lu, P. Balling, and A. N. Larsen, *Appl. Phys. Lett.* **95**, 183107 (2009).
- ¹⁴⁸P. Clauws, *Mater. Sci. Eng., B* **36**, 213 (1996).
- ¹⁴⁹Y. Maeda, N. Tsukamoto, and Y. Yazawa, *Appl. Phys. Lett.* **59**, 3168 (1991).
- ¹⁵⁰Y. Kanemitsu, H. Uto, Y. Masumoto, and Y. Maeda, *Appl. Phys. Lett.* **61**, 2187 (1992).
- ¹⁵¹S. Takeoka, M. Fujii, S. Hayashi, and K. Yamamoto, *Appl. Phys. Lett.* **74**, 1558 (1999).
- ¹⁵²B. Zhang, W. Truong, S. Shrestha, M. A. Green, and G. Conibeer, *Physica E* **45**, 207 (2012).
- ¹⁵³W. K. Choi, Y. W. Ho, S. P. Ng, and V. Ng, *J. Appl. Phys.* **89**, 2168 (2001).
- ¹⁵⁴M. Zacharias and P. M. Fauchet, *Appl. Phys. Lett.* **71**, 380 (1997).
- ¹⁵⁵J. O. Carlsson and P. M. Martin, "Chemical vapor deposition," in *Handbook of Deposition Technologies for Films and Coatings: Science, Applications and Technology*, 3rd ed., edited by P. M. Martin (Elsevier Inc., Oxford, 2010), pp. 314–363.
- ¹⁵⁶L. Martinu, O. Zabeida, and J. E. Klemborg-Sapieha, "Plasma-enhanced chemical vapor deposition of functional coatings," in *Handbook of Deposition Technologies for Films and Coatings: Science, Applications and Technology*, 3rd ed., edited by P. M. Martin (Elsevier Inc., Oxford, 2010), pp. 392–465.
- ¹⁵⁷R. Dhanasekaran, "Growth of semiconductor single crystals from vapor phase," in *Springer Handbook of Crystal Growth*, edited by G. Dhanaraj, K. Byrappa, V. Prasad, and M. Dudley (Springer, Berlin, 2010), pp. 897–935.
- ¹⁵⁸C. Meier, S. Lüttjohann, M. Offer, H. Wiggers, and A. Lorke, *Adv. Solid State Phys.* **48**, 79 (2009).
- ¹⁵⁹H. Takagi, H. Ogawa, Y. Yamazaki, A. Ishizaki, and T. Nakagiri, *Appl. Phys. Lett.* **56**, 2379 (1990).
- ¹⁶⁰Y. Kanemitsu and S. Okamoto, *Phys. Rev. B* **58**, 9652 (1998).
- ¹⁶¹Y. Kanemitsu, T. Ogawa, K. Shiraishi, and K. Takeda, *Phys. Rev. B* **48**, 4883 (1993).
- ¹⁶²G. Ledoux, J. Gong, F. Huisken, O. Guillois, and C. Reynaud, *Appl. Phys. Lett.* **80**, 4834 (2002).
- ¹⁶³C. Reynaud, O. Guillois, N. Herlin-Boime, G. Ledoux, and F. Huisken, *Mater. Res. Soc. Symp. Proc.* **832**, F6.2.1 (2005).
- ¹⁶⁴F. Iacona, G. Franzo, and C. Spinella, *J. Appl. Phys.* **87**, 1295 (2000).
- ¹⁶⁵L. A. Nesbit, *Appl. Phys. Lett.* **46**, 38 (1985).
- ¹⁶⁶T. V. Torchynska, *J. Non-Cryst. Solids* **352**, 2484 (2006).
- ¹⁶⁷B. Zaknoon, G. Bahir, C. Saguy, and R. Edrei, *Nano Lett.* **8**, 1689 (2008).
- ¹⁶⁸T. Inokuma, Y. Wakayama, T. Muramoto, R. Aoki, Y. Kurata, and S. Hasegawa, *J. Appl. Phys.* **83**, 2228 (1998).
- ¹⁶⁹N. M. Park, C. J. Choi, T. Y. Seong, and S. J. Park, *Phys. Rev. Lett.* **86**, 1355 (2001).
- ¹⁷⁰D. Wen-Ge, Y. Jing, M. Ling-Hai, W. Shu-Jie, Y. Wei, and F. Guang-Sheng, *Commun. Theor. Phys.* **55**, 688 (2011).
- ¹⁷¹W. Yu, J. Y. Zhang, W. G. Ding, and G. S. Fu, *Eur. Phys. J. B* **57**, 53 (2007).
- ¹⁷²F. A. Reboredo and A. Zunger, *Phys. Rev. B* **62**, R2275 (2000).
- ¹⁷³D. W. Kim, Y. H. Kim, X. Chen, C. H. Lee, S. C. Song, F. E. Prins, D. L. Kwong, and S. Banerjee, *J. Vac. Sci. Technol., B* **19**, 1104 (2001).
- ¹⁷⁴S. N. M. Mestanza, I. Doi, and N. C. Frateschi, *J. Integr. Circuits Syst.* **2**, 81 (2007). Available at www.sbmicro.org.br/jics/html/artigos/vol2no2/04.pdf.
- ¹⁷⁵J. Shieh, T. S. Ko, H. L. Chen, B. T. Dai, and T. C. Chu, *Chem. Vap. Deposition* **10**, 265 (2004).
- ¹⁷⁶R. Wei, N. Deng, M. Wang, S. Zhang, and P. Chen, in *Proceedings of 2005 5th IEEE Conference on Nanotechnology* (2005), Vol. 2.
- ¹⁷⁷K. W. Sun, S. H. Sue, and C. W. Liu, *Physica E* **28**, 525 (2005).
- ¹⁷⁸P. Boucaud, V. Le Thanh, S. Sauvage, D. Debarre, D. Bouchier, and J. M. Lourtioz, *Thin Solid Films* **336**, 240 (1998).
- ¹⁷⁹J. Huang, Z. Ye, B. Zhao, X. Ma, Y. Wang, and D. Que, *Appl. Phys. Lett.* **78**, 1858 (2001).
- ¹⁸⁰I. V. Markov, "Nucleation at surfaces," in *Springer Handbook of Crystal Growth*, edited by G. Dhanaraj, K. Byrappa, V. Prasad, and M. Dudley (Springer, Berlin, 2010), pp. 17–52.
- ¹⁸¹H. Hirayama and H. Asahi, "Molecular beam epitaxy with gaseous source," in *Handbook of Crystal Growth*, edited by D. T. J. Hurle (Elsevier Science, Amsterdam, 1994), pp. 184–221.
- ¹⁸²D. Vvedensky, "Epitaxial growth of semiconductors," in *Low-Dimensional Semiconductor Structures*, edited by K. Barnham and D. Vvedensky (Cambridge University Press, Cambridge, 2001), pp. 1–55.
- ¹⁸³O. P. Pchelyakov, Y. B. Bolkhovityanov, A. V. Dvurechenskii, A. I. Nikiforov, A. I. Yakimov, and B. Voigtländer, *Thin Solid Films* **367**, 75 (2000).

- ¹⁸⁴E. Søndergård, R. Kofman, P. Cheyssac, and A. Stella, *Surf. Sci.* **364**, 467 (1996).
- ¹⁸⁵O. G. Schmidt, C. Lange, K. Eberl, O. Kienzle, and F. Ernst, *Appl. Phys. Lett.* **71**, 2340 (1997).
- ¹⁸⁶H. Baumgärtner, F. Kaesen, H. Gossner, and I. Eisele, *Appl. Surf. Sci.* **130**, 747 (1998).
- ¹⁸⁷V. V. Afanasev, M. Badylevich, A. Stesmans, A. Laha, H. J. Osten, and A. Fissel, *Appl. Phys. Lett.* **95**, 102107 (2009).
- ¹⁸⁸A. Fissel, A. Laha, E. Bugiel, D. Kühne, M. Czernohorsky, R. Dargis, and H. J. Osten, *Microelectron. J.* **39**, 512 (2008).
- ¹⁸⁹J. L. Bischoff, H. Mortada, D. Dentel, M. Derivaz, C. Ben Azzouz, A. Akremi, C. Chefí, F. Miguel Morales, M. Herrera, J. Manuel Mánuel, R. García, and M. Diani, *Phys. Status Solidi A* **209**, 657 (2012).
- ¹⁹⁰H. Mortada, D. Dentel, M. Derivaz, J. L. Bischoff, E. Denys, R. Moubah, C. Ulhaq-Bouillet, and J. Werckmann, *J. Cryst. Growth* **323**, 247 (2011).
- ¹⁹¹D. A. Pavlov, P. A. Shlyayev, E. V. Korotkov, and N. O. Krivulin, *Tech. Phys. Lett.* **36**, 548 (2010).
- ¹⁹²X. Wang, Z. M. Jiang, H. J. Zhu, F. Lu, D. Huang, C. W. Hu, Y. Chen, Z. Zhu, T. Yao, and X. Liu, *Appl. Phys. Lett.* **71**, 3543 (1997).
- ¹⁹³A. A. Shklyaev and M. Ichikawa, *Surf. Sci.* **514**, 19 (2002).
- ¹⁹⁴D. J. Lockwood, N. L. Rowell, I. Berbezier, G. Amiard, A. Ronda, M. Faustini, and D. Gross, *J. Electrochem. Soc.* **157**, H1160 (2010).
- ¹⁹⁵A. Konchenko, Y. Nakayama, I. Matsuda, S. Hasegawa, Y. Nakamura, and M. Ichikawa, *Phys. Rev. B* **73**, 113311 (2006).
- ¹⁹⁶N. L. Rowell, D. J. Lockwood, I. Berbezier, P. D. Szkutnik, and A. Ronda, *J. Electrochem. Soc.* **156**, H913 (2009).
- ¹⁹⁷D. J. Lockwood, N. L. Rowell, I. Berbezier, G. Amiard, L. Favre, A. Ronda, and D. Gross, *ECS Trans.* **28**, 33 (2010).
- ¹⁹⁸M. Nastasi and J. W. Mayer, *Ion Implantation and Synthesis of Materials* (Springer, Berlin, 2006).
- ¹⁹⁹C. R. Mokry, P. J. Simpson, and A. P. Knights, *J. Appl. Phys.* **105**, 114301 (2009).
- ²⁰⁰S. N. Dedyulin, M. P. Singh, F. S. Razavi, and L. V. Goncharova, *Nucl. Instrum. Methods Phys. Res. B* **288**, 60 (2012).
- ²⁰¹P. J. Simpson, C. R. Mokry, and A. P. Knights, *J. Phys.: Conf. Ser.* **265**, 012022 (2011).
- ²⁰²M. L. Brongersma, A. Polman, K. S. Min, and H. A. Atwater, *J. Appl. Phys.* **86**, 759 (1999).
- ²⁰³S. Guha, S. B. Qadri, R. G. Musket, M. A. Wall, and T. Shimizu-Iwayama, *J. Appl. Phys.* **88**, 3954 (2000).
- ²⁰⁴C. Bonafos, B. Colombeau, A. Altimbelli, M. Carrada, G. B. Assayag, B. Garrido, M. López, A. Pérez-Rodríguez, J. R. Morante, and A. Claverie, *Nucl. Instrum. Methods Phys. Res. B* **178**, 17 (2001).
- ²⁰⁵C. Bonafos, B. Garrido, M. Lopez, A. Perez-Rodriguez, J. R. Morante, T. Kihn, G. B. Assayag, and A. Claverie, *Mater. Sci. Eng., B* **70**, 380 (2000).
- ²⁰⁶B. Garrido, M. López, O. González, A. Pérez-Rodríguez, J. R. Morante, and C. Bonafos, *Appl. Phys. Lett.* **77**, 3143 (2000).
- ²⁰⁷U. Serincan, M. Kulakci, R. Turan, S. Foss, and T. G. Finstad, *Nucl. Instrum. Methods Phys. Res. B* **254**, 87 (2007).
- ²⁰⁸T. S. Iwayama, T. Hama, D. E. Hole, and I. W. Boyd, *Vacuum* **81**, 179–185 (2006).
- ²⁰⁹U. S. Sias, E. C. Moreira, E. Ribeiro, H. Boudinov, L. Amaral, and M. Behar, *J. Appl. Phys.* **95**, 5053 (2004).
- ²¹⁰W. Skorupa, R. A. Yankov, I. E. Tyschenko, H. Fröb, T. Böhme, and K. Leo, *Appl. Phys. Lett.* **68**, 2410 (1996).
- ²¹¹M. Yamamoto, T. Koshikawa, T. Yasue, H. Harima, and K. Kajiyama, *Thin Solid Films* **369**, 100 (2000).
- ²¹²L. Nikolova, R. G. Saint-Jacques, C. Dahmounea, and G. G. Ross, *Surf. Coat. Technol.* **203**, 2501 (2009).
- ²¹³E. P. O'Reilly and J. Robertson, *Phys. Rev. B* **27**, 3780 (1983).
- ²¹⁴A. Stesmans and V. V. Afanasev, *J. Appl. Phys.* **97**, 033510 (2005).
- ²¹⁵H. Z. Song and X. M. Bao, *Phys. Rev. B* **55**, 6988 (1997).
- ²¹⁶R. Tohmon, Y. Shimogaichi, H. Mizuno, Y. Ohki, K. Nagasawa, and Y. Hama, *Phys. Rev. Lett.* **62**, 1388 (1989).
- ²¹⁷S. Guha, M. D. Pace, D. N. Dunn, and I. L. Singer, *Appl. Phys. Lett.* **70**, 1207 (1997).
- ²¹⁸C. J. Nicklaw, M. P. Pagey, S. T. Pantelides, D. M. Fleetwood, R. D. Schrimpf, K. F. Galloway, E. J. Wittig, B. M. Howard, E. Taw, W. H. McNeil, and J. F. Conley, Jr., *IEEE Trans. Nucl. Sci.* **47**, 2269 (2000).
- ²¹⁹B. Garrido Fernandez, M. López, C. García, A. Pérez-Rodríguez, J. R. Morante, C. Bonafos, M. Carrada, and A. Claverie, *J. Appl. Phys.* **91**, 798 (2002).
- ²²⁰D. Pacifici, E. Moreira, G. Franzò, V. Martorino, F. Priolo, and F. Iacona, *Phys. Rev. B* **65**, 144109 (2002).
- ²²¹M. López, B. Garrido, C. García, P. Pellegrino, A. Pérez-Rodríguez, J. R. Morante, C. Bonafos, M. Carrada, and A. Claverie, *Appl. Phys. Lett.* **80**, 1637 (2002).
- ²²²A. Stesmans, *J. Appl. Phys.* **88**, 489 (2000).
- ²²³D. I. Telbaum, A. N. Mikhaylov, O. N. Gorshkov, A. P. Kasatkin, A. I. Belov, D. M. Gaponova, and S. V. Morozov, *Vacuum* **78**, 519 (2005).
- ²²⁴I. D. Sharp, Q. Xu, D. O. Yi, C. W. Yuan, J. W. Beeman, K. M. Yu, J. W. Ager, D. C. Chrzan, and E. E. Haller, *J. Appl. Phys.* **100**, 114317 (2006).
- ²²⁵E. G. Barbagiovanni, S. N. Dedyulin, P. J. Simpson, and L. V. Goncharova, *Nucl. Instrum. Methods Phys. Res. B* **272**, 74 (2012b).
- ²²⁶K. Hirose, H. Nohira, K. Azuma, and T. Hattori, *Prog. Surf. Sci.* **82**, 3 (2007).
- ²²⁷L. Ding, T. P. Chen, Y. Liu, M. Yang, and J. I. Wong, *J. Appl. Phys.* **101**, 103525 (2007).
- ²²⁸U. S. Sias, L. Amaral, M. Behar, H. Boudinov, and E. C. Moreira, *Nucl. Instrum. Methods Phys. Res. B* **250**, 178 (2006).
- ²²⁹J. Linnros, N. Lalic, A. Galeckas, and V. Grivickas, *J. Appl. Phys.* **86**, 6128 (1999).
- ²³⁰V. I. Klimov, C. J. Schwarza, D. W. McBranch, and C. W. White, *Appl. Phys. Lett.* **73**, 2603 (1998).
- ²³¹M. V. Minke and K. A. Jackson, *J. Non-Cryst. Solids* **351**, 2310 (2005).
- ²³²U. V. Desnica, M. Buljan, P. Dubcek, Z. Siketic, I. B. Radovic, S. Bernstorff, U. Serincan, and R. Turan, *Nucl. Instrum. Methods Phys. Res. B* **249**, 843 (2006).
- ²³³K. Prabhakaran, F. Maeda, Y. Watanabe, and T. Ogino, *Appl. Phys. Lett.* **76**, 2244 (2000).
- ²³⁴S. N. M. Mestanza, I. Doi, J. W. Swart, and N. C. Frateschi, *J. Mater. Sci.* **42**, 7757 (2007).
- ²³⁵J. P. Zhao, D. X. Huang, Z. Y. Chen, W. K. Chu, B. Makarenkov, A. J. Jacobson, B. Bahrim, and J. W. Rabalais, *J. Appl. Phys.* **103**, 124304 (2008).
- ²³⁶C. F. Yu, D. S. Chao, Y. F. Chen, and J. H. Liang, *Nucl. Instrum. Methods Phys. Res. B* **307**, 171 (2013).
- ²³⁷L. Rebohle, J. von Borany, R. A. Yankov, W. Skorupa, I. E. Tyschenko, H. Fröb, and K. Leo, *Appl. Phys. Lett.* **71**, 2809 (1997).
- ²³⁸X. L. Wu, T. Gao, G. G. Siu, S. Tong, and M. Bao, *Appl. Phys. Lett.* **74**, 2420 (1999).
- ²³⁹K. S. Min, K. V. Shcheglov, C. M. Yang, H. A. Atwater, M. L. Brongersma, and A. Polman, *Appl. Phys. Lett.* **68**, 2511 (1996).
- ²⁴⁰H. B. Kim, K. H. Chae, C. N. Whang, J. Y. Jeong, M. S. Oh, S. Im, and J. H. Song, *J. Lumin.* **80**, 281 (1998).
- ²⁴¹R. Salh, L. Fitting, E. V. Kolesnikova, A. A. Sitnikova, M. V. Zamoryanskaya, B. Schmidt, and H. J. Fitting, *Semiconductors* **41**, 381 (2007).
- ²⁴²J. M. Schmeltzer and J. M. Buriak, “Recent developments in the chemistry and chemical applications of porous silicon,” in *The Chemistry of Nanomaterials*, edited by C. N. R. Rao, A. Müller, and A. K. Cheetham (Wiley, Weinheim, 2004), Vol. 2, pp. 518–547.
- ²⁴³D. J. Lockwood, *Solid State Commun.* **92**, 101 (1994).
- ²⁴⁴S. Schuppler, S. L. Friedman, M. A. Marcus, D. L. Adler, Y. H. Xie, F. M. Ross, Y. J. Chabal, T. D. Harris, L. E. Brus, W. L. Brown, E. E. Chaban, P. F. Szajowski, S. B. Christman, and P. H. Citrin, *Phys. Rev. B* **52**, 4910 (1995).
- ²⁴⁵L. T. Canham, T. I. Cox, A. Loni, and A. J. Simons, *Appl. Surf. Sci.* **102**, 436 (1996).
- ²⁴⁶L. Stalmans and J. Poortmans, *Prog. Photovoltaics* **6**, 233 (1998).
- ²⁴⁷B. Hamilton, *Semicond. Sci. Technol.* **10**, 1187 (1995).
- ²⁴⁸A. G. Cullis, L. T. Canham, and P. D. J. Calcott, *J. Appl. Phys.* **82**, 909 (1997).
- ²⁴⁹L. Brus, *J. Phys. Chem.* **98**, 3575 (1994).
- ²⁵⁰L. T. Canham, *Appl. Phys. Lett.* **57**, 1046 (1990).
- ²⁵¹R. Boukherroub, S. Morin, D. D. M. Wayner, F. Bensebba, G. I. Sproule, J. M. Baribeau, and D. J. Lockwood, *Chem. Mater.* **13**, 2002 (2001).
- ²⁵²M. V. Wolkin, J. Jorne, P. M. Fauchet, G. Allan, and C. Delerue, *Phys. Rev. Lett.* **82**, 197 (1999).
- ²⁵³I. Sychugov, R. Juhasz, J. Valenta, and J. Linnros, *Phys. Rev. Lett.* **94**, 087405 (2005).
- ²⁵⁴D. J. Lockwood, A. Wang, and B. Bryskiewicz, *Solid State Commun.* **89**, 587 (1994).
- ²⁵⁵L. Z. Kun, K. Y. Lan, C. Hao, H. Ming, and Q. Yu, *Chin. Phys. Lett.* **22**, 984 (2005).

- ²⁵⁶Z. Sui, P. P. Leong, I. P. Herman, G. S. Higashi, and H. Temkin, *Appl. Phys. Lett.* **60**, 2086 (1992).
- ²⁵⁷L. K. Pan, C. Q. Sun, B. K. Tay, T. P. Chen, and S. Li, *J. Phys. Chem. B* **106**, 11725 (2002).
- ²⁵⁸C. Q. Sun, L. K. Pan, Y. Q. Fu, B. K. Tay, and S. Li, *J. Phys. Chem. B* **107**, 5113 (2003).
- ²⁵⁹R. M'ghaieth, H. Maâref, I. Mihalcescu, and J. C. Vial, *Microelectron. J.* **30**, 695 (1999).
- ²⁶⁰D. Kovalev, H. Heckler, M. Ben-Chorin, G. Polisski, M. Schwartzkopff, and F. Koch, *J. Porous Mater.* **7**, 85 (2000).
- ²⁶¹J. C. Vial, A. Bsisy, F. Gaspard, and R. Herino, *Phys. Rev. B* **45**, 14171 (1992).
- ²⁶²L. J. Lauhon, M. S. Gudiksen, D. Wang, and C. M. Lieber, *Nature* **420**, 57 (2002).
- ²⁶³Y. Li, F. Qian, J. Xiang, and C. M. Lieber, *Mater. Today* **9**, 18 (2006).
- ²⁶⁴C. Thelander, P. Agarwal, S. Brongersma, J. Eymery, L. F. Feiner, A. Forchel, M. Scheffler, W. Riess, B. J. Ohlsson, U. Gösele, and L. Samuelson, *Mater. Today* **9**, 28 (2006).
- ²⁶⁵W. Lu and C. M. Lieber, *J. Phys. D: Appl. Phys.* **39**, R387 (2006).
- ²⁶⁶N. Wang, Y. Cai, and R. Q. Zhang, *Mater. Sci. Eng., R* **60**, 1 (2008).
- ²⁶⁷R. S. Wagner and W. C. Ellis, *Appl. Phys. Lett.* **4**, 89 (1964).
- ²⁶⁸H. Adhikari, P. C. McIntyre, A. F. Marshall, and C. E. D. Chidsey, *J. Appl. Phys.* **102**, 094311 (2007).
- ²⁶⁹V. Grossi, L. Ottaviano, S. Santucci, and M. Passacantando, *J. Non-Cryst. Solids* **356**, 1988 (2010).
- ²⁷⁰T. Hanrath and B. A. Korgel, *J. Am. Chem. Soc.* **124**, 1424 (2002).
- ²⁷¹P. Rudolph, "Defect formation during crystal growth from the melt," in *Springer Handbook of Crystal Growth*, edited by G. Dhanaraj, K. Byrappa, V. Prasad, and M. Dudley (Springer, Berlin, 2010), pp. 159–201.
- ²⁷²Y. Wu, Y. Cui, L. Huynh, C. J. Barrelet, D. C. Bell, and C. M. Lieber, *Nano Lett.* **4**, 433 (2004).
- ²⁷³P. K. Sekhar, S. N. Sambandam, D. K. Sood, and S. Bhansali, *Nanotechnology* **17**, 4606 (2006).
- ²⁷⁴K. W. Kolasinski, *Surface Science: Foundations of Catalysis and Nanoscience*, 2nd ed. (Wiley, West Sussex, 2008).
- ²⁷⁵Y. Cui, L. J. Lauhon, M. S. Gudiksen, J. Wang, and C. M. Lieber, *Appl. Phys. Lett.* **78**, 2214 (2001).
- ²⁷⁶J. D. Holmes, K. P. Johnston, R. C. Doty, and B. A. Korgel, *Science* **287**, 1471 (2000).
- ²⁷⁷A. Lugstein, M. Steinmair, Y. J. Hyun, G. Hauer, P. Ponratz, and E. Bertagnoli, *Nano Lett.* **8**, 2310 (2008).
- ²⁷⁸N. Ozaki, Y. Ohno, and S. Takeda, *Appl. Phys. Lett.* **73**, 3700 (1998).
- ²⁷⁹B. V. Kamenev, V. Sharma, L. Tsypeskov, and T. I. Kamins, *Phys. Status Solidi A* **202**, 2753 (2005).
- ²⁸⁰K. Das, A. K. Chakraborty, M. L. NandaGoswami, R. K. Shingha, A. Dhar, K. S. Coleman, and S. K. Ray, *J. Appl. Phys.* **101**, 074307 (2007).
- ²⁸¹X. H. Sun, C. Didychuk, X. T. Zhou, F. Heigl, L. Armelao, T. Regier, R. I. R. Blyth, and T. K. Sham, *Can. Light Source* **22**, 59 (2007). Available at http://www.lightsource.ca/about/pdf/activity_report_2007/22_Sham.pdf.
- ²⁸²F. Sunqi, Y. Dapeng, Z. Hongzhou, B. Zhigang, D. Yu, H. Qingling, Z. Yinghua, and W. Jingjing, *Sci. China, Ser. A* **42**, 1316 (1999).
- ²⁸³P. Noé, J. Guignard, P. Gentile, E. Delamadeleine, V. Calvo, P. Ferret, F. Dhalluin, and T. Baron, *J. Appl. Phys.* **102**, 016103 (2007).
- ²⁸⁴C. C. Hong, W. J. Liao, and J. G. Hwu, *Appl. Phys. Lett.* **82**, 3916 (2003).
- ²⁸⁵A. T. Chu, T. T. N. Thi, T. T. Tran, B. N. Vu, T. T. Pham, V. T. Pham, T. H. Pham, and H. D. Pham, *Adv. Nat. Sci.: Nanosci. Nanotechnol.* **2**, 035004 (2011).
- ²⁸⁶N. H. Quang, N. T. Truc, and Y. M. Niquet, *Comput. Mater. Sci.* **44**, 21 (2008).
- ²⁸⁷Y. F. Zhang, Y. H. Tang, N. Wang, D. P. Yu, C. S. Lee, I. Bello, and S. T. Lee, *Appl. Phys. Lett.* **72**, 1835 (1998).
- ²⁸⁸C. P. Li, X. H. Sun, N. B. Wong, C. S. Lee, S. T. Lee, and B. K. Teo, *Chem. Phys. Lett.* **365**, 22 (2002).
- ²⁸⁹S. T. Lee, R. Q. Zhang, and Y. Lifshitz, "Oxide-assisted growth of silicon and related nanowires: Growth mechanism, structure and properties," in *The Chemistry of Nanomaterials*, edited by C. N. R. Rao, A. Müller, and A. K. Cheetham (Wiley, Weinheim, 2004), Vol. 1, pp. 308–370.
- ²⁹⁰R. G. Hobbs, S. Barth, N. Petkov, M. Zirngast, C. Marschner, M. Morris, and J. D. Holmes, *J. Am. Chem. Soc.* **132**, 13742 (2010).
- ²⁹¹Y. Zhang, Y. Tang, N. Wang, C. Lee, I. Bello, and S. Lee, *Phys. Rev. B* **61**, 4518 (2000).
- ²⁹²S. T. Lee, N. Wang, and C. S. Lee, *Mater. Sci. Eng., A* **286**, 16 (2000).
- ²⁹³Y. Yao, F. Li, and S. T. Lee, *Chem. Phys. Lett.* **406**, 381 (2005).
- ²⁹⁴R. Q. Zhang, Y. Lifshitz, and S. T. Lee, *Adv. Mater.* **15**, 635 (2003).
- ²⁹⁵C. P. Li, C. S. Lee, X. L. Ma, N. Wang, R. Q. Zhang, and S. T. Lee, *Adv. Mater.* **15**, 607 (2003).
- ²⁹⁶Y. F. Zhang, Y. H. Tang, C. Lam, N. Wang, C. S. Lee, I. Bello, and S. T. Lee, *J. Cryst. Growth* **212**, 115 (2000b).
- ²⁹⁷T. K. Sham, S. J. Naftel, P. S. Kim, R. Sammynaiken, Y. H. Tang, I. Coulthard, A. Moewes, J. W. Freeland, Y. F. Hu, and S. T. Lee, *Phys. Rev. B* **70**, 045313 (2004).
- ²⁹⁸X. H. Sun, Y. H. Tang, P. Zhang, S. J. Naftel, R. Sammynaiken, T. K. Sham, H. Y. Peng, Y. F. Zhang, N. B. Wong, and S. T. Lee, *J. Appl. Phys.* **90**, 6379 (2001).
- ²⁹⁹D. J. Lockwood and A. G. Wang, *Solid State Commun.* **94**, 905 (1995).
- ³⁰⁰H. S. Seo, X. Li, H. D. Um, B. Yoo, J. H. K. K. P. Kim, Y. W. Cho, and J. H. Lee, *Mater. Lett.* **63**, 2567 (2009).
- ³⁰¹B. Wu, A. Kumar, and S. Pamarthi, *J. Appl. Phys.* **108**, 051101 (2010).
- ³⁰²K. R. Williams, K. Gupta, and M. Wasilik, *J. Microelectromech. Syst.* **12**, 761 (2003).
- ³⁰³P. H. Yih, V. Saxena, and A. J. Steckl, *Phys. Status Solidi B* **202**, 605 (1997).
- ³⁰⁴M. Sekine, *Appl. Surf. Sci.* **192**, 270 (2002).
- ³⁰⁵G. Jäger-Waldau, H. U. Habermeier, G. Zwicker, and E. Bucher, *J. Electron. Mater.* **23**, 363 (1994).
- ³⁰⁶H. Yoshioka, N. Morioka, J. Suda, and T. Kimoto, *J. Appl. Phys.* **109**, 064312 (2011).
- ³⁰⁷J. Valenta, R. Juhasz, and J. Linnros, *Appl. Phys. Lett.* **80**, 1070 (2002).
- ³⁰⁸A. Wellner, R. E. Palmer, J. G. Zheng, C. J. Kiely, and K. W. Kolasinski, *J. Appl. Phys.* **91**, 3294 (2002).
- ³⁰⁹S. Schuppler, S. L. Friedman, M. A. Marcus, D. L. Adler, Y.-H. Xie, F. M. Ross, T. D. Harris, W. L. Brown, Y. J. Chabal, L. E. Brus, and P. H. Citrin, *Phys. Rev. Lett.* **72**, 2648 (1994).
- ³¹⁰J. von Behren, T. van Buuren, M. Zacharias, E. H. Chimowitz, and P. M. Fauchet, *Solid State Commun.* **105**, 317 (1998).
- ³¹¹Q. Zhang and S. C. Bayliss, *J. Appl. Phys.* **79**, 1351 (1996).
- ³¹²Y. Kanemitsu, *J. Lumin.* **100**, 209 (2002).
- ³¹³B. T. Sullivan, D. J. Lockwood, H. J. Labb  , and Z. H. Lu, *Appl. Phys. Lett.* **69**, 3149 (1996).
- ³¹⁴B. A. Wilson, C. M. Taylor, and J. P. Harbison, *Phys. Rev. B* **34**, 8733 (1986).
- ³¹⁵D. J. Lockwood, *Phase Transitions* **68**, 151 (1999).
- ³¹⁶T. Mchedlidze, T. Arguirov, S. Kouteva-Arguirova, G. Jia, M. Kittler, R. R  olver, B. Berghoff, M. F  rst, D. L. B  tzner, and B. Spangenberg, *Thin Solid Films* **516**, 6800 (2008).
- ³¹⁷D. J. Lockwood and L. Tsybeskov, *Encyclopedia Nanosci. Nanotechnol.* **6**, 477 (2004).
- ³¹⁸M. Bonfanti, E. Grilli, M. Guzzi, M. Virgilio, G. Grosso, D. Chrastina, G. Isella, H. von K  nel, and A. Neels, *Phys. Rev. B* **78**, 041407 (2008).
- ³¹⁹M. Bonfanti, E. Grilli, M. Guzzi, D. Chrastina, G. Isella, H. von K  nel, and H. Sigg, *Physica E* **41**, 972 (2009).
- ³²⁰D. Chrastina, A. Neels, M. Bonfanti, M. Virgilio, G. Isella, E. Grilli, M. Guzzi, G. Grosso, H. Sigg, and H. von K  nel, in *2008, 5th IEEE International Conference on Group IV Photonics* (2008), p. 194.
- ³²¹M. Virgilio, M. Bonfanti, D. Chrastina, A. Neels, G. Isella, E. Grilli, M. Guzzi, G. Grosso, H. Sigg, and H. von K  nel, *Phys. Rev. B* **79**, 075323 (2009).
- ³²²M. Bollani, E. M  ller, S. Signoretti, C. Beeli, G. Isella, M. Kummer, and H. von K  nel, *Mater. Sci. Eng., B* **101**, 102 (2003).
- ³²³M. J. S  uss, L. Carroll, H. Sigg, A. Diaz, D. Chrastina, G. Isella, E. M  ller, and R. Spolenak, *Mater. Sci. Eng., B* **177**, 696 (2012).
- ³²⁴T. M. Burbaev, V. A. Kurbatov, A. O. Pogosov, M. M. Rzaev, and N. N. Sibiel'din, *Semiconductors* **37**, 207 (2003).
- ³²⁵Y. H. Kuo, Y. K. Lee, Y. Ge, S. Ren, J. E. Roth, T. I. Kamins, D. A. B. Miller, and J. S. Harris, *Nature* **437**, 1334 (2005).
- ³²⁶U. Menczigar, G. Abstreiter, J. Olajos, H. Grimmeiss, H. Kibbel, H. Presting, and E. Kasper, *Phys. Rev. B* **47**, 4099 (1993).
- ³²⁷P. A. M. Rodrigues, M. A. Ara  jo Silva, G. A. Narvaez, F. Cerdeira, and J. C. Bean, *Braz. J. Phys.* **29**, 547 (1999).
- ³²⁸A. Laha, E. Bugiel, M. Jestremski, R. Ranjith, A. Fissel, and H. J. Osten, *Nanotechnology* **20**, 475604 (2009).
- ³²⁹Z. H. Lu, J. M. Baribeau, and D. J. Lockwood, *J. Appl. Phys.* **76**, 3911 (1994).
- ³³⁰P. A. M. Rodrigues, M. A. Ara  jo Silva, F. Cerdeira, and J. C. Bean, *Phys. Rev. B* **48**, 18024 (1993).
- ³³¹S. B. Samavedam, M. T. Currie, T. A. Langdo, and E. A. Fitzgerald, *Appl. Phys. Lett.* **73**, 2125 (1998).
- ³³²G. G. Qin, S. Y. Ma, Z. C. Ma, W. H. Zong, and Y. Li-ping, *Solid State Commun.* **106**, 329 (1998).

- ³³³H. Xiao, S. Huang, J. Zheng, G. Xie, and Y. Xie, *Microelectron. Eng.* **86**, 2342 (2009).
- ³³⁴S. Huang, H. Xiao, and S. Shou, *Appl. Surf. Sci.* **255**, 4547 (2009).
- ³³⁵B. Averboukh, R. Huber, K. W. Cheah, Y. R. Shen, G. G. Qin, Z. C. Ma, and W. H. Zong, *J. Appl. Phys.* **92**, 3564 (2002).
- ³³⁶C. Ternon, F. Gourbilleau, R. Rizk, and C. Dufour, *Physica E* **16**, 517 (2003).
- ³³⁷E. C. Cho, J. Xia, A. G. Aberle, and M. A. Green, *Sol. Energy Mater. Sol. Cells* **74**, 147 (2002).
- ³³⁸S. Cosentino, M. Miritello, I. Crupi, G. Nicotra, F. Simone, C. Spinella, A. Terrasi, and S. Mirabella, *Nanoscale Res. Lett.* **8**, 128 (2013).
- ³³⁹L. Heikkila, T. Kuusela, H. P. Hedman, and H. Ihantola, *Appl. Surf. Sci.* **133**, 84 (1998).
- ³⁴⁰R. Röller, O. Winkler, M. Först, B. Spangenberg, and H. Kurz, *Microelectron. Reliab.* **45**, 915 (2005).
- ³⁴¹R. Röller, S. Brünninghoff, M. Först, B. Spangenberg, and H. Kurz, *J. Vac. Sci. Technol., B* **23**, 3214 (2005).
- ³⁴²T. Mchedlidze, T. Arguirov, M. Kittler, R. Roelver, B. Berghoff, M. Foerst, and B. Spangenberg, *Physica E* **38**, 152 (2007).
- ³⁴³Z. H. Lu, D. J. Lockwood, and J. M. Baribeau, *Solid State Electron.* **40**, 197 (1996).
- ³⁴⁴L. Tsybeskov and D. J. Lockwood, *Self-Organised Growth of Silicon Nanocrystals in Nanocrystalline Si/SiO₂ Superlattices*, edited by K. Sato, Y. Furukawa, and K. Nakajima (Elsevier, Amsterdam, 2001).
- ³⁴⁵D. J. Lockwood, G. F. Grom, P. M. Fauchet, and L. Tsybeskov, *J. Crystal Growth* **237**, 1898 (2002).
- ³⁴⁶J. M. Wagner, K. Seino, F. Bechstedt, A. Dymati, J. Mayer, R. Röller, M. Först, B. Berghoff, B. Spangenberg, and H. Kurz, *J. Vac. Sci. Technol., A* **25**, 1500 (2007).
- ³⁴⁷R. Röller, M. Först, O. Winkler, B. Spangenberg, and H. Kurz, *J. Vac. Sci. Technol., A* **24**, 141 (2006).
- ³⁴⁸E. F. Steigmeier, R. Morf, D. Grützmacher, H. Auderset, B. Delley, and R. Wessicken, *Appl. Phys. Lett.* **69**, 4165 (1996).
- ³⁴⁹V. Vinciguerra, G. Franzò, F. Priolo, F. Iacona, and C. Spinella, *J. Appl. Phys.* **87**, 8165 (2000).
- ³⁵⁰R. Röller, B. Berghoff, D. L. Bätzner, B. Spangenberg, and H. Kurz, *Appl. Phys. Lett.* **92**, 212108 (2008).
- ³⁵¹Z. H. Lu, J. M. Baribeau, D. J. Lockwood, M. Buchanan, N. Tit, C. Dharma-Wardana, and G. C. Aers, *SPIE* **3491**, 457 (1998).
- ³⁵²D. J. Lockwood, Z. H. Lu, and J. M. Baribeau, *Phys. Rev. Lett.* **76**, 539 (1996).
- ³⁵³Z. H. Lu, D. J. Lockwood, and J. M. Baribeau, *Nature* **378**, 258 (1995).
- ³⁵⁴S. Okamoto and Y. Kanemitsu, *Solid State Commun.* **103**, 573 (1997).
- ³⁵⁵D. J. Lockwood, M. W. C. Dharma-wardana, Z. H. Lu, D. H. Grozea, P. Carrier, and L. J. Lewis, *Mater. Res. Soc. Symp. Proc.* **737**, F1.1.1 (2003).
- ³⁵⁶Z. H. Lu and D. Grozea, *Appl. Phys. Lett.* **80**, 255 (2002).
- ³⁵⁷Y. Kanemitsu, M. Iiboshi, and T. Kushida, *J. Lumin.* **87**, 463 (2000).
- ³⁵⁸Y. Kanemitsu, Y. Fukunishi, M. Iiboshi, S. Okamoto, and T. Kushida, *Physica E* **7**, 456 (2000).
- ³⁵⁹F. J. Himpsel, F. R. McFeely, A. Taleb-Ibrahimi, and J. A. Yarmoff, *Phys. Rev. B* **38**, 6084 (1988).
- ³⁶⁰S. Rashkeev, D. Fleetwood, R. Schrimpf, and S. Pantelides, *Phys. Rev. Lett.* **87**, 165506 (2001).
- ³⁶¹G. Hadjisavvas and P. C. Kelires, *Physica E* **38**, 99 (2007).
- ³⁶²B. Rößner, G. Isella, and H. von Känel, *Appl. Phys. Lett.* **82**, 754 (2003).
- ³⁶³K. Seino and F. Bechstedt, *Semicond. Sci. Technol.* **26**, 014024 (2011).
- ³⁶⁴C. Q. Sun, T. P. Chen, B. K. Tay, S. Li, H. Huang, Y. B. Zhang, L. K. Pan, S. P. Lau, and X. W. Sun, *J. Phys. D: Appl. Phys.* **34**, 3470 (2001).
- ³⁶⁵Y. Kanemitsu, Y. Fukunishi, and T. Kushida, *Appl. Phys. Lett.* **77**, 211 (2000).
- ³⁶⁶J. Singh, *J. Non-Cryst. Solids* **299**, 444 (2002).
- ³⁶⁷R. B. Wehrspohn, J. N. Chazalviel, F. Ozanam, and I. Solomon, *Eur. Phys. J. B* **8**, 179 (1999).
- ³⁶⁸M. Cardona and F. H. Pollak, *Phys. Rev.* **142**, 530 (1966).
- ³⁶⁹G. Bastard, *Wave Mechanics Applied to Semiconductor Heterostructures* (Les Éditions de Physique, Les Ulis Cedax, 1988).
- ³⁷⁰G. L. Bir and G. E. Pikus, *Symmetry and Strain-Induced Effects in Semiconductors* (Wiley, New York, 1976).
- ³⁷¹H. Haken, *Quantum field theory of solids* (North-Holland Pub. Co., Amsterdam, 1976).
- ³⁷²S. Tomic and N. Vukmirović, *J. Appl. Phys.* **110**, 053710 (2011).
- ³⁷³Y. M. Niquet, C. Delerue, G. Allan, and M. Lannoo, *Phys. Rev. B* **62**, 5109 (2000).
- ³⁷⁴K. Seino, F. Bechstedt, and P. Kroll, *Phys. Rev. B* **86**, 075312 (2012).
- ³⁷⁵M. G. Burt, *J. Phys.: Condens. Matter* **4**, 6651 (1992).
- ³⁷⁶K. Nehari, M. Lannoo, F. Michelini, N. Cavassilas, M. Bescond, and J. L. Autran, *Appl. Phys. Lett.* **93**, 092103 (2008).
- ³⁷⁷T. Takagahara, *Phys. Rev. B* **36**, 9293 (1987).
- ³⁷⁸S. Kivelson and C. D. Gelatt, *Phys. Rev. B* **19**, 5160 (1979).
- ³⁷⁹F. Alvarez and A. A. Valladares, *Rev. Mex. Fis.* **48**, 528 (2002). Available at <http://www.ejournal.unam.mx/rmf/no486/RMF48607.pdf>.
- ³⁸⁰R. A. Street, *Hydrogenated Amorphous Silicon* (Cambridge University Press, Cambridge, 1991).
- ³⁸¹J. Singh, T. Aoki, and K. Shimakawa, *Philos. Mag. B* **82**, 855 (2002).
- ³⁸²X. Y. Lang, W. T. Zheng, and Q. Jiang, *IEEE Trans. Nanotechnol.* **7**, 5 (2008).
- ³⁸³L. Pan, Z. Sun, and C. Sun, *Scr. Mater.* **60**, 1105 (2009).
- ³⁸⁴X. Zianni and A. G. Nassiopoulou, *J. Appl. Phys.* **100**, 074312 (2006).
- ³⁸⁵E. L. Ramos, H. C. Weissker, J. Furthmüller, and F. Bechstedt, *Phys. Status Solidi B* **242**, 3053 (2005).
- ³⁸⁶D. B. T. Thoai, Y. Z. Hu, and S. W. Koch, *Phys. Rev. B* **42**, 11261 (1990).
- ³⁸⁷L. C. L. Y. Voon and M. Willatzen, *The k-p Method: Electronic Properties of Semiconductors* (Springer, Berlin, 2009).
- ³⁸⁸G. Allan, C. Delerue, and Y. Niquet, *Phys. Rev. B* **63**, 205301 (2001).
- ³⁸⁹J. M. Luttinger and W. Kohn, *Phys. Rev.* **97**, 869 (1955).
- ³⁹⁰B. Lassen, R. V. N. Melnik, and M. Willatzen, *Commun. Comput. Phys.* **6**, 699 (2009).
- ³⁹¹L. Jacak and J. K. M. Korkusinski, *Phys. Rev. B* **57**, 9069 (1998).
- ³⁹²G. Bastard, *Phys. Rev. B* **24**, 5693 (1981).
- ³⁹³I. M. Kupchak, D. V. Korbutyak, Y. V. Kryuchenko, A. V. Sachenko, I. O. Sokolovskii, and O. M. Sreseli, *Semiconductor* **40**, 94 (2006).
- ³⁹⁴A. Moskalenko, J. Berakdar, A. Prokofiev, and I. Yassievich, *Phys. Rev. B* **76**, 085427 (2007).
- ³⁹⁵S. Öğüt, J. R. Chelikowsky, and S. G. Louie, *Phys. Rev. Lett.* **79**, 1770 (1997).
- ³⁹⁶J. S. de Sousa, H. Wang, G. A. Farias, V. N. Freire, and E. F. da Silva, Jr., *Appl. Surf. Sci.* **166**, 469 (2000).
- ³⁹⁷A. M. Lepadatu, I. Stavarache, M. L. Ciurea, and V. Iancu, *J. Appl. Phys.* **107**, 033721 (2010).
- ³⁹⁸S. Goedecker and M. Teter, *Phys. Rev. B* **51**, 9455 (1995).
- ³⁹⁹C. Delerue, G. Allan, and M. Lannoo, *Phys. Rev. B* **48**, 11024 (1993).
- ⁴⁰⁰N. C. Bacalis and A. D. Zdetsis, *J. Math. Chem.* **46**, 962–970 (2009).
- ⁴⁰¹Y. M. Niquet, G. Allan, C. Delerue, and M. Lannoo, *Appl. Phys. Lett.* **77**, 1182 (2000).
- ⁴⁰²M. Nishida, *Semicond. Sci. Technol.* **21**, 443 (2006).
- ⁴⁰³N. Tit, Z. H. Yamani, J. Graham, and A. Ayesh, *Mater. Chem. Phys.* **124**, 927 (2010).
- ⁴⁰⁴N. Tit and M. W. C. Dharma-Wardana, *J. Appl. Phys.* **86**, 387 (1999).
- ⁴⁰⁵K. Leung and K. B. Whaley, *Phys. Rev. B* **56**, 7455 (1997).
- ⁴⁰⁶F. Trani, G. Cantele, D. Ninno, and G. Iadonisi, *Phys. Status Solidi C* **2**, 3435 (2005).
- ⁴⁰⁷M. Nishida, *J. Appl. Phys.* **98**, 023705 (2005).
- ⁴⁰⁸M. Nishida, *Phys. Rev. B* **59**, 15789 (1999).
- ⁴⁰⁹A. A. Prokofiev, A. S. Moskalenko, I. N. Yassievich, W. D. A. M. de Boer, D. Timmerman, H. Zhang, W. J. Buma, and T. Gregorkiewicz, *JETP Lett.* **90**, 758 (2009).
- ⁴¹⁰Z. Pu-Qin, H. Dong-Sheng, and W. Xing-Long, *Chin. Phys. Lett.* **22**, 1492 (2005).
- ⁴¹¹W. Pickett, *Comput. Phys. Rep.* **9**, 115 (1989).
- ⁴¹²L. W. Wang and A. Zunger, *J. Phys. Chem.* **98**, 2158 (1994b).
- ⁴¹³A. Zunger, *Phys. Status Solidi B* **224**, 727 (2001).
- ⁴¹⁴C. Bulutay, *Phys. Rev. B* **76**, 205321 (2007).
- ⁴¹⁵G. Bester, *J. Phys.: Condens. Matter* **21**, 023202 (2009).
- ⁴¹⁶A. Zunger and L. W. Wang, *Appl. Surf. Sci.* **102**, 350 (1996).
- ⁴¹⁷A. J. Read, R. J. Needs, K. J. Nash, L. T. Canham, P. D. J. Calcott, and A. Qteish, *Phys. Rev. Lett.* **69**, 1232 (1992).
- ⁴¹⁸H. C. Weissker, J. Furthmüller, and F. Bechstedt, *Phys. Rev. B* **65**, 155328 (2002).
- ⁴¹⁹F. A. Reboredo, A. Franceschetti, and A. Zunger, *Appl. Phys. Lett.* **75**, 2972 (1999).
- ⁴²⁰A. Franceschetti, L. W. Wang, and A. Zunger, *Phys. Rev. Lett.* **83**, 1269 (1999).
- ⁴²¹A. Franceschetti and A. Zunger, *Phys. Rev. Lett.* **78**, 915 (1997).
- ⁴²²A. Franceschetti and A. Zunger, *Phys. Rev. B* **62**, 2614 (2000).
- ⁴²³A. V. Gert and I. N. Yassievich, *JETP Lett.* **97**, 87 (2013).
- ⁴²⁴V. Ranjan, M. Kapoor, and V. A. Singh, *J. Phys.: Condens. Matter* **14**, 6647 (2002).
- ⁴²⁵N. L. Rowell, D. J. Lockwood, A. Karmous, P. D. Szkutnik, I. Berbezier, and A. Ronda, *Superlattices Microstruct.* **44**, 305 (2008).